Electromechanical Properties of Lead Magnesium Niobate - Lead Titanate and Lead Zirconium Titanate Ceramic Actuators

by

Stephen Hutton Ferguson
B. Eng., University of Victoria, 2000
Department of Mechanical Engineering
Faculty of Engineering

A Dissertation Submitted in Partial Fulfillment of the
Requirements for the Degree of
DOCTOR OF PHILOSOPHY
in the Department of Mechanical Engineering

December 5, 2005

Supervisory Committee

Co-Supervisor: Dr. Hubert W. King (Department of Mechanical Engineering)
Co-Supervisor: Dr. Afzal Suleman (Department of Mechanical Engineering)
Departmental Member: Dr. James W. Provan (Department of Mechanical Engineering)
Outside Member: Dr. George Beer (Department of Physics and Astronomy)

Abstract

Piezoelectric and electrostrictive actuators composed of lead titanate zirconate (PZT) and lead magnesium niobate-lead titanate (PMN-PT) are important in a variety of engineering applications. A review of the literature indicated that published phase diagrams for the PMN-PT system are based primarily on temperatures of dielectric transitions, rather than direct measurements of structural changes. Structural transformations in the PMN-PT ceramic system have not been investigated at non-ambient temperatures for compositions with less than 0.29 PT. The review also revealed that crack growth in cyclic electric fields has been observed in only two compositions of PZT, while no crack initiation or growth is observed in a relaxor composition of PMN-PT.

The X-ray diffraction results showed that the PMN-PT samples undergo multiple structural transformations on cooling through the temperature regions of their dielectric transitions. In compositions containing 0.0, 0.08, 0.10 and 0.20, an upper transformation temperature T_{α}, derived from a sharp change in coefficient of thermal expansion, lies well above the temperature T_m, of the observed maximum in dielectric constant. Lower structural transformation temperatures observed in these compositions lie close to the freezing temperature T_f, below which ceramics exhibit remanent polarization. The

temperatures of an upper structural transformation in PMN-PT ceramics with the higher PT mole fractions 0.30 and 0.35, agree closely with the Curie Temperature T_C.

Cracks emanating from the corners of Vickers diamond indents in the soft piezoelectric ceramics BM532 PZT (Navy-Type VI) and PMN–0.30PT were increased in length when subjected to low frequency cyclic electric fields that were applied normal to the crack. Crack growth was observed in fields of 2-5 x E_C, but no new cracks were initiated when these higher fields were applied. Similar induced cracks in hard piezoelectric PZT ceramics, did not exhibit visible crack growth when subjected to low frequency fields with amplitudes up to ±3.15 MV/m (1.6 x E_C), which is considered to be a safe maximum to avoid dielectric breakdown in PZT ceramics. No cracks were observed to emanate from the corners of either Vickers, or Knoop, diamond indents in samples of PMN-0.08PT. The intergranular cracks which emanate from the sides of the indents did not grow, and no new cracks were initiated, when the specimens were subjected to similar electric fields.

Table of Contents

List of Figures

List of Tables

List of Symbols

A	Helmholtz free energy
C	Curie constant
C_0, C_1	Capacitance
d	Piezoelectric charge coefficient (d-constant), units are C/N, or m/V
d_e	Electrostrictive d-constant.
D	Displacement of charged particles
ε_0	Permittivity of free space (vacuum) = 8.854×10^{-12} F/m
ε_C	Dielectric constant (also see K) = $\varepsilon/\varepsilon_0$
E_{ac}	AC electric field
E_{dc}	DC electric field
F_a	Anti-resonant frequency (Hz)
F_r	Resonant frequency (Hz)
g	Piezoelectric voltage coefficient (g constant)
G	Gibb's free energy
J_0, J_1	Bessel functions
k	Electromechanical coupling coefficient
k_{eff}	Effective coupling factor
K	Dielectric constant (also see ε_C) = $\varepsilon/\varepsilon_0$
MPB	Morphotropic Phase Boundary
η_1	Root of a Bessel equation
P	Polarization

PZT	Lead Zirconate Titanate
PLZT	Lead Lanthanum Zirconate Titanate
PMN	Lead Magnesium Niobate
PT	Lead Titanate
PMN-PT	Lead Magnesium Niobate-Lead Titanate
Q_M or Q	Quality factor (Mechanical Q)
s_{11}^D	Elastic compliance coefficient (superscript D indicates an open circuit)
s_{33}^E	Elastic compliance coefficient (superscript E indicates an closed circuit)
S	Entropy
SEM	Scanning electron microscope
θ	Curie-Weiss constant
T_0	Curie-Weiss temperature
T_α	Temperature at which the coefficient of thermal expansion changes (to be described in later in text)
Tan δ	Dielectric loss coefficient (dissipation factor) = 1/Q
T_d	Temperature at which polarization is detectable (on cooling)
T_D	Burns temperature
TEM	Transmission electron microscope
T_f	Temperature below which remanent polarization begins
T_m	Temperature of the maximum dielectric constant
U	Internal energy
Y	Young's modulus

Acknowledgements

I thank Drs. Hubert Wylam King and Afzal Suleman for their supervision and support throughout this research project.

I also acknowledge the advice and support of Drs. S. Eswar Prasad and David F. Waechter and Mr. Richard G. Blacow of Sensor Technology Ltd. (BM Hi-Tech Division). As well, I would like to thank Dr. Prasad for the many trips I made to Collingwood, Ontario where I was permitted to use his laboratories and precision measuring equipment to perform my research. I also extend a special thankyou to all the employees at Sensor Technology for their friendship, patience and assistance during my research at Collingwood.

I also express my gratitude to Dr. E. Andrew Payzant of Oakridge National Laboratory-Materials and Ceramics Division, for his advice and support.

My doctoral studies at the University of Victoria were made possible from an NSERC strategic grant, which covered my stipend and the many costs of materials, services and travel.

1.0 Introduction

Ferroelectric ceramics have been used as capacitors in electronic devices since 1945, because their dielectric properties are an order of magnitude greater than those of competitive materials. The application of these ceramics has been progressively extended to sensors and actuators over the past twenty years, because of their exceptional piezoelectric and electrostrictive properties. At the macroscopic level, these applications include sonar systems, piezoelectric transducers, ultra-precision actuators, accelerometers, hydrophones, surface acoustic wave filters and delay lines, ink jet print heads, touch controls, ultrasonic motors for cameras, ultrasonic cleaners and buzzers [1]. At the microscopic level, these ceramics are used for the operation of nano-scale pumps and motors [1, 2].

The exceptional properties that enable ferroelectric ceramics to be used for such a wide range of applications have their common origin in a set of crystal structures, each of which contains a set of unique polar directions along which ions are displaced, to develop a permanent net polarization [3]. The orientation of this polarization vector can be rotated, and fully reversed, by the application of an electric field, with varying degrees of hysteresis [3, 4]. The magnitude and orientation of this polarization vector, along with the hysteresis loop created by varying the electric field [5], determine the magnitude and nature of the piezoelectric and electrostrictive properties of the ferroelectric ceramics [4]. Since the present research is directed at improving the electromechanical properties of ferroelectric ceramics, the investigation of the composition and temperature dependence

of the structural transformations that generate the required polar directions is as an essential prerequisite to an understanding of the observed physical properties.

In the engineering applications of actuators, applied electric fields subject the component piezoelectrics and electrostrictors to static and/or cyclic stresses that are presumed to be well below the known mechanical fracture stresses [6]. However, if the ceramics contain isolated flaws, such as pores, agglomerates or cracks, it is possible that the consequent stress concentrations can raise the local stress above the fracture stress. In a cyclic field application, an existing crack can be thus be propagated during successive positive components of the stress cycles, so that the material is subjected to electric field induced mechanical fatigue, which can severely shorten the life of the component [7].
The investigation of crack propagation by cyclic electric fields has thus be made an essential component of the present study directed at improved piezoelectric and electrostrictive ceramics.

2.0 Literature review

2.1. Electromechanical properties

This review of the literature relevant to the research project is introduced by defining the unique physical properties that enable ceramics to be used as sensors and actuators [3–6].

2.1.1. Dielectric properties

2.1.1.1. Electric Polarization in Solids

Insulators resist the penetration of an applied field (E) by the displacement (D) of charged particles which oppose the field, i.e.:

$$D = \varepsilon E \qquad \text{Equation 2-1}$$

where D has units of Coulombs per m^2, E has units of volts per m and ε is the permittivity of the solid, in units of Coulombs/Vm (or Farads/m). The maximum electric field that a ceramic can withstand before electric breakdown is the dielectric strength, which is expressed in units of volts per unit thickness (i.e. typically kV/mm).

The polarization (P) is a measure of the increased dielectric displacement in a solid that is subjected to an incident electric field, compared to the electric displacement from the same field in a vacuum, and is given by the relationships:

$$D = \varepsilon_o E + P \qquad \text{Equation 2-2}$$

$$P = (D - \varepsilon_o E) = (\varepsilon E - \varepsilon_o E) \qquad \text{Equation 2-3}$$

where ε_o is the permittivity of free space, in units of F /m, and P has units of coulombs per unit area, i.e. C/m^2.

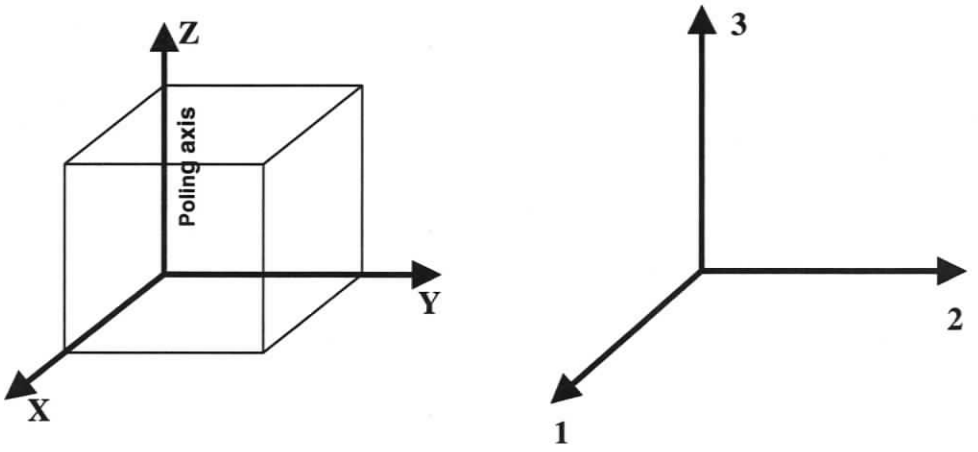

Figure 2-1 Axis designations [6]

In most insulators, the charged particles are electrons, but the displacement of charged atoms in certain crystal structures can also contribute to polarization in ionic ceramics. In this context, the direction of polarization is generally designated as the z axis of an orthogonal crystallographic system and the axes x, y and z are designated 1, 2 and 3, shown in Figure 2-1.

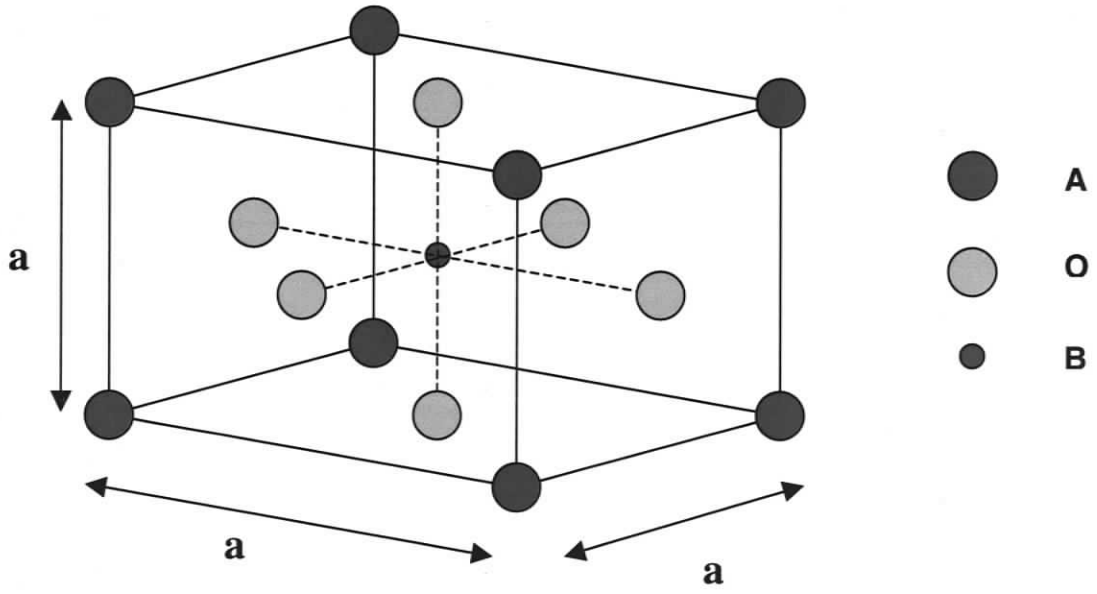

Figure 2-2 Cubic perovskite-type structure ABO_3 [8]

Many mixed oxide ionic ceramics with the composition ABO_3 crystallize in the perovskite structure, which is illustrated in Figure 2-2. The larger A cations (Ba, Pb) are located at the corners of the cubic unit cell, while the smaller B cations (Ti, Mg, Nb) occupy the body centred position. The oxygen ions are at the centres of the cell faces, so that the B cations are enclosed within octahedra of oxygen ions, which are the nearest neighbours. In ceramics, such as $BaTiO_3$, the small Ti cations are a loose fit within the oxygen octahedra and thus have large amplitudes of vibration, which are randomly distributed along the three <001> directions. On cooling below a critical temperature T_C, the vibrations cease and the Ti cation remains permanently displaced along one of the <001> directions, while the neighbouring oxygen atoms are displaced in the opposite

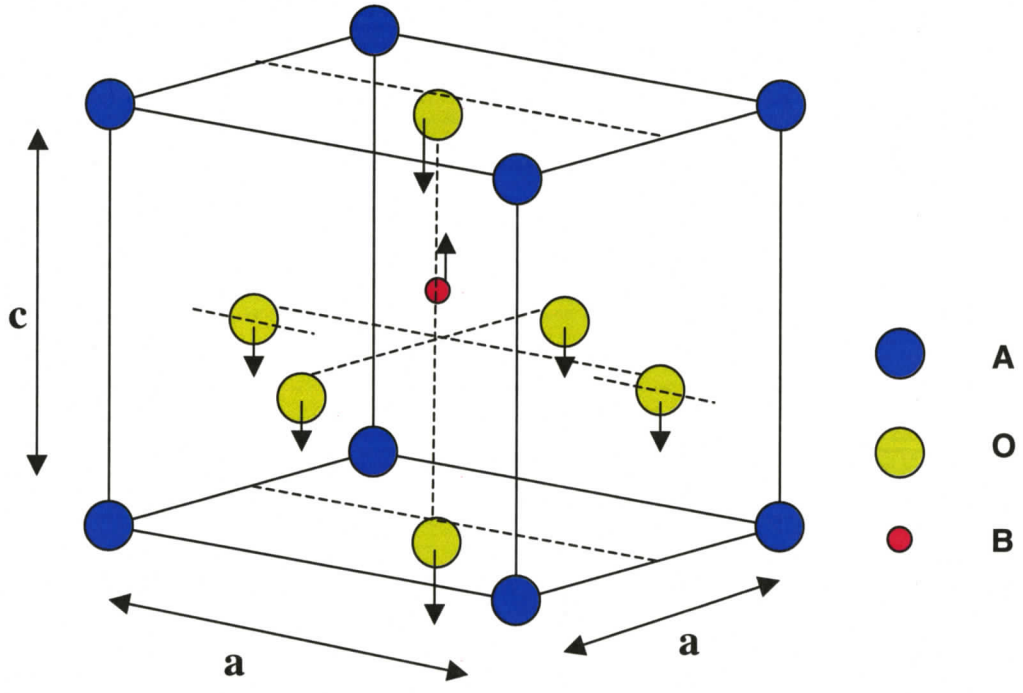

Figure 2-3 B-site cation is displaced upon polarization (based on [9])

direction, as shown in Figure 2-3, so that the crystal structure becomes tetragonal [3, 8, 10, 11].

The displacement of the titanium and oxygen ions $BaTiO_3$, creates in a permanent electric dipole and the cooperative alignment of dipoles in adjacent unit cells results in a spontaneous polarization (i.e. in the absence of an applied field) that extends over many unit cells, within a region referred to as a domain. On subsequent cooling below T_C, BaTiO3 passes through further critical temperatures, at which the direction of the Ti ion

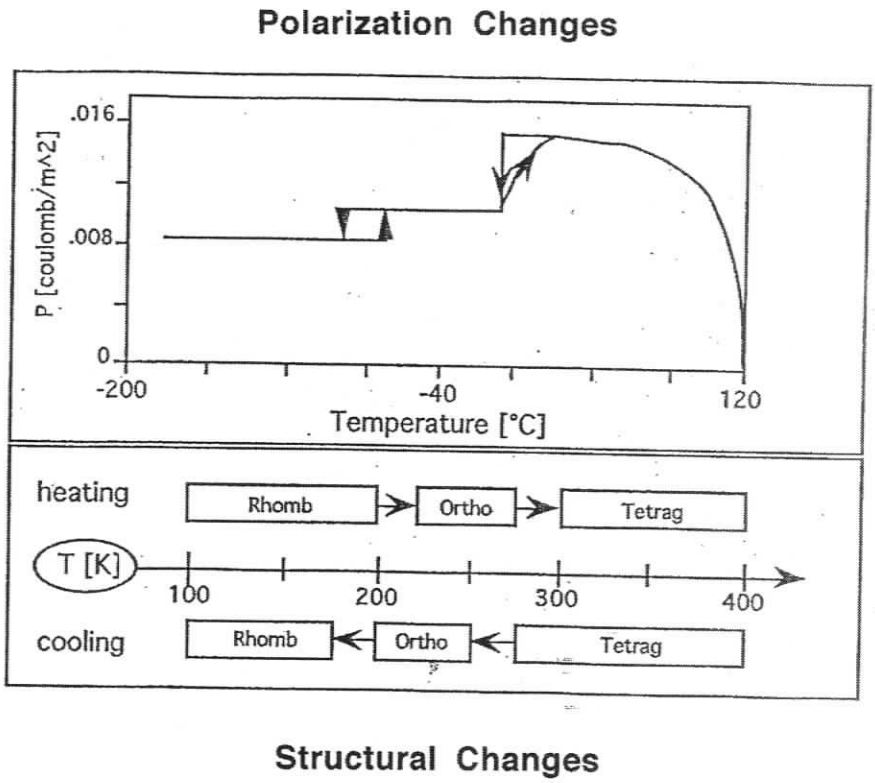

Figure 2-4 Polarization and Structural Changes for $BaTiO_3$ [8, 12, 13]

displacement changes progressively from [001] to [011] to [111], with consequent changes in structure from tetragonal to orthorhombic to rhombohedral. Polarization changes that accompany these crystal structural changes are illustrated in Figure 2-4.

2.1.1.2. Capacitance

Dielectric properties allow an insulator to act as a capacitor. The capacitance (C) is a measure of the charge (Q) stored between parallel plates for a given applied voltage (V):

$$C = Q/V \qquad \text{Equation 2-4}$$

and has units of coulombs per volt, or Farads (F).

In practice, the so-called static capacitance of a dielectric material is measured directly by a capacitance meter, which provides a standard voltage at a frequency of 1 kHz, which a well below the mechanical resonance of the specimen.

As illustrated schematically in Figure 2-5, the capacitance is increased (as shown by the squares) by the inclusion of the dielectric material between the capacitor plates. The measured capacitance thus depends on the permittivity (ε) of the dielectric material between the conducting plates, and on the area of the plates (A) and the distance (t) that separates them. Hence:

$$C = \varepsilon A/t \qquad \text{Equation 2-5}$$

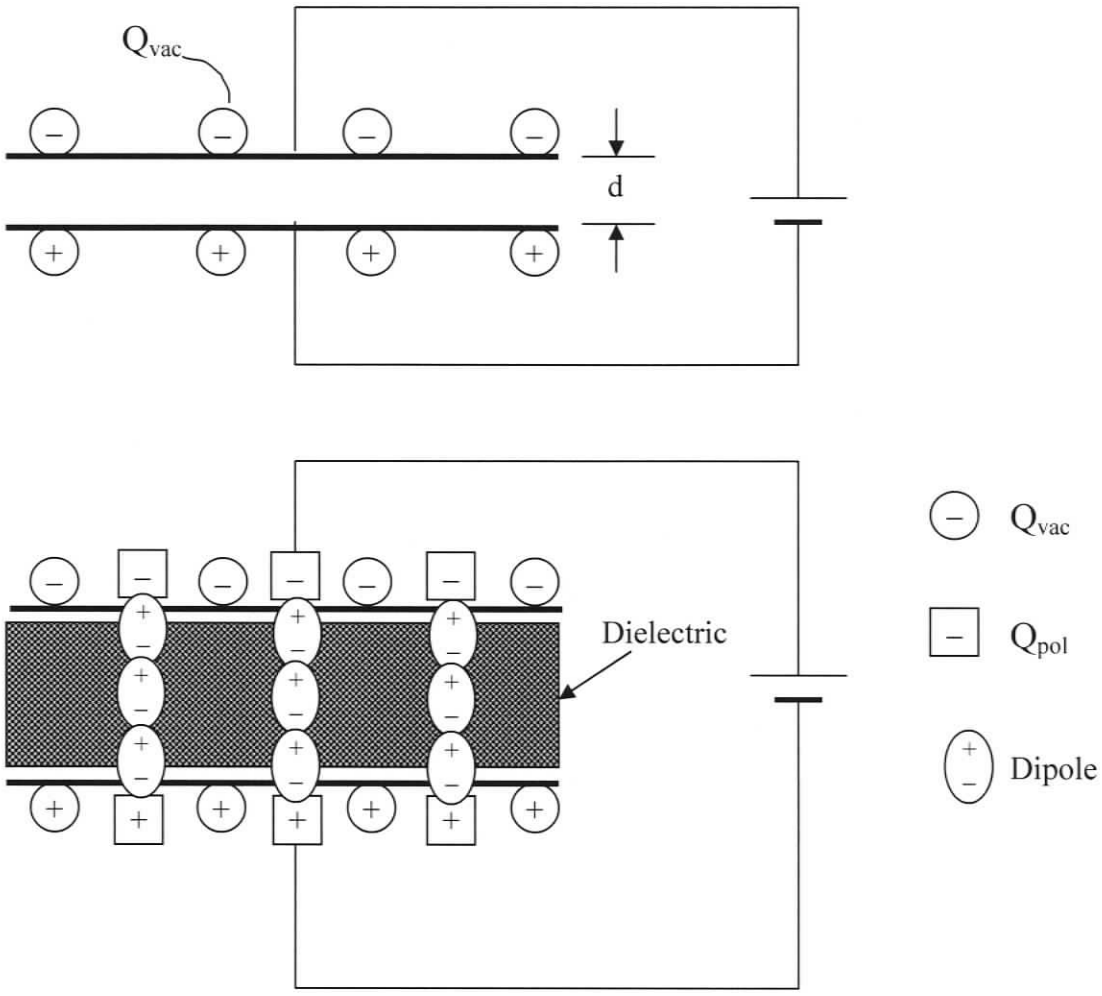

Figure 2-5 Diagram showing increased capacitance of dielectric (based on [11, 13])

The relative permittivity, or dielectric constant, referred to as K (or sometimes as ε_c) is the ratio between the permittivity of the material (ε) to the permittivity of free space (ε_o = 8.854 x 10^{-12} F/m [14]), i.e.

$$K = \varepsilon_C = \varepsilon/\varepsilon_O = C\,t\,/\,\varepsilon_O A \qquad \text{Equation 2-6}$$

The polarization (P) developed in the dielectric by an applied voltage (V) is related to K by the relationship:

$$P = (\varepsilon E - \varepsilon_o E) = (K - 1)\,\varepsilon_o E = (K - 1)\,\varepsilon_o V / t \qquad \text{Equation 2-7}$$

where, as before, E = the applied electric field.

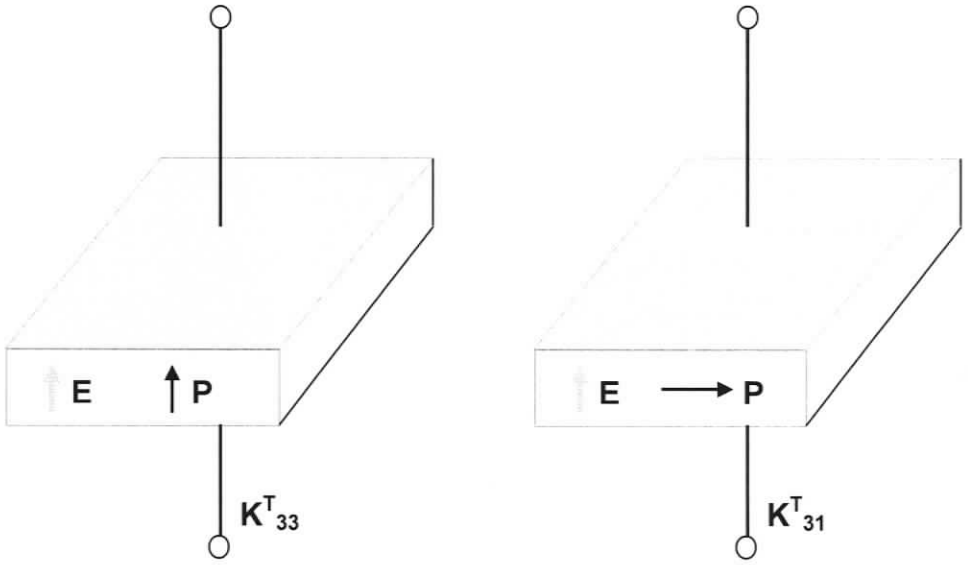

Figure 2-6 Notation for relative permittivity [15, 16]

Since polarization can also be induced in directions other than the direction of an applied field, the parameter K is assigned subscripts (related to the orthogonal axes defined previously in Figure 2-1), as illustrated in Figure 2-6. The first subscript gives the direction of the field associated with the applied electric field, while the second subscript gives the direction of the vector of the induced polarization. This nomenclature also

contains superscripts indicating the boundary conditions, where T, E, D and S indicate constant stress, field, displacement and strain, respectively.

2.1.1.3. Dielectric loss in AC fields

Dielectric losses occur in capacitors in AC fields due to the inertia of the charged species and the movement of charged species in doped ceramics. As indicated in Figure 2-7 the direct current I_{chg} that charges up a capacitor is 90° out of phase with the applied voltage, while the AC loss current I_{loss} is parallel to the applied voltage, so that the total current

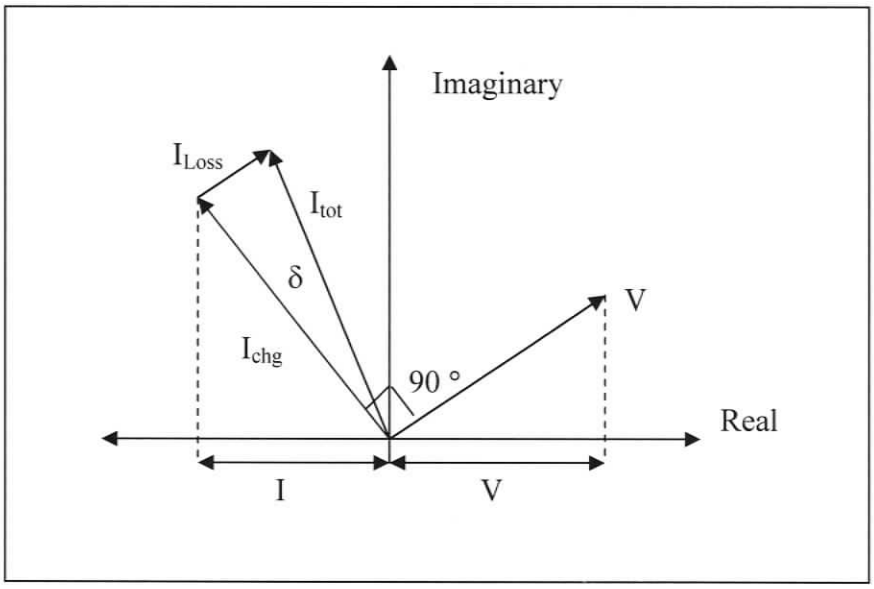

Figure 2-7 Diagram of dielectric losses in AC fields (based on [17, 18])

from both effects leads the charge current by an angle of $(90 - \phi) = \delta$. The dielectric loss factor is represented by the tangent of the loss angle ($\tan \delta$) and is thus often referred as the loss tangent. For practical applications, the loss factor should be as small as possible. Referring to the parallel equivalent circuit for a dielectric ceramic in Figure 2-8, the loss factor can be represented by the ratio of the resistance (that governs I_{chg}) to the reactance

(that governs I_{loss}). This ratio can be measured directly by an impedance bridge, which is typically built into capacitance meters.

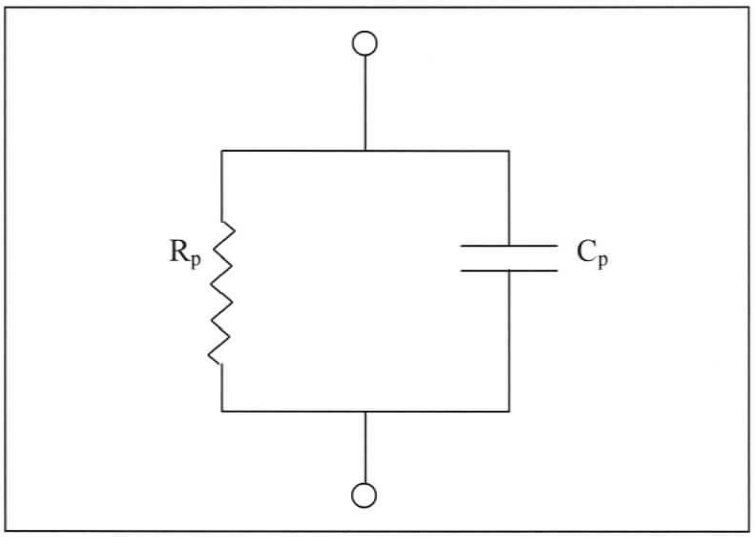

Figure 2-8 Parallel equivalent circuit for a ceramic element [6]

The displacement current density (J) for a parallel plate capacitor, due to sinusoidal-time-varying field (E_t), is provided from the following equations [19]:

$$E_t = E_1 \exp(i\omega t) \qquad \text{Equation 2-8}$$

$$J = \frac{\partial D}{\partial t} = (\omega\varepsilon' + i\omega\varepsilon'')E_1 \exp(i\omega t) \qquad \text{Equation 2-9}$$

where:

D is the electric displacement, E_1 is the field along direction 1 and ε' and ε'' are the real and imaginary parts of the permittivity (ε). That is:

$$\varepsilon = \varepsilon' + i\varepsilon'' \qquad \text{Equation 2-10}$$

From Equation 2-9, the average power loss per unit volume of the capacitor is $\frac{\omega\varepsilon''E_1^{\,2}}{2}$ and the maximum stored-energy density is $\frac{\varepsilon'E_1^{\,2}}{2}$. Therefore, the inverse of the dielectric loss (tan δ), which is used to define the dielectric quality factor ($Q_{dielectric}$) for the dielectric material, is given by following equation [19]:

$$Q_{dielectric} = \frac{\max imum\ stored\ energy}{average\ power\ loss} x\omega = \frac{\varepsilon'}{\varepsilon''} = \frac{1}{\tan\delta} \qquad \text{Equation 2-11}$$

2.1.2. Ferroelectric properties

The dielectric properties of industrial insulators are listed in Table 2-1. The exceptionally high dielectric constants of $BaTiO_3$ and the other mixed oxides BZT, PZT and PMN stem from the degree of permanent polarization that is present in these perovskite ceramics,

Table 2-1 Dielectric constants at 25 °C

Material	Abbrev.	Dielectric constant (K) [20]	Tan δ
Teflon		2.1	< 0.0005 [21]
Silica glass (fused quartz)		3.8	0.0009 [21]
Polyvinylidene fluoride		8.4	
Alumina		10	< 0.00033 [21]
Magnesium oxide		20	
Barium tetratitanate		40	
Titanium oxide		100	
Calcium oxide		160	
Strontium titanate	ST	320	0.00005 [22]
Lead zirconate titanate	PZT	1000-3250 [6]	< 0.02 [6]
Barium titanate	BT	1000-5000	0.056 [21]
Barium zirconate titanate	BZT	20,000	
Lead magnesium niobate	PMN	20,000 -30,000 [6]	0.08 [6]

which gives them an enhanced response to an applied electric field. The relatively high tan δ dissipation of these ceramics is related to leakage currents associated with space charges that develop due to doping with solutes of different valence. For the reasons described below, these ceramics are referred to as ferroelectrics.

2.1.2.1. Temperature Dependence of Dielectric Constants

The temperature dependence of the dielectric constant (ε_C or K) of $BaTiO_3$ is shown in Figure 2-9. On cooling, K passes through a sharp peak that accurately locates the critical temperature T_C. At temperatures above T_C the plot follows the Curie-Weiss law:

$$\varepsilon = \varepsilon_o + C / (T - T_0) \qquad \text{Equation 2-12}$$

Where C is the Curie constant and T_0 is the temperature at which the plot of the inverse of the dielectric constant vs. temperature extrapolates to zero. As shown in Figure 2-9, T_0 lies a few degrees below T_C and would only become equal to T_C if the dielectric constant really went to infinity. Above its T_C temperature, $BaTiO_3$ is paraelectric with the centrosymmetric cubic perovskite structure [12] shown previously in Figure 2-2. In order for spontaneous electrical dipoles to develop, and be retained, on cooling through T_C, this cubic structure becomes distorted into a non-centrosymmetrical tetragonal, rhombohedral or orthorhombic crystal structure [23]. In compounds such as $BaTiO_3$, the peak in the temperature dependence of dielectric constant is so sharp that the temperature of the transition to the polarized state is not distinguishable from the temperature of the associated structural transformation to the low temperature non-centrosymmetrical phase,

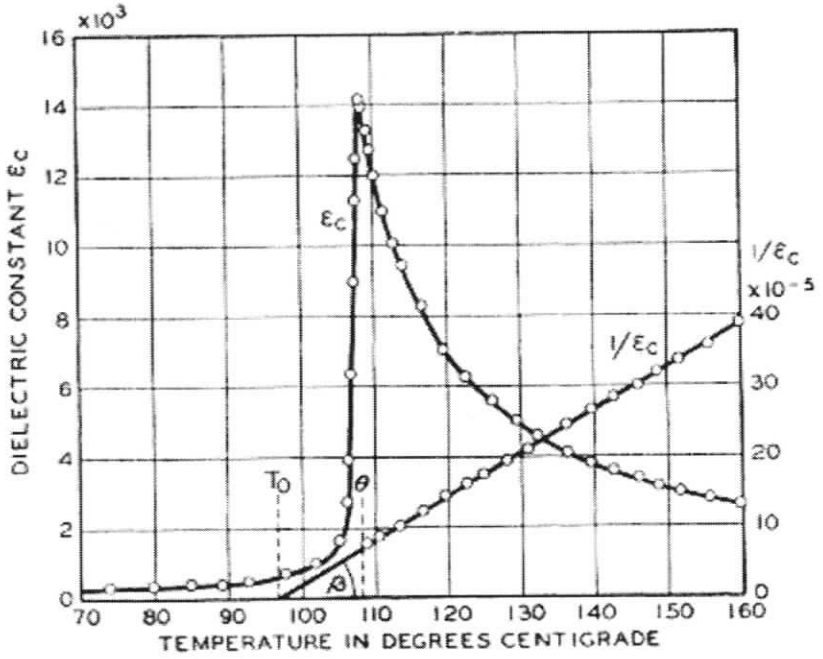

Figure 2-9 Sharp peak in the temperature dependence of dielectric constant in $BaTiO_3$ [24]

so both temperatures are used interchangeably. However, as will be shown later, many industrial solid solution ceramics exhibit a relatively broad peak in dielectric constant, so that the temperatures of the structural changes cannot be precisely equated to the temperature T_m of the maximum of the broad peak in dielectric constant.

2.1.2.2. Field Dependence of Polarization

The electric dipoles created by the spontaneous polarization that occurs on cooling a ferroelectric ceramic through T_C are aligned within small regions, referred to as domains, but as the domains themselves are randomly oriented, samples that are freshly cooled through T_C do not display a measurable polarization at the sample surface. When an

electric field is applied, however, domains aligned parallel to the field grow at the expense of domains with other orientations and a measurable net polarization is observed. As shown in Figure 2-10, when the field is increased to a sufficiently high value, all of the domains become aligned parallel to the field and the polarization attains a saturation value (P_S). On removing the field, most of the domains remain aligned along the direction of the field, causing the sample to have a remanent polarization (P_R), and the specimen is then said to be "poled". Ferroelectrics are generally used in the poled condition, as this state is associated with a high degree of polarization, which enhances the dielectric and related properties. Also, in this condition, small changes in applied field result in approximately linear changes in polarization and the direction of these changes is reversed when the sign of the field is reversed.

On reversing the direction of the applied field, the domains become randomly oriented at a coercive field $-E_C$ and with increasing negative fields the domains become re-aligned with the reversed field to display a negative saturation polarization ($-P_S$). The ability to reverse the polarity by reversing the sign of the electric field is the basic criterion for defining a ferroelectric ceramic. Re-applying a positive field, generates a hysteresis loop, as the polarization passes through zero and then increases to P_S. The degree of hysteresis is governed by the ability of a domain wall to move, to enable the growth of domains aligned to an applied field. Domains can be anchored by the addition of trivalent or divalent dopants that can dissolve in the perovskite structure, in place of the tetravalent Ti ions, and then migrate to create space charges that restrict the movement of the domain walls [25]. These dopants generate square hysteresis loops, with relatively large coercive

fields, which give sharp the switching that is required for memories. Multivalent dopants that create vacancies at the large A ion sites of the perovskite structure increase the

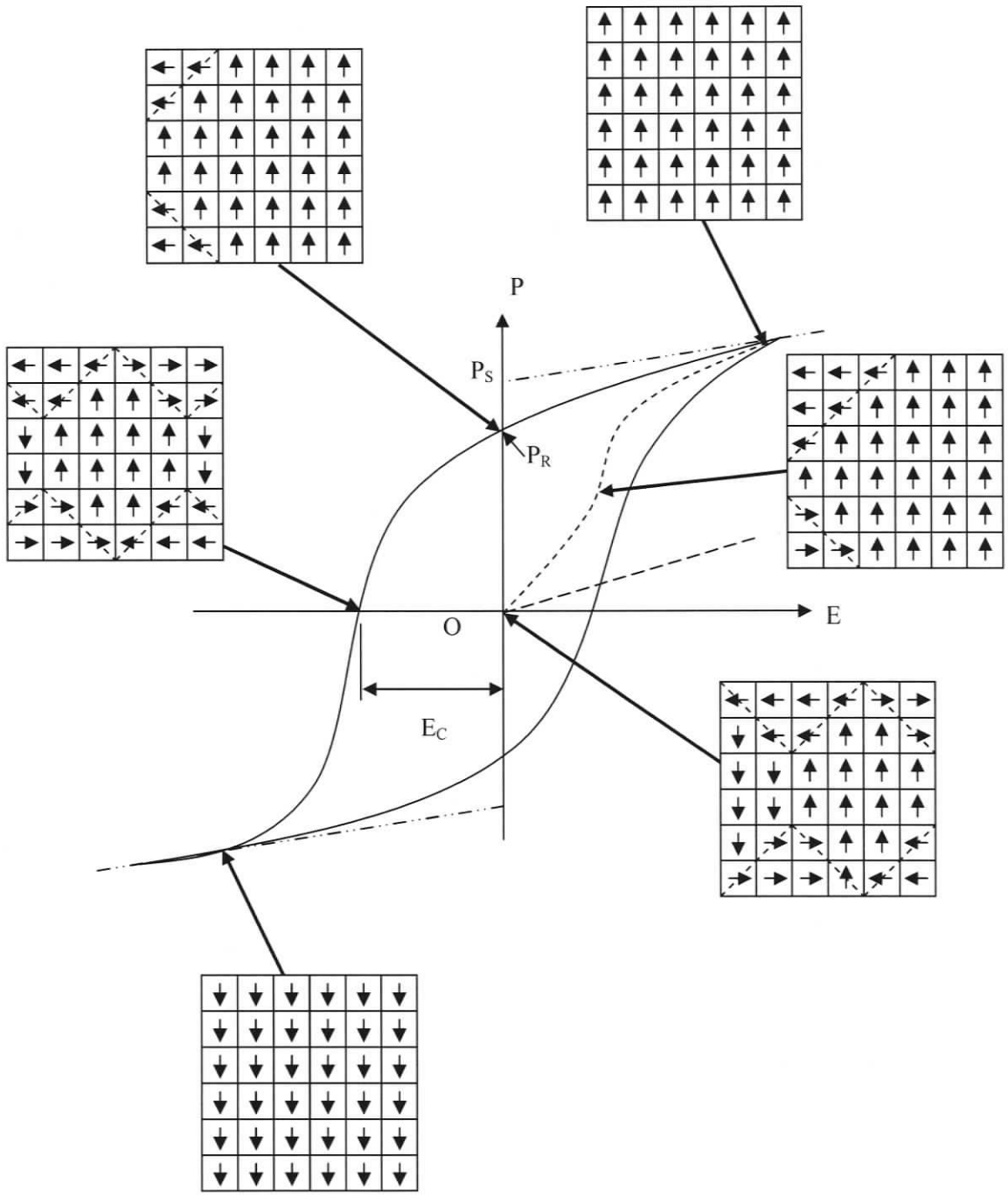

Figure 2-10 Polarization vectors vs. applied electric field [1, 7, 8, 26]

mobility of the domains walls. These dopants reduce the degree of hysteresis and the coercive fields, to cause a consequent reduction in the dissipation losses (tan δ) that occur in AC fields [25].

2.1.3. Piezoelectric properties

2.1.3.1. Definitions of piezoelectricity

Dielectric materials that produce an electric field (E) when subjected to an applied stress (σ) are referred to as piezoelectric [11], where the prefix "piezo" comes from the Greek word for pressure. This effect, which is used in sensors and transducers, is expressed in terms of the piezoelectric voltage coefficient, or g-constant, defined as:

$$E = g\sigma \qquad \text{Equation 2-13}$$

where g has units of Vm/N

Conversely, when an electric field (E) is imposed on a piezoelectric material a strain (e) is developed. This opposite effect, which is used in actuators, is expressed in terms of the piezoelectric charge coefficient, or d-constant, defined as:

$$e = dE \qquad \text{Equation 2-14}$$

where d has units of C/N, or m/V

The two piezoelectric constants are related through the Young's modulus (Y): i.e.:

$$Y = 1/gd \qquad \text{Equation 2-15}$$

As the electric field is a vector, and stresses and strains are 2nd order tensors, the piezoelectric coefficients in different directions in a crystal are related to orthogonal axes

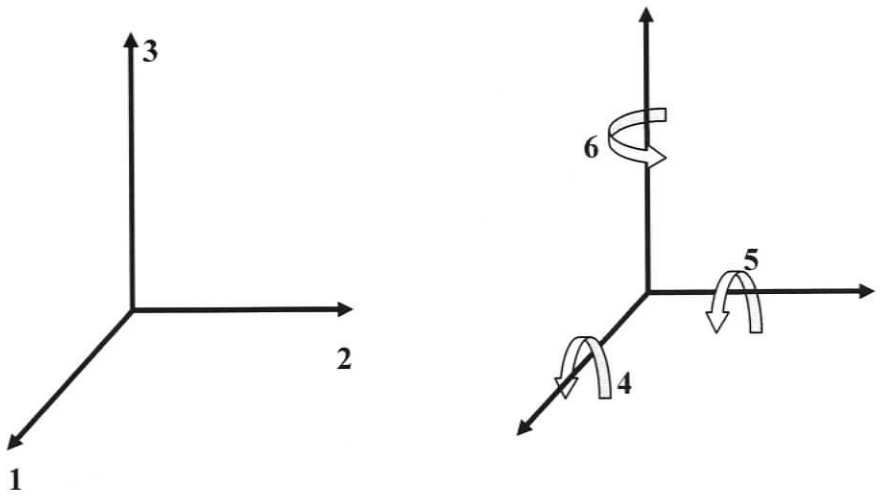

Figure 2-11 Axis designations for subscripts [15, 16]

as shown in Figure 2-11. The piezoelectric coefficients are thus expressed with subscripts where 1, 2, and 3 refer to the directions parallel to the axes x, y and z, while the shear stresses and strains about these axes are referred to as 4, 5 and 6. The first subscript refers to the direction of the applied field, or the charge produced, while the second subscript gives the direction of the mechanical stress, or strain, using the reduced tensor notation [4]. For many applications, the piezoelectric elements are in the form of discs that are silvered on the flat faces, as illustrated in Figure 2-12. For a field applied normal to these faces, i.e. along direction 3, the induced strain parallel to the direction of the applied field (which will result in a change in thickness t), is given by the charge coefficient d_{33}. For the same field, an induced strain normal to the applied field (which will result in a change in the diameter D) is given by the charge coefficient d_{31}.

For the silvered discs in Figure 2-12, the applied field $E_3 = V_3/t$ and the parallel strain $\varepsilon_3 = \Delta t/t$, so the equation for the d-constant can be written in term of the extension Δt and the applied voltage V_3, i.e.

$$\Delta t = d_{33} V_3 \qquad \text{Equation 2-16}$$

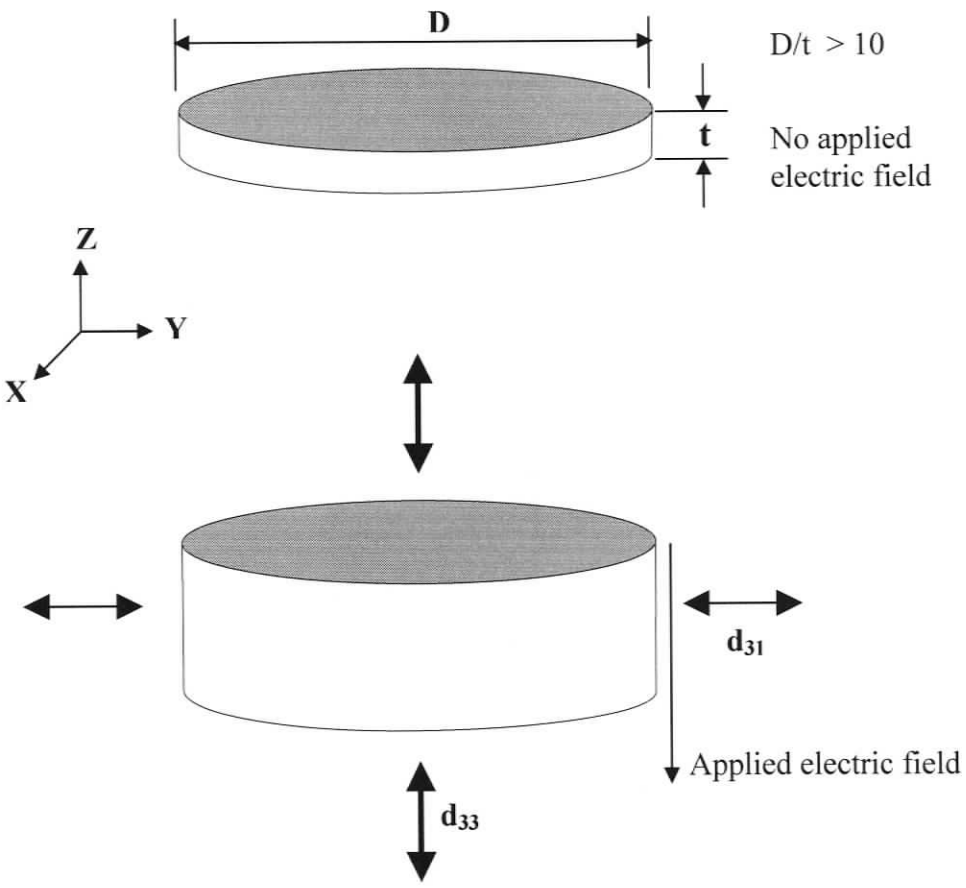

Figure 2-12 Piezoelectric disc showing the d_{33} and d_{31} directions (based on [27])

2.1.3.2. Piezoelectric Modes of Vibration

Modes of vibration for piezoelectric discs, rods, plates and tubes, etc., are illustrated in Figure 2-13. The most common shape is the disc shown previously in Figure 2-12, but

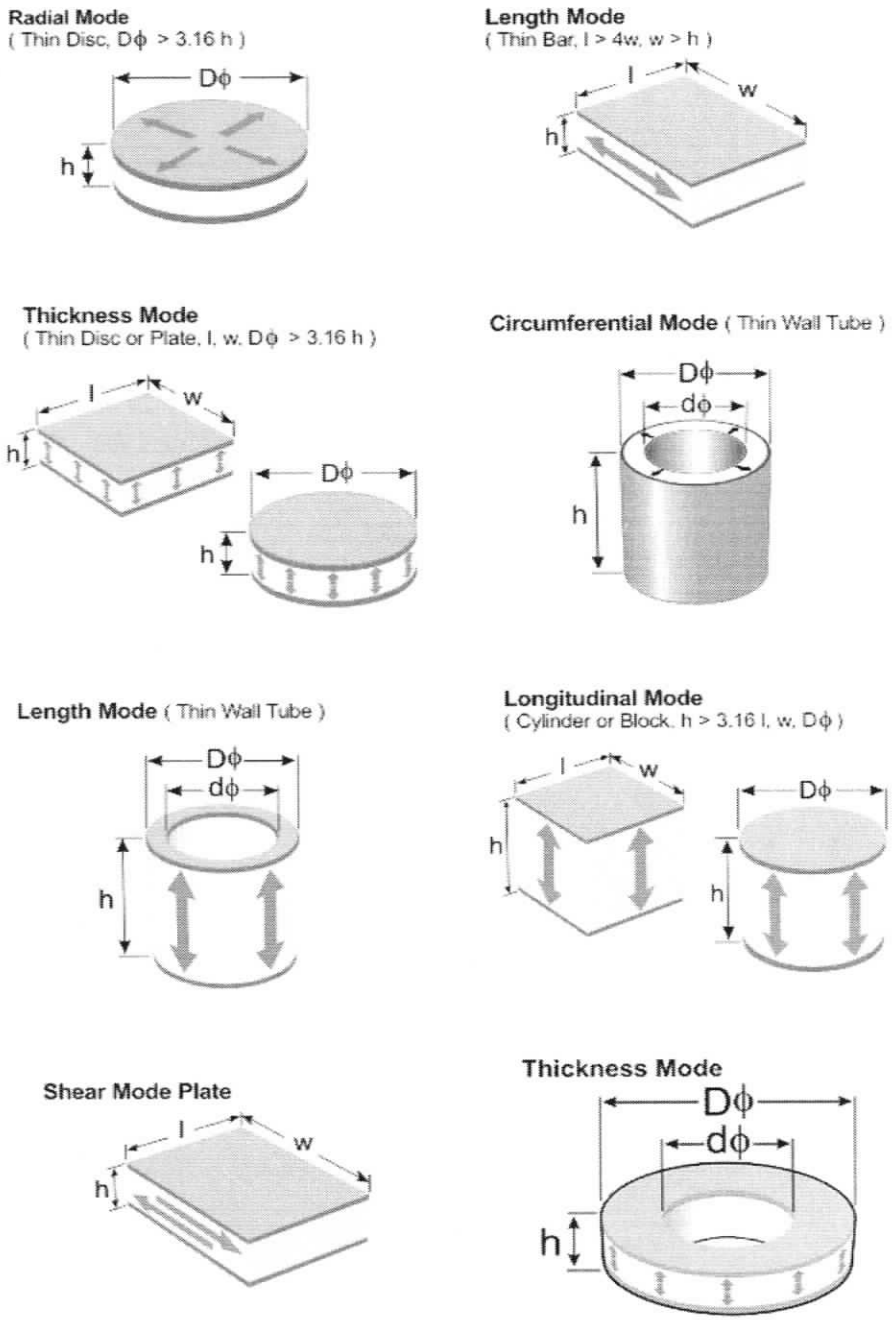

Figure 2-13 Piezoelectric modes of vibration [15, 16]

the length extension mode for thin plates was also used for the present experiments. A relative measure of the resonant frequency of a particular shaped specimen is given by the frequency constant N, which is the product of the resonance frequency and the linear dimension governing the resonance. Equations to derive N for different modes of vibration are given by [15, 16]:

$N_1 = F_r D$ (Hz.m) Radial Mode Disc

$N_2 = F_r l$ (Hz.m) Length Mode Disc

$N_3 = F_r l$ (Hz.m) Length Mode Cylinder

$N_4 = F_r h$ (Hz.m) Thickness Mode Disc, Plate

$N_5 = F_r h$ (Hz.m) Shear Mode Plate

2.1.3.3. Electrical Impedance and Resonance

Electrical impedance is defined as the voltage drop across an element divided by the

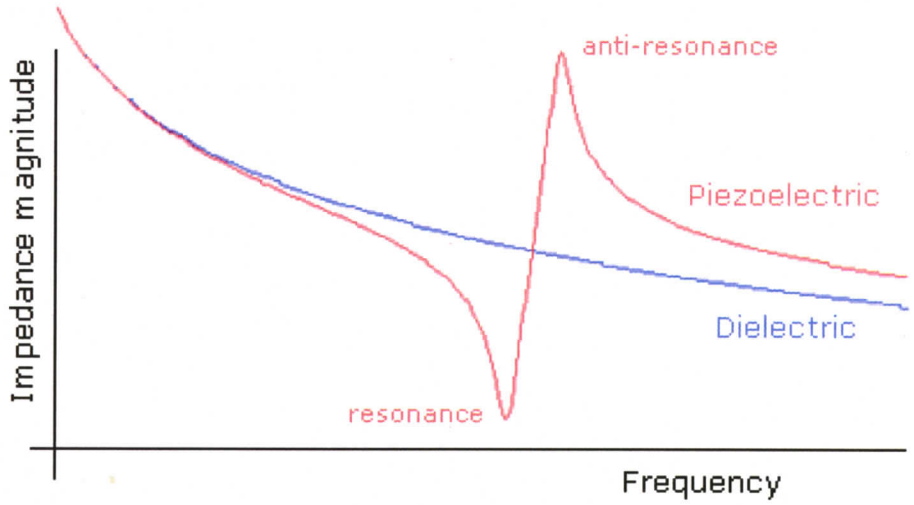

Figure 2-14 Impedance for piezoelectric and non-piezoelectric element [28]

current through the element. The impedance of a non-piezoelectric dielectric decreases exponentially with increasing frequency, as shown in Figure 2-14. Impedance measurements can also be used to determine the resonance of the operational vibrational modes of a piezoelectric element in accordance with the series equivalent circuit shown in Figure 2-15. As illustrated in Figure 2-14, if the input frequency is high enough, a piezoelectric element will display an electrical resonance (F_r) and anti-resonance (F_a) at well-defined frequencies, due to the electrical input signal exiting a mechanical resonance.

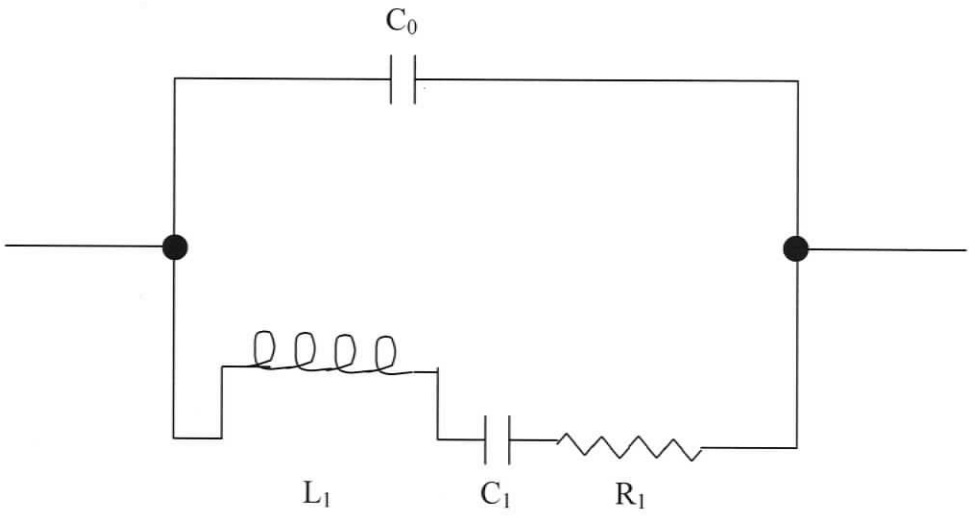

Figure 2-15 Equivalent circuit for a transducer element [2, 15, 16, 29]

The frequency dependence of impedance for a commercial piezoelectric element is shown in Figure 2-16. With increasing frequency, the impedance reduces to a low point at F_r, and then suddenly rises to a higher sharp apex at F_a, after which it gradually reduces.

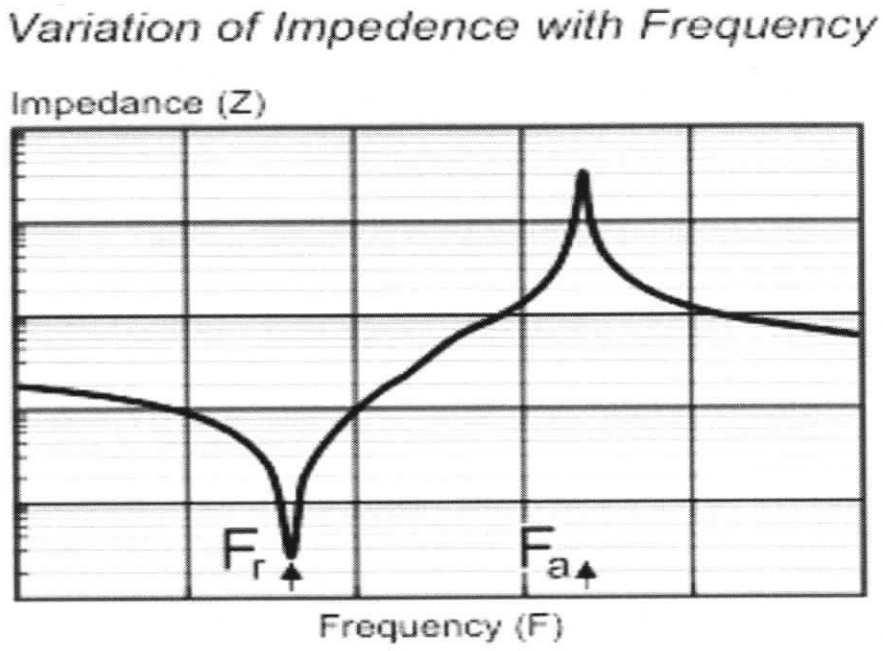

Figure 2-16 Variation of Impedance with Frequency [15, 16]

The resonant and anti-resonant frequencies are defined in the following equations [30]:

$$F_r = \frac{1}{2\pi}\sqrt{\frac{1}{L_1 C_1}} \qquad \text{Equation 2-17}$$

$$F_a = \frac{1}{2\pi}\sqrt{\frac{C_0 + C_1}{L_1 C_0 C_1}} \qquad \text{Equation 2-18}$$

Impedance measurements for piezoelectric elements behave in a capacitive manner below the resonant frequency (F_r) and above the anti-resonant frequency (F_a), but between these frequencies, the impedance behaves inductively. This behaviour is illustrated by the variation of phase angle with frequency, as shown in Figure 2-17.

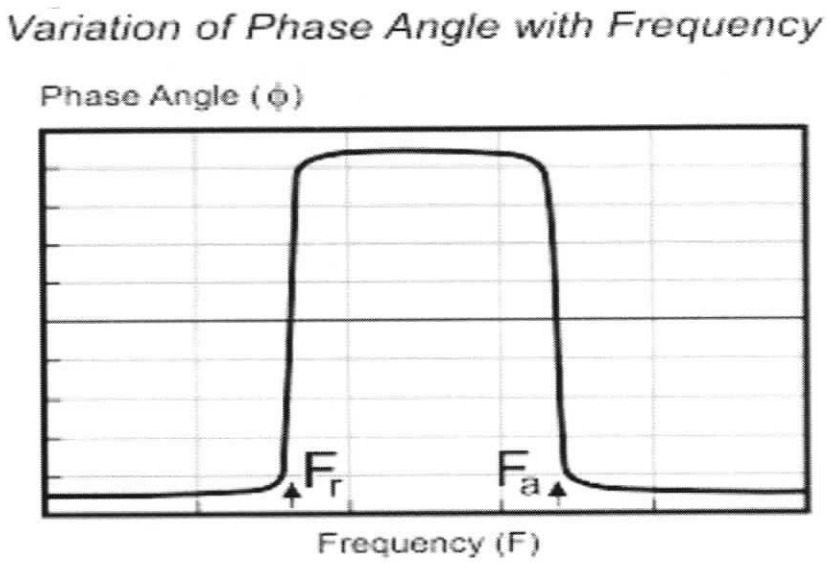

Figure 2-17 Variation of Phase Angle with Frequency [15, 16]

2.1.3.4. Piezoelectric Coupling Coefficient

The coupling of the electrical energy input to the mechanical energy output of a piezoelectric, that stimulates the resonances referred to above, is governed by the piezoelectric coupling coefficient k, which is sometimes referred to as the electromechanical coupling coefficient. This coefficient is defined as the ratio of the mechanical energy accumulated to the electric energy applied to the ceramic or vice versa, i.e.:

$$k = \sqrt{\frac{Mechanical\ Energy\ Stored}{Electrical\ Energy\ Applied}} \quad \text{(Actuators)}$$

$$= \sqrt{\frac{\textit{Electrical Energy Stored}}{\textit{Mechanical Energy Applied}}} \quad \text{(Transducers)} \qquad \text{Equation 2-19}$$

Equations for calculating the piezoelectric coupling factor (which is also a 2nd order tensor) for various modes of vibration are given below [15, 16]:

$$\frac{k_p^2}{1-k_p^2} = \frac{(1-\sigma^E)J_1\left[\eta_1\left(1+\frac{\Delta F}{F_r}\right)\right]-\eta_1\left(1+\frac{\Delta F}{F_r}\right)J_0\left[\eta_1\left(1+\frac{\Delta F}{F_r}\right)\right]}{(1+\sigma^E)J_1\left[\eta_1\left(1+\frac{\Delta F}{F_r}\right)\right]} \qquad \text{Equation 2-20}$$

where:

J_0: Bessel function of the first kind and zero order
J_1: Bessel function of the first kind and first order
σ^E: Poisson's Ratio
η_1: Lowest positive root of:

$$(1+\sigma^E)J_1(\eta) = \eta J_0(\eta)$$

$$k_{33}^2 = \frac{\frac{\pi}{2}}{1+\frac{\Delta F}{F_r}} \tan\frac{\frac{\pi}{2}\frac{\Delta F}{F_r}}{1+\frac{\Delta F}{F_r}} \qquad \text{Equation 2-21}$$

$$\frac{k_{31}^2}{1-k_{31}^2} = \frac{\pi}{2}\left(1+\frac{\Delta F}{F_r}\right)\tan\left(\frac{\pi}{2}\frac{\Delta F}{F_r}\right)$$

where:

$$\Delta F = F_a - F_r \text{ (Hz)}$$

In addition, the parameter, k_{eff}, is often used to describe the effective coupling factor of an arbitrary resonator, at its fundamental resonance, or at any overtone, using the relationship [15, 16]:

$$\frac{k_{eff}^2}{1-k_{eff}^2} = \frac{F_a^2 - F_r^2}{F_r^2} \qquad \text{Equation 2-22}$$

2.1.3.5. Mechanical Quality Factor

The mechanical quality factor (Q or Q_M) is a measure of the quality of the frequency produced by the piezoelectric resonator in terms of the sharpness of the resonance

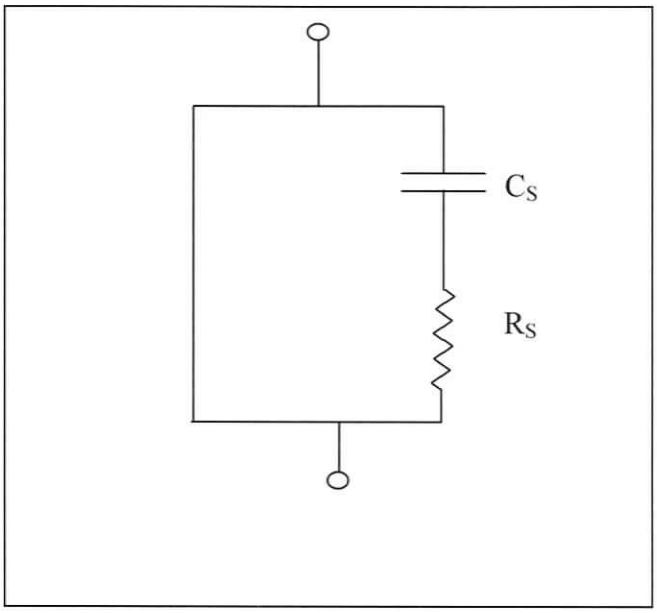

Figure 2-18 Series equivalent circuit for a piezoelectric ceramic element [15, 16]

frequency. The mechanical Q is defined as the ratio of the reactance to the resistance in a series equivalent circuit representing the piezoelectric circuit (refer to Figure 2-18). The equations for Q derived with this circuit are given below [6]:

$$Q_M = \frac{1}{2\pi F_r Z_m C_0}\left(\frac{F_a^2}{F_a^2 - F_r^2}\right) \qquad \text{Equation 2-23}$$

where:

F_r: Resonant frequency (Hz)

F_a: Anti-resonant frequency (Hz)
Z_m: Resistance at F_r (ohms)
C_0: Static Capacitance (Farads)

The mechanical Q can also be determined using [6]:

$$Q_M = \frac{F_r}{F_1 - F_2} \qquad \text{Equation 2-24}$$

where F_1, F_2 are the -3 dB points on the frequency/impedance curve from the resonance frequency F_r.

2.1.3.6. The Compliance of Piezoelectrics

The elastic compliance (s) is the inverse of the Young's modulus, which describes the mechanical stiffness of a material. In piezoelectric materials the Young's modulus is dependent on the stress, strain and electrical conditions. The value of Y, or s, can thus be derived the vibrational frequencies of a piezoelectric specimen of known dimensions, using the following equations.

$s = 1/Y = \text{strain} / \text{stress}$ Equation 2-25

$= 1/\rho v^2 \qquad (m^2/N)$ Equation 2-26

$=1/ (\rho (2\pi Fl)^2) \qquad (m/sec)$ Equation 2-27

where

ρ: density
v: sonic velocity
l: length of the element (m)

The various elastic coefficients for different loading conditions are given by [15, 16]:

$s_{33}^D = 1/\rho v_1^2 \quad (v_1 = 2\pi F_a l)$ Equation 2-28

$$s_{33}^{E} = s_{33}^{D}/ (1-k_{33}^{2}) \qquad \text{Equation 2-29}$$

$$s_{11}^{E} = 1/\rho v_2^{2} \quad (v_2 = 2\pi F_r l) \qquad \text{Equation 2-30}$$

$$s_{33}^{D} = (1-k_{31}^{2})\, s_{11}^{E} \qquad \text{Equation 2-31}$$

where k is the relevant piezoelectric coupling coefficient.

The piezoelectric coupling and the elastic coefficients are directly related to the d-constants of piezoelectrics according to the relationship:

$$d_{3x} = k_{3x} \sqrt{(K_3^{T} s_{xx})} \qquad \text{Equation 2-32}$$

where K_3 is the relative dielectric constant of the material and x = 1, 2 or 3.
Hence, piezoelectrics intended for use as actuators should have relatively high values of the coefficients k, K and s.

2.1.3.7. Strain vs. Field Plots for Piezoelectrics

Various forms of strain vs. applied field for piezoelectrics are illustrated in Figure 2-19. For a given field, non-ferroelectric piezoelectric materials, such as quartz, show very low magnitudes of strain and the strain vs. field plots are strictly linear, with no hysteresis in reversed fields. The hard PZT in the figure shows a lower strain for a given voltage and a minimal hysteresis loop in a reversed field. The soft PZT displays an even greater strain for a given voltage, but also displays considerable hysteresis in a reversed field.

It is significant to note that the hysteresis effects of field induced polarization and strain are opposite. The hard piezoelectrics that show very little piezoelectric hysteresis exhibit

considerable polarization hysteresis. Both of these effects have the same root, i.e. the locking of domain walls, which resist change. In the hard piezoelectrics, the lack of domain wall movement restricts the amount of induced strain and also causes the high degree of remanent polarization and high coercive fields that contribute to polarization hysteresis.

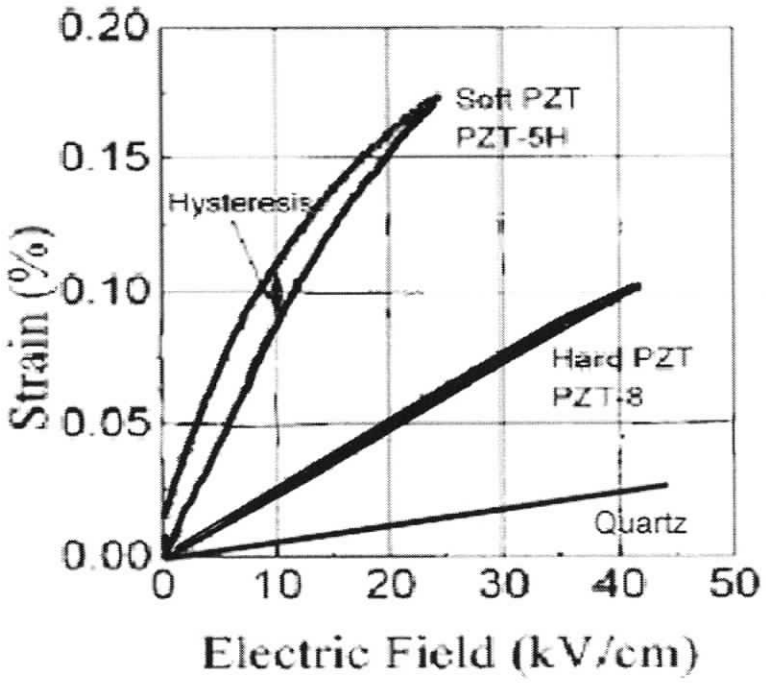

Figure 2-19 Strain vs. E-field behaviour for various electromechanical ceramics [31]

2.1.3.8. Piezoelectric Hysteresis and Linearity Parameters

As shown in Figure 2-19, the magnitude of the piezoelectric hysteresis in an extension vs. voltage (or strain vs. field) plot can be defined as the maximum difference in extension at a given voltage divided by the maximum measured extension. Soft piezoelectrics

typically exhibit 15% hysteresis, while the hysteresis in hard piezoelectric is typically below 2% [6].

Figure 2-19 also shows that the linearity of extension vs. voltage plots can be expressed quantitatively as the maximum percent deviation of a given point on the increasing voltage plot relative to the best straight line least squares fit. The linearity varies from 1-10 %, with the lower values occurring in the hard piezoelectrics [6].

2.1.3.9. Poling and Ageing

The ageing rate of piezoelectric ceramics is a linear logarithmic function with time [15, 16]:

$$Ageing\ Rate = \frac{1}{\log t_1 - \log t_2}\left(\frac{P_1 - P_2}{P_1}\right) \qquad \text{Equation 2-33}$$

where:

t_1, t_2: number of days after polarization

P_1, P_2: measured parameters (i.e. capacitance, resonant frequency, etc.)

Ageing rate: is per decade of time.

2.1.3.10. Effect of Crystal Symmetry on Piezoelectric Properties

Centrosymmetric crystal structures have a symmetry radiating from the centre of the crystal cell and thus cannot display polarization when subjected to an applied stress (Figure 2-20-A). However, nonsymmetrical crystal structures, such as that of quartz, can become polarized along a polar direction, when subjected to stress (Figure 2-20-B). When the stress is removed, the polarization induced in the quartz crystal will disappear,

because it lacks a permanent dipole, so the stress-induced polarization is completely reversible. The reverse effect happens when the quartz crystal is subjected to an electric field, where the crystal will return to its original dimensions upon removal of the electric field. The piezoelectric properties of quartz are thus strictly linear functions of stress, or applied field, because quartz is a piezoelectric, but not a ferroelectric material [4]. The ferroelectrics, such as barium-titanate and lead-zirconate-titanate ceramics, have polar symmetry combined with permanent molecular dipoles and thus display enhanced polarization when subjected to mechanical stress (Figure 2-20-C).

It is also evident from Figure 2-21 that the simple lack of a centre of symmetry is not a sufficient condition for supporting the piezoelectric effect. The non-centrosymmetric point group 432 can support polar directions, but the operation of the 3-fold and 4-fold rotational symmetry axes can reverse the symmetry along the orthogonal crystal axes, so that oppositely charged species cannot exist on opposite faces of these cubic crystals [4]. The remaining 20 non-centrosymmetric point groups exhibit the piezoelectric effect. Of these, 10 point groups are pyroelectric, i.e. they exhibit a temperature dependence of the magnitude of their spontaneous polarization. The other 10 piezoelectric point groups

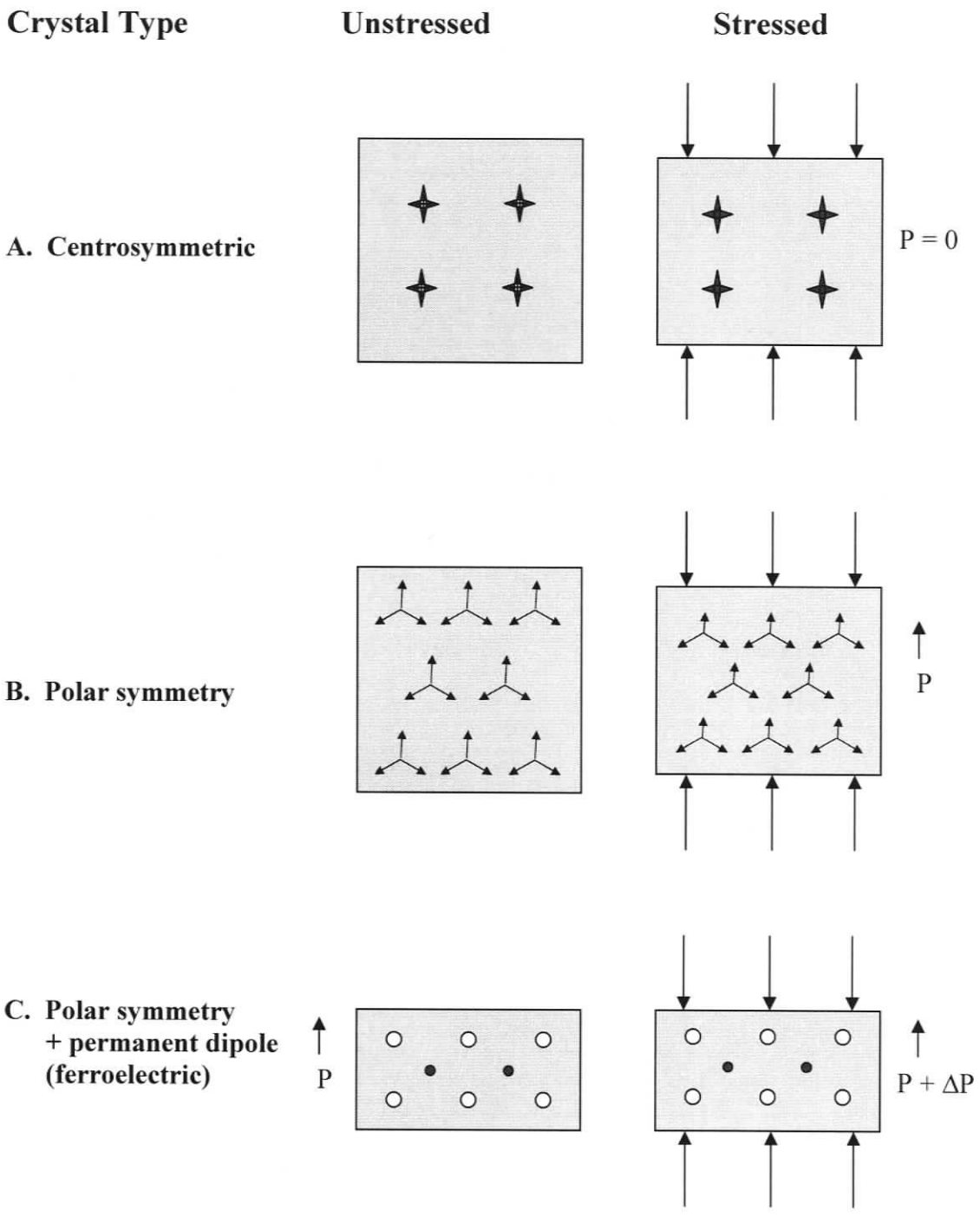

Figure 2-20 Effects of stress on various crystal types [8]

are non-pyroelectric and, like quartz, do not exhibit spontaneous polarization in the absence of an applied field. Further, not all of the pyroelectrics exhibit the ferroelectric behaviour associated with a field-induced change in the orientation of the dipoles within domains. Since ferroelectrics form the bulk of the ceramics used as sensors and actuators in industrial applications, because of their exceptional properties in the poled condition, they are often mistakenly regarded as the prototype of piezoelectrics, when they are in fact a sub-set of a sub-group of pyroelectric piezoelectrics!

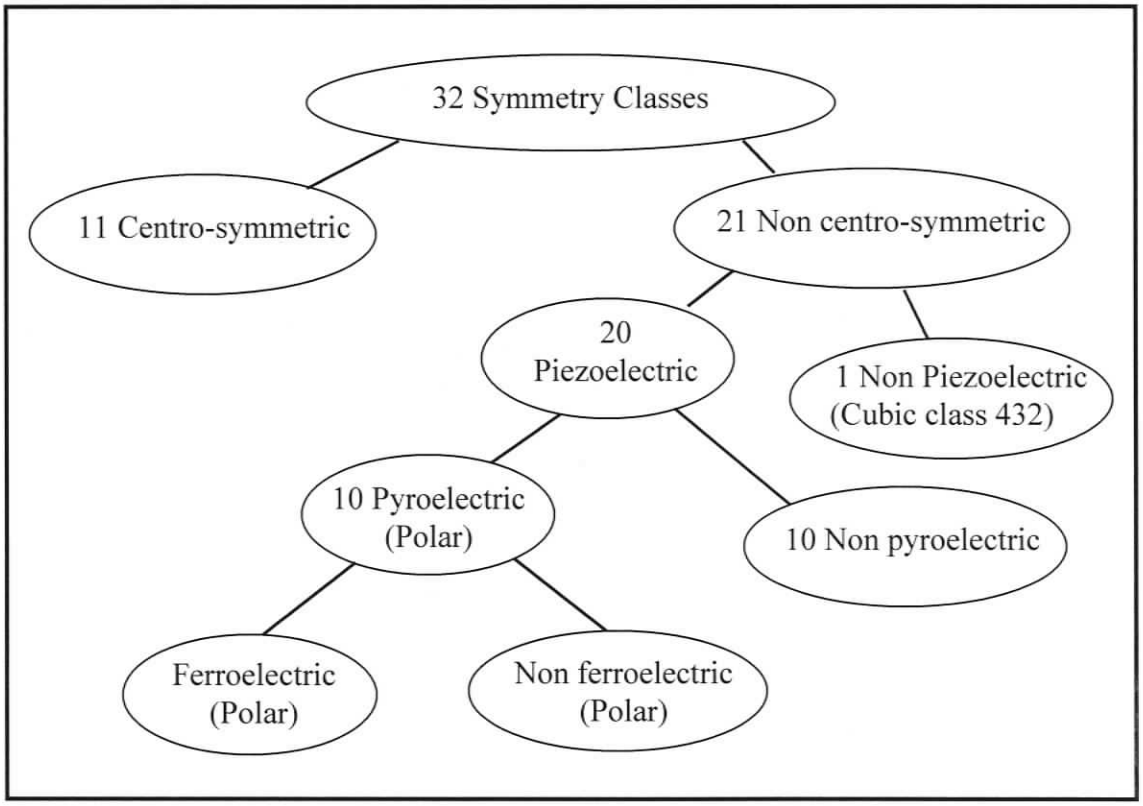

Figure 2-21 Crystal Symmetry Diagram [20, 32]

2.1.4. Electrostrictive Properties

2.1.4.1. Definition of Electrostriction

All materials, regardless of crystal symmetry, display the electrostrictive effect, in which a minute strain is generated by an applied electric field. In contrast to the piezoelectric effect, this strain is proportional to the square of the applied field, as indicated by [3]:

$$e_{3x} = d_e E_3^{\,2} \tag{2-34}$$

where d_e is the electrostrictive d_{3x}-constant.

A direct consequence of this relationship is that the reverse effect does not occur in electrostrictors, (i.e. an applied stress does not generate an electric charge, so that electrostrictors cannot be used as load sensors, or transducers. Further, since the direction of the strain is independent of the sign of the applied voltage, in contrast to the piezoelectrics, there is no requirement for the crystal structure of an electrostrictor to be non-centrosymmetric. In most cases the induced strains are negligibly small, but a notable exception occurs in relaxor ferroelectrics.

2.1.4.2. Relaxor Ferroelectrics

In contrast to the sharp transitions observed in piezoelectric ferroelectrics, the relaxors exhibit a diffuse dielectric transition from the paraelectric to the ferroelectric state. The temperature dependence of the dielectric constant in the region of this ferroelectric transition takes the form of a broad shallow peak and the decay in ferroelectric behaviour at temperatures above the diffuse maximum at T_m does not follow the Curie-Weiss Law [33], as shown in Figure 2-22. In addition, with increasing frequency of the applied

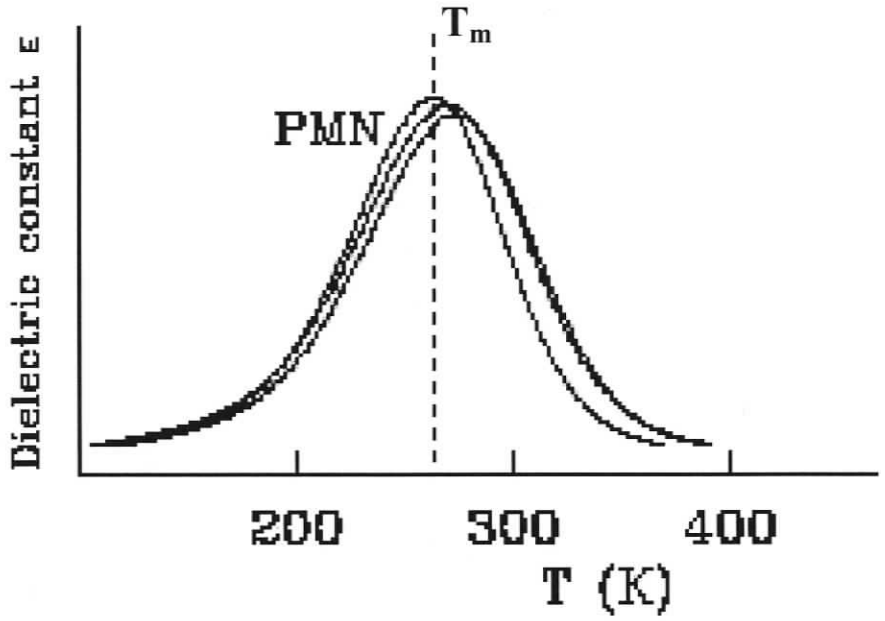

Figure 2-22 Graph of dielectric constant vs. temperature for PMN [34, 35]

electric field, the broad peak in dielectric constant is decreased in magnitude and the temperature (T_m) of the maximum is shifted to towards higher temperatures.

As mentioned in Section 2.1.4.1, relaxors exhibit electrostrictive properties as the induced strain is proportional to the square of the applied field. The magnitude of the strain for a given voltage is also relatively large, compared to normal piezoelectrics, and there is little or no hysteresis in reversed fields. Since the dielectric constant maintains a moderately high value over a relatively large temperature range, and the field induced strain is both large and reversible, these materials are strong candidates for capacitor and actuator applications where sensitivity to temperature, and/or strain hysteresis, is of prime concern.

The relaxor ferroelectric transition was first identified by Smolenskii and Agranovska [36] in lead magnesium niobate, $Pb(Mg_{1/3}Nb_{2/3})O_3$ (PMN) and lead nickel niobate $Pb(Ni_{1/3}Nb_{2/3})O_3$ (PNN). These authors noticed that the onset of the relaxor transition on cooling is accompanied by a distinct decrease in the coefficient of thermal expansion of the ceramic and used this property as a criterion to identify the relaxor transition in other systems [37–40]. Cross has also reported that the coefficient of thermal expansion of a sample of PMN containing 0.1 mole fraction of lead titanate (PMN-0.1PT) changes by an order of magnitude from 10^{-6} mm/mm per °C at room temperature to 10^{-5} mm/mm per °C at 400 °C [40]. On the basis of an observation that a gradual (but definitive) change occurs in the slope of strain vs. temperature measurements in PMN, Cross labeled the temperature at which the plot deviates from a linear trend T_0, as shown in Figure 2-23

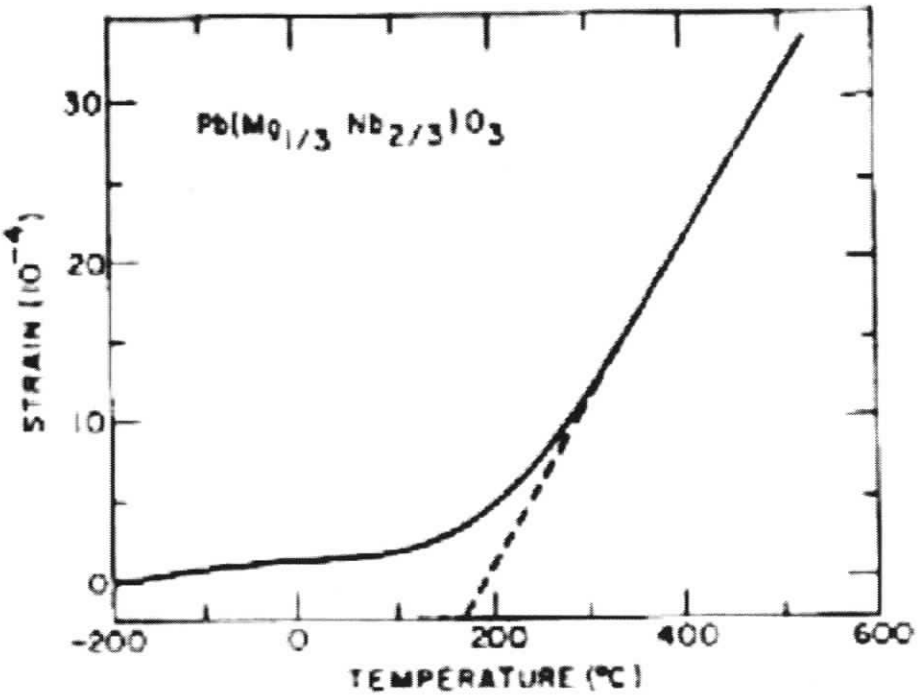

Figure 2-23 Thermal expansion S_{11} vs. Temperature for PMN [41]

[41]. On the basis of this observation, he suggested that the relaxor transition is a second order phase change, and used the value of T_0 = 350 °C to calculate the magnitude of the polarization fluctuations that were considered to be the basis of the relaxor transition in PMN. Burns and Dacol [42] defined an equivalent temperature, T_D, at which the thermal dependence of the optical refractive index is no longer linear on cooling, and reported values of T_D equal to 343 °C and 345 °C for the two laser light frequencies used to study PMN. While this result is close to the T_0 temperature of 350 °C obtained by Cross, both of these values are hundreds of degrees greater than the T_m temperature for PMN, which lies close to -18 °C [38].

Although Cross's suggestion of a second order phase change has been widely accepted, as discussed in Section 2.1.4.4 below, the observation upon which it was based has been

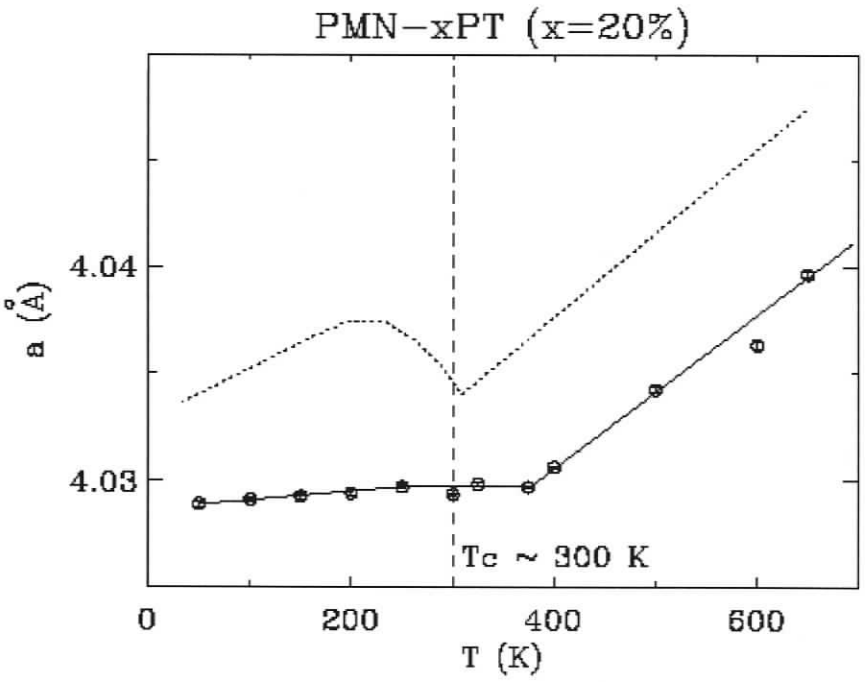

Figure 2-24 Lattice parameter (a) vs. Temperature [34]

largely disregarded in theoretical treatments of the relaxor transition, and is frequently ignored by experimentalists. For example, in a recent neutron diffraction study, Xu et al. [34], noted an abrupt change in the slope of the temperature dependence of the *a* lattice parameter of a single crystal of PMN-0.2PT, as shown in Figure 2-24. Apart from brief comments, that the abrupt change in slope has also been observed by others [44, 45] and that it is characteristic of compositions in the relaxor region, they pay no attention to the fact that it occurs at a temperature that it some 80 °C above the dielectric transition temperature T_C.

2.1.4.3. The crystal structure of PMN

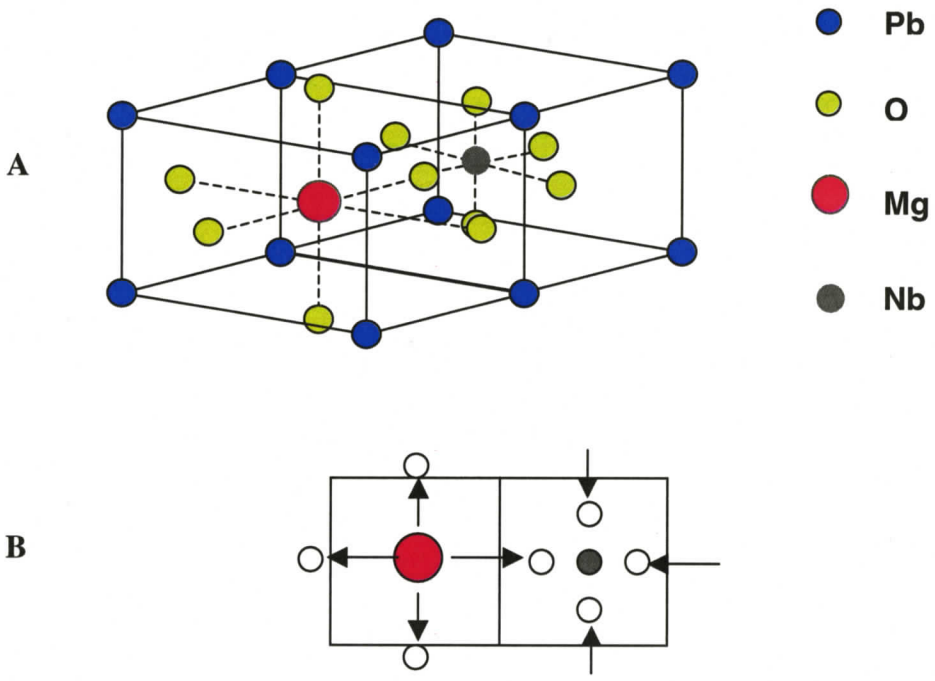

Figure 2-25 A. 3D diagram for Pb(•Mg,•Nb)O_3
B. Schematic for Pb(•Mg,•Nb)O_3 [46]

In the paraelectric state, the relaxor PMN has the cubic perovskite crystal structure shown in Figure 2-25. The small Nb^{5+} ions at the body centre positions are a loose fit within the surrounding oxygen ion octahedra (like the Ti^{4+} ions in the $BaTiO_3$ structure in Figure 2-1), and so cause no lattice strain. On the other hand, the large Mg^{2+} ions are too big to fit into the body centre sites, so displace the neighbouring oxygen ions along <100> directions. The oxygen octahedra in adjacent unit cells are thus pressed closer to the enclosed Nb^{5+} ions. If the Nb^{5+} and Mg^{2+} ions are randomly distributed among the body centre sites, the oxygen ion displacements will cause the *a* parameters of neighbouring unit cells to deform elastically by $\pm\Delta a$, but the randomness of the deformation directions will leave the unit cell with overall cubic symmetry [31]. Similar random rhombohedral deformations along the diagonal directions <111> would also leave the structure

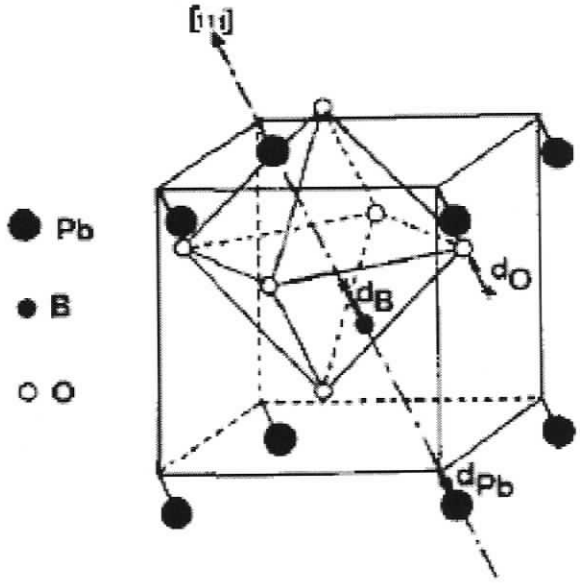

Figure 2-26 Rhombohedral structure of locally polar nanoregions at 5K [47]

macroscopically cubic [47], but the randomness of the ion displacement will cause the Bragg diffraction peaks to become broadened, so it is common practice to index the X-ray and neutron diffraction patterns of the relaxor phase as pseudocubic, [47, 48]. From neutron diffraction studies of PMN, de Mathan et al. [47] have shown that the pseudocubic structure persists at temperatures down to 5 K, and should be considered as a two phase structure composed of a non-polar cubic matrix within which about 20% of the volume is composed of polar regions with local rhombohedral symmetry generated by atomic shifts along <111> directions, as shown in Figure 2-26.

It is evident from Figure 2-25, that the elastic strain in the pseudocubic structure of PMN can be reduced if the Mg^{2+} and Mg^{2+} ions occupy adjacent unit cells throughout the lattice, but this is not possible with Mg^{2+}:Nb^{5+} ratio of 1:2, dictated by the composition $Pb(Mg_{1/3}Nb_{2/3})O_3$. Chen *et al.* [49] and Randall *et al.* [49] have reported transmission electron microscopy (TEM) diffraction patterns of short-range order domains on the scale of 2-5 nm within the pseudocubic structure, just below the transition temperature of PMN. Chen et al. [49] have also proposed that the ratio of Mg^{2+}:Nb^{5+} ions in these domains is 1:1, to give an ordered structure of the type $Pb(Mg_{1/2}Nb_{1/2})O_3$, and that the resulting net negative charge is balanced by positively charged domains with unit cells containing only Nb^{5+} ions. The strong space charge effects between domains in this model predicts that domain wall movement will be restricted. As a refinement of this space-charged domain model, Viehland et al. [50] have suggested that layers within the perovskite structure are occupied exclusively by Nb^{5+} ions, while other layers are occupied randomly by Mg^{2+} and Nb^{5+} ions, to give an ordered structure of the form $Pb(Mg_{1/3}Nb_{2/3})_{2/3}\ Nb_{1/2}O_3$. As the charges created by ordering in this charged balanced

random-layer model are balanced internally within the domains, the model does not predict a restriction on domain wall movement. Yan et al. [52] have later reported that the ordered domain structure they observed by high resolution Z-contract electron diffraction is in agreement with the charge balanced random-layer model of Viehland [50] and inconsistent with the earlier domain space-charge model of Chen [49].

2.1.4.4. The Mechanism of the Relaxor Transition in PMN

The mechanism of the relaxor ferroelectric transition in PMN is still under active discussion. Smolenskii and Agranovska [36] explained the diffuse nature by suggesting that the ferroelectric transition does not occur simultaneously throughout the volume of a relaxor, because of local composition fluctuations of the order of 100-1000 Å, and the dielectric response at the transition temperature was thus interpreted as a switching of local spontaneous polarization between states with different vector orientations. This proposal was supported by the electron diffraction observations of Chen *et al.* [49] and Randall *et al.* [49], but it did not account for the frequency dependent relaxor behaviour. Cross [41] proposed that relaxors should be considered as superparaelectrics with small non-interacting polar regions, each with its own spontaneous polarization, and that the potential barrier for reorientation of 100 Å size regions should be comparable to the thermal energy of the crystal. The temperature and frequency dependence of the transition was thus attributed to a slowing down of the fluctuation of the local polarization vectors. Viehland et al. [53, 53] have compared relaxors to spin glasses, by suggesting that relaxors are composed of non-interacting regions of polarizing fluctuations, which were identified by X-ray line broadening in

$Pb_{1-x}La_xZr_{0.55}Ti_{0.45}O_3$ (PLZT). The frequency dispersion (f_m) observed in the relaxor state was analyzed by the relationship:

$$f_m = f_v \exp(-E_v/k(T_m - T_f) \qquad \text{Equation 2-35}$$

where T_m is the temperature of the peak in dielectric constant for a measurement at a frequency f_v and T_f is the so-called freezing temperature. For PMN, it was found that T_f = 218 K, which is almost coincident with the zero-field de-poling temperature of 213 K, i.e. the temperature below which spontaneous polarization is observed. Glassy behaviour has also been proposed as a mechanism for the relaxor transition by Westphal *et al.* [54] and by Yusin and Dorogovtsev [56].

Bell [56] and Glazounov *et al.* [58] examined two alternatives of the superparaelectric model of an ensemble of independent, nano-sized superparaelectric clusters: - one based on a single transition temperature, with a size range of polar regions - and the other based on a range of temperatures, with a constant polar region size. They showed that the broadened peaks in the temperature dependence of the dielectric constant occur when the size of the polar regions is less than 15 μm, which is of the order of the short range order domains observed by TEM [49, 49, 52]. These authors thus demonstrated that the broadening of the dielectric peak is solely a function of the size of the correlated polar regions with <111> rhombohedral distortions and that the temperature T_m does not represent a true structural change. In an extension of the model, the authors considered that the size of the polar regions, and the coupling between them, are increased as the temperatures are lowered. They found that a combination of both effects gave the best fit

to available relaxor data for PMN, and also provided a rationale for the onset of the spontaneous polarization observed at temperatures below T_f [56, 58].

2.1.5. Thermodynamic Treatment of Ferroelectrics

The change in internal energy of a body that is subjected to external stresses and electric fields has been analysed by Fattuzzo and Merz [12] according to the following differential equation:

$$\partial U = T\Delta S - \sum_{i=1}^{3} X_i dx_i + E \cdot dP \qquad \text{Equation 2-36}$$

where:

S:	entropy
T:	temperature
X_1:	stress
x_1:	strain
E:	electric field
P:	polarization

The Helmholtz free energy and the elastic Gibbs function can be defined (in terms of these same properties) in the following equations [12, 60]:

Helmholtz: $A = U - TS$ Equation 2-37

Gibbs: $G = U + \sum_i X_i x_i - TS$ Equation 2-38

From the above definitions the equations take the following differential form [12]:

$$dA = -SdT - \sum_{i=1}^{3} X_i dx_i + E \cdot dP \qquad \text{Equation 2-39}$$

$$dG = -SdT + \sum_{i=1}^{3} x_i dX_i + E \cdot dP \qquad \text{Equation 2-40}$$

Since the Gibbs function is in terms of temperature, stress and polarization; it is typically the most convenient potential function to use. When the stress is assumed to be zero, the equation for G can be expanded in powers of polarization (where the coefficients are a function of temperature), as follows [12]:

$$G = G_0 + \frac{1}{2}X'(P_X^2 + P_Y^2 + P_Z^2) + \frac{1}{4}\xi'(P_X^4 + P_Y^4 + P_Z^4) + \frac{1}{2}\lambda'(P_X^2P_Y^2 + P_Z^2P_X^2 + P_Y^2P_Z^2) + \frac{1}{6}\varsigma'(P_X^6 + P_Y^6 + P_Z^6) + \frac{1}{6}\eta'(P_X^2P_Y^2P_Z^2 + ..., \quad \text{Equation 2-41}$$

where:

G_0 is the free energy for zero polarization. This value is often set to zero. Provided the polarized phase below the Curie temperature is treated as a slight distortion of the paraelectric state that occurs above the T_C, Equation 2-41 can apply to the entire temperature range. When it is required to investigate the strain that accompanies polarization in the cubic system, a similar expansion can be performed for the Helmholtz free energy equation. Since the Gibbs equation in most commonly used, it can be rewritten into the form [12]:

$$G = G_0 + \frac{1}{2}\alpha P^2 + \frac{1}{4}\gamma P^4 + \frac{1}{6}\delta P^6 \quad \text{Equation 2-42}$$

where:

α, γ and δ are new coefficients
$P = P_Z$, ($P_X = P_Y = 0$).

Then, differentiating the previous equation yields the following expression:

$$\frac{\partial G}{\partial P} = E = \alpha P + \gamma P^3 + \delta P^5 \quad \text{Equation 2-43}$$

By substituting $\alpha = \beta(T\text{-}T_0)$ into equations 2-42 and 2-43 the resulting equations are derived [12, 61] :

$$G = G_0 + \frac{1}{2}\beta(T - T_0)P^2 + \frac{1}{4}\gamma P^4 + \frac{1}{6}\delta P^6 \qquad \text{Equation 2-44}$$

$$\frac{\partial G}{\partial P} = E = \beta(T - T_0)P + \gamma P^3 + \delta P^5 \qquad \text{Equation 2-45}$$

The relevance of equations 2-42 to 2-45 is in the γ coefficient, which determines whether the equation is defining a first order transition (γ is negative) and a second order transition (γ is positive). The first order transition on cooling from the paraelectric state to the ferroelectric state is accompanied by latent heat and a discontinuity in the specific heat. The second order transition takes place without latent heat but has a peak in specific heat [12]. The equations need only extend to the P^4 term as this is adequate for a second order transition, although not entirely accurate [56].

Figure 2-27 demonstrates the relationship of the Gibbs free energy (G) to the polarization (P) at various temperatures. The temperatures of interest are T_0, T_C, T_1 and T_2 which are defined with respect to $BaTiO_3$ as [12]:

$T_0 = T_C - 7.7\ °C$

$T_C = 120\ °C$

$T_1 = T_0 + 10\ °C$

$T_2 = 175\ °C$

For $BaTiO_3$ the variable γ which is dependent on temperature is also of interest and is defined as [12]:

$$\gamma = 18 \times 10^{-15}(T - T_2) \qquad (2\text{-}46)$$

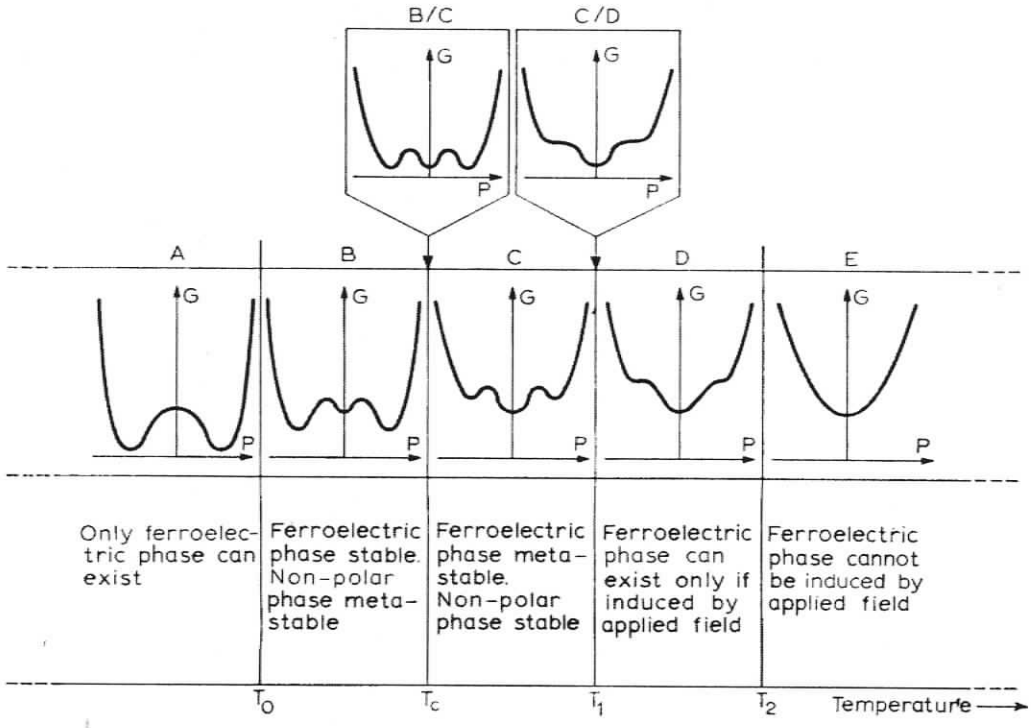

Figure 2-27 Free energy functions (at temperature) for a ferroelectric with first order transitions [12]

It should be noted that as $T \rightarrow T_2$, $\gamma \rightarrow 0$ and since T_C is less than T_2, γ takes a negative value. In relation to the electrocaloric effect, entropy of the crystal is held constant during sudden changes in polarization. To balance the energy of the crystal, the temperature of the crystal will vary accordingly. Fattuzzo and Merz define the maximum corresponding change in temperature as 2 °C near T_C (where the polarization changes sharply from P = maximum to P = 0) for $BaTiO_3$.

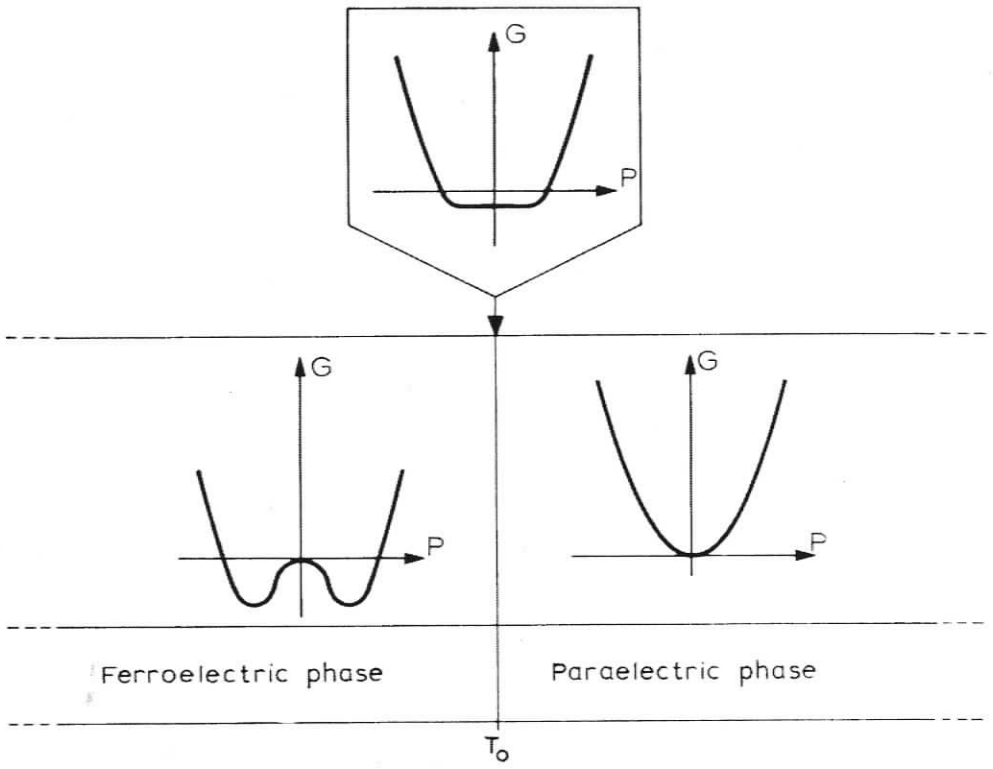

Figure 2-28 Free energy functions (at temperature) for a ferroelectric with 2nd order transitions [12]

Figure 2-28 shows the Gibbs free energy for a second order transition at temperatures below and above the Curie-Weiss temperature (T_0). The polarization (P_0) induced by a bias field (B) in the paraelectric state, i.e. above the Curie point of a ferroelectric, is illustrated in Figure 2-29. The Curie point (or Curie temperature) is at $T = T_C$ which is the maximum transition point for the dielectric constant. This maximum point for the dielectric constant (T_C) will shift to higher temperatures when the bias filed is applied and

is then referred to as T*; whereas, the position of the Curie-Weiss temperature (T_0) is not affected by the bias field [12].

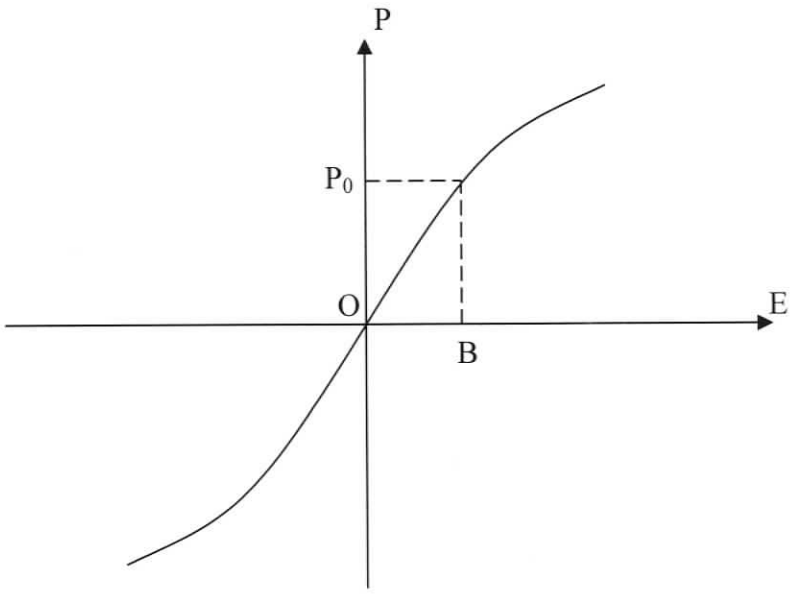

Figure 2-29 Polarization (P) induced by the bias (B) above the Curie point [12]

2.2. Piezoelectric and Electrostrictive Ceramic Systems

2.2.1. Lead Zirconate Titanate (PZT) Piezoelectrics

2.2.1.1. Optimum Compositions

The dielectric and piezoelectric properties of $BaTiO_3$ are prone to excessive aging, because its transition temperature of T_C = 130 °C is not very far above the ambient. As shown in Figure 2-30, Pb^{2+} is the only substitutional divalent ion that causes T_C to be increased. However, while the T_C of the terminal phase $PbTiO_3$ (PT) at 480 °C solves the aging problem, it becomes more difficult to pole the ceramics, as this operation is normally conducted in an insulating oil. The T_C can be lowered to an optimum temperature in the region of 350 °C, by the partial replacement of Ti^{4+} by Zr^{4+}, as shown in Figure 2-31. This diagram also shows that $PbTiO_3$ (PT) and $PbZrO_3$ (PZ) form a continuous series of substitutional solid solutions at high temperatures, but on cooling through T_C the richer PT compositions form the tetragonal perovskite structure, while the PZ rich compositions form the rhombohedral perovskite structure. The tetragonal and rhombohedral phases are separated by a so-called morphotropic phase boundary (MPB) across which the phase change is effected by a rotation of the direction of the polarization vector from [100] to [111], without any ion movement to disturb nearest neighbour ions. It is also evident from the figure that a ceramic of composition $52PbZrO_3$–$48PbTiO_3$ can be poled in the tetragonal phase and then transformed to the rhombohedral phase on subsequent cooling. Ceramics that are processed in this manner have been shown to have the highest dielectric and piezoelectric properties [59].

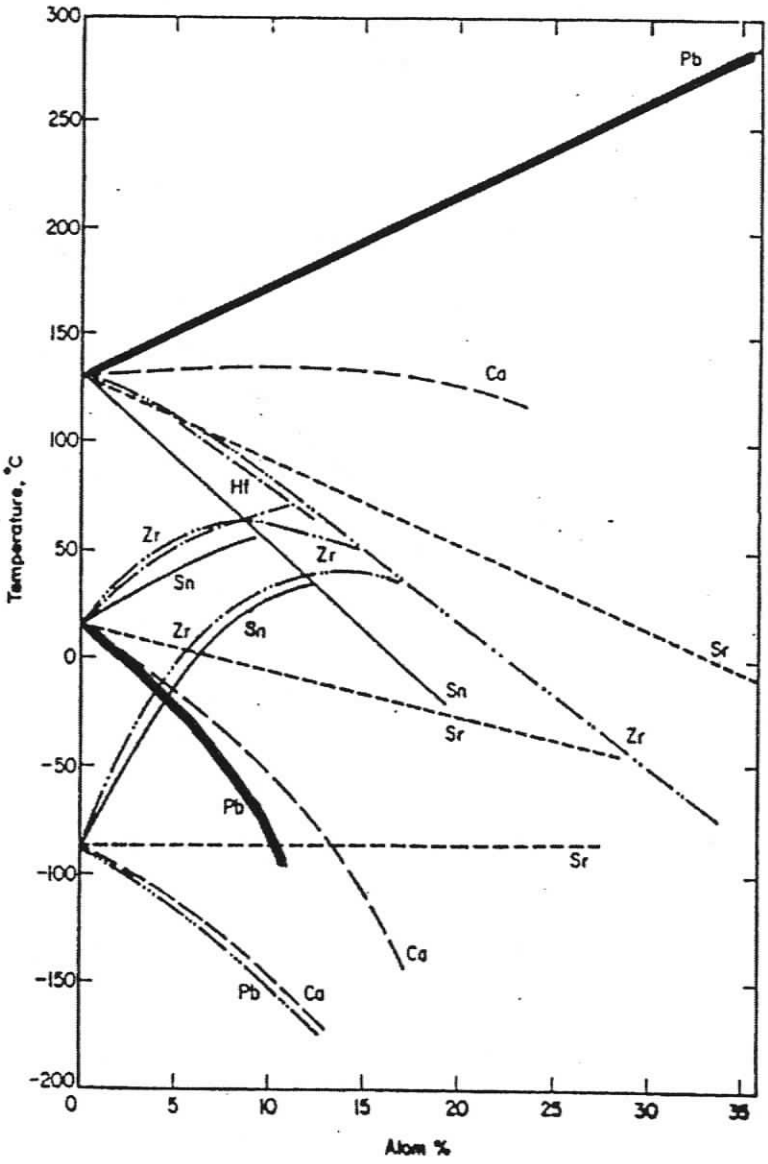

Figure 2-30 Effect of isovalent substitutions on transition temperatures of $BaTiO_3$ [5]

A series of six types of piezoelectrics based on this PZT composition, with selective doping, have been specified by the US Navy for various sensor and actuator applications, as shown in Table 8-1 in the Appendix [62]. Hard piezoelectrics are obtained by doping

with oxides such as Cr_2O_3, Co_2O_3, NiO, Rh_2O_3, IrO_2 and Sc_2O_3 [59]. These small diameter divalent or trivalent ions substitute for Ti^{4+}, or Zr^{4+}, and migrate to preferred sites in the ferroelectric domain walls, where they create space charges that restrict domain wall movement. Soft piezoelectrics are developed by doping with oxides such as La_2O_3, Nb_2O_5, Ta_2O_5, Sb_2O_3, Bi_2O_3, WO_3 and ThO_2 [59]. When these larger polyvalent ions substitute for Pb^{2+}, vacancies are created at the Pb sites, so that the mobility of the domain walls is increased. Other dopants such as Fe_2O_3, Cr_2O_3, MnO_2, WO_3 and Al_2O_3 are also added to improve the aging characteristics of the piezoelectrics [25].

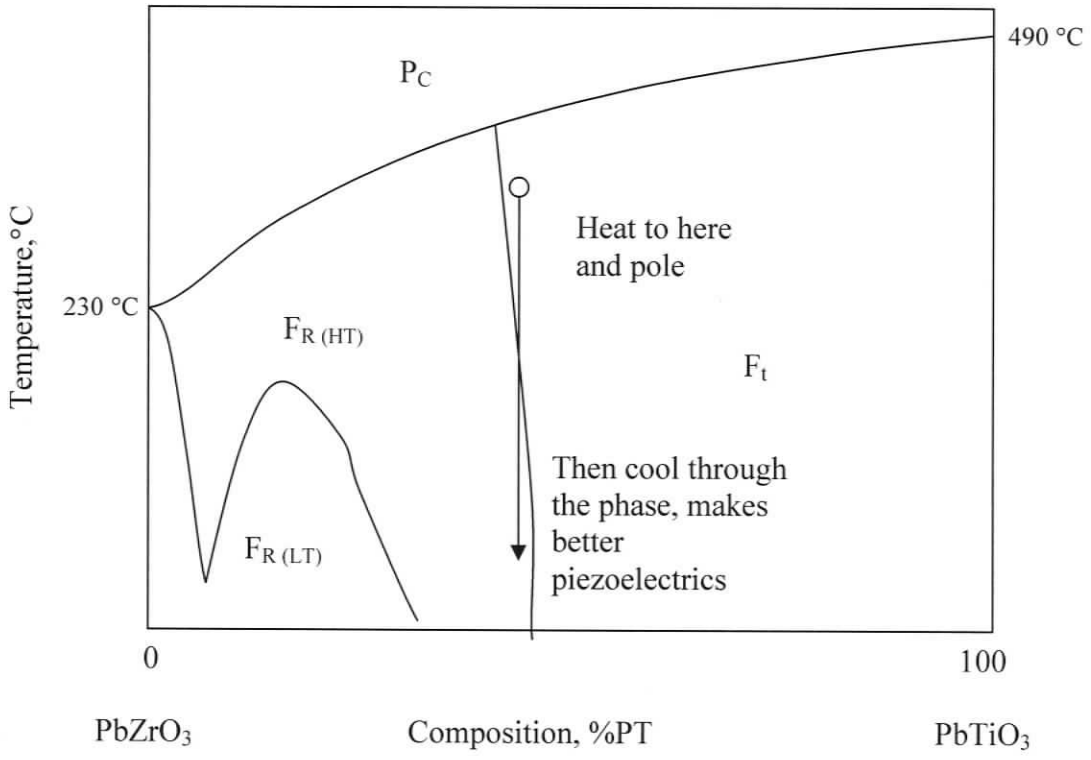

Figure 2-31 The lead-titanate, lead- zirconate (PZT) system [5, 62]

Proprietary compositions to meet the US Navy specifications have been developed by several manufactures. Relevant BM designations developed by Sensor Technology, Ltd.,

of Collingwood, ON are included in Table 8-4 (in the Appendix), since a number of these ceramics are used in the experiments to be described later.

2.2.1.2. Hard and Soft PZT ceramics

The typical properties listed in Table 2-2 show that hard piezoelectrics for use as sonars, sensors and high power transducers, have high Curie temperatures, coercive fields and mechanical quality, combined with low dissipation factors, piezoelectric hysteresis and linearity factors, with moderate dielectric constants, coupling factors and aging. Soft PZT piezoelectrics for use as actuators, and low power resonators, have high dielectric constants, d-constants and coupling coefficients, combined with low Curie temperatures, mechanical quality, and aging characteristics, with moderate coercive fields and dissipation factors. These beneficial properties of the soft piezoelectrics are offset by relatively large piezoelectric hysteresis and deviation from linearity factors.

Table 2-2 Characteristics of hard and soft piezoelectrics [6]

	Hard Piezoelectrics		Soft Piezoelectrics	
	Value	Comment	Value	Comment
Curie Temp.	$T_c > 300$ °C	High	$T_c < 200$ °C	Low
Dielectric Const.	K = 100 - 1750	Medium	K = 2750 - 3250	High
Dissipation Fact.	$\tan\delta = 0.3 - 0.4$ %	Low	$\tan\delta = 1.6 - 2.0$ %	Moderate
Coercive field	$E_c = 1.88$ MV/m	High	$E_c = 0.88$ MV/m	Med-high
d-constants	$d_{33} = 225 \times 10^{-12}$ m/V	Small	$d_{33} = 600 \times 10^{-12}$ m/V	Med-large
	$d_{31} = 100 \times 10^{-12}$ m/V	Small	$d_{31} = 275 \times 10^{-12}$ m/V	Med-large
Piezo. Hysteresis	~ 2 %	Low	15 -20 %	High
Piezo. Linearity	~ 1 %	Good	2-10 %	Larger
Coupling Factor	k = 0.3 – 0.6	Moderate	k = 0.4 – 0.7	High
Mechanical Q	$Q_M = 500 - 1000$	Good	$Q_M = 70 - 80$	Low
Ageing	Ageing rate = 2 - 6	Moderate	Ageing rate = 0.5 – 1.0	Low
Applications	Sonar sensors, high-power transducers		Actuators, low-power resonators	

2.2.1.3. Applications of PZT Piezoelectrics

Figure 2-32 shows the piezoelectric effect for a poled ceramic under conditions of no stimulation, i.e. no applied stress (pressure) and voltage. When the piezoelectric element is used as transducer, the applied stress generates a voltage signal that can be used in a sensor or load cell. The prime piezoelectric property in this context is the coupling coefficient "k", which indicates the fraction of mechanical energy converted to electrical energy [26] and this parameter is thus used for comparing transducer materials.

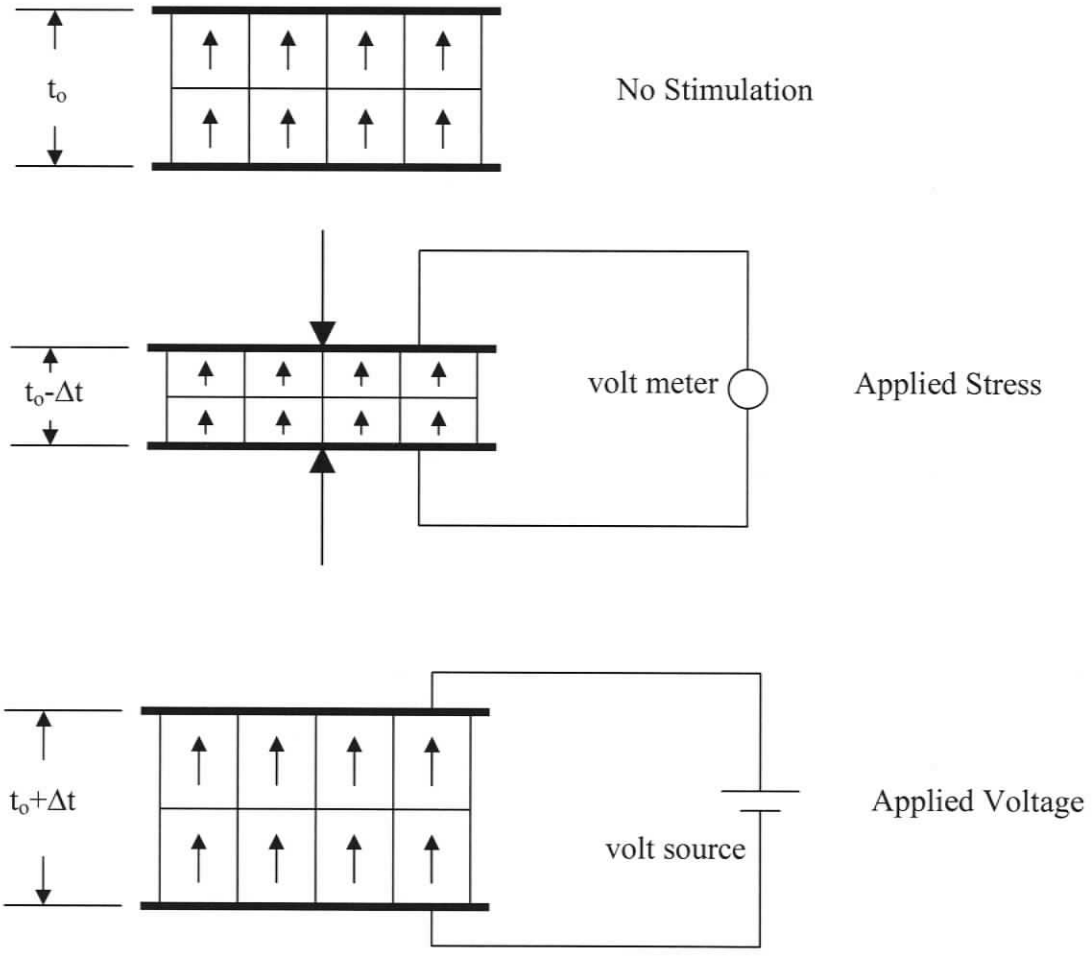

Figure 2-32 Piezoelectric effects (schematic)

When the piezoelectric element is used as an actuator, the applied voltage generates a displacement that can be used to operate a smart system. The prime piezoelectric property in this context is the magnitude of the piezoelectric d-constant, which governs the extension available for a given voltage.

2.2.2. Lead Magnesium Niobate-Lead Titanate (PMN-PT) Ceramics

2.2.2.1. Dielectric Transitions and Structural Transformations

In spite of its enhanced electrostrictive properties, the relaxor PMN is impractical for most engineering applications, because its transition temperature of -18 °C [38] is below the ambient. This temperature can be raised above room temperature, however, by substituting Ti^{4+} ions for the Mg^{2+} and Nb^{5+} ions at the body centre positions of the PMN perovskite unit cell shown previously in Figure 2-25. These solid solution ceramics are represented by the chemical formula $(1-x)[Pb(Mg_{1/3}Nb_{2/3})O_3]-x[PbTiO_3]$, which it is conveniently shortened to PMN-xPT, where x is the mole% of $PbTiO_3$.

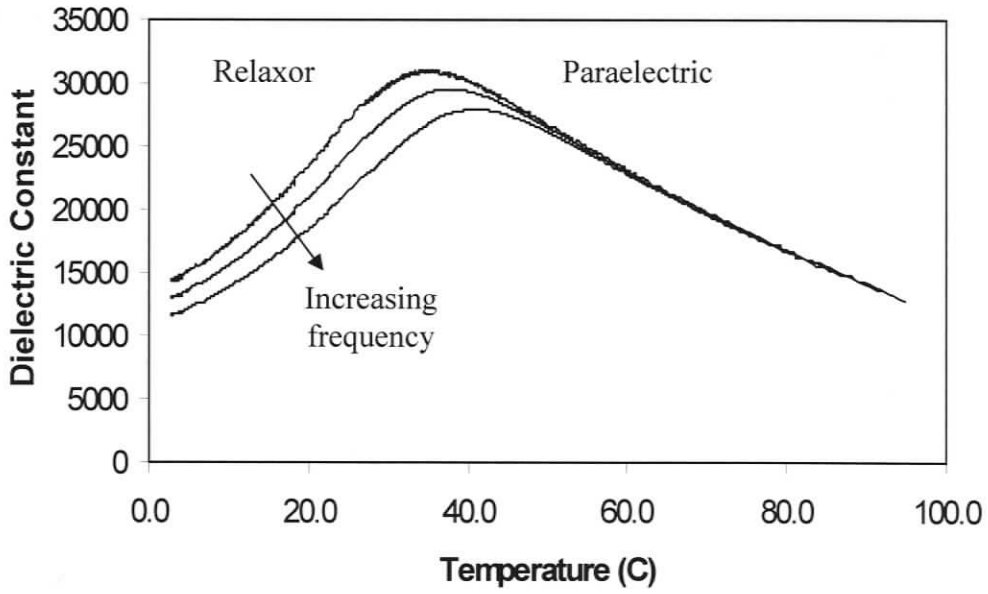

Figure 2-33 Graph of dielectric constant vs. temperature for PMN-0.10PT [1, 7, 64, 65, 66]

The raising of the temperature of the relaxor region of PMN by the addition of PT is illustrated by the results of Waechter et al. [64], which shows the temperature dependence of the static dielectric constant of a ceramic of composition PMN-0.1PT. As shown in Figure 2-33, the dielectric constant of this sample exhibits a broad peak with a maximum at a temperature T_m, which lies in the region of 38 °C [64]. It is also evident from Figure 2-33 that, as observed in PMN, the magnitude of this peak is diminished, and temperature of the maximum dielectric constant is moved to higher temperatures, when the measurements are made at increasing frequencies.

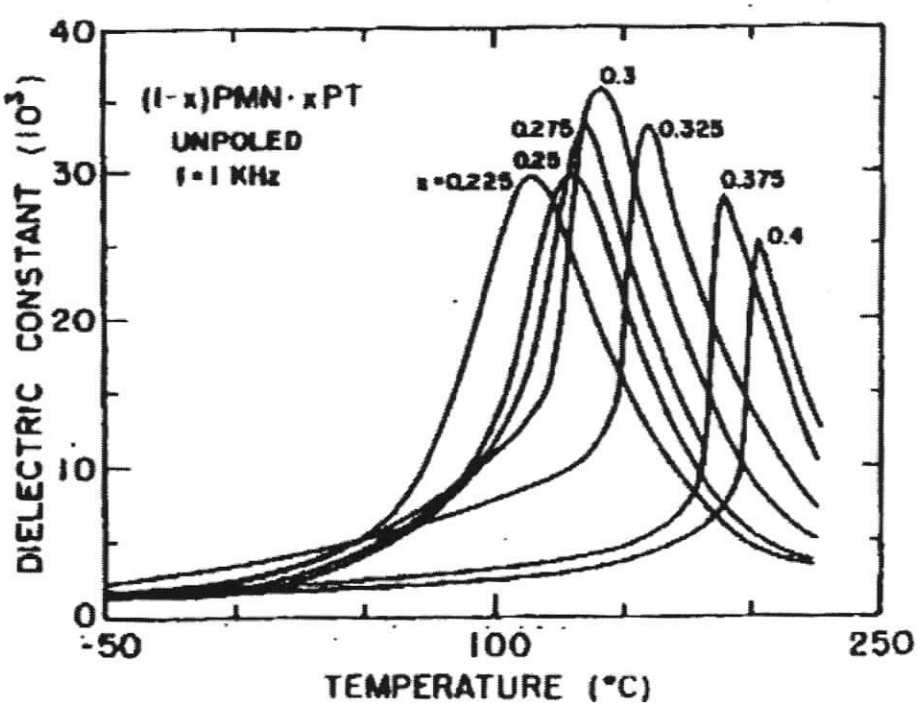

Figure 2-34 Dielectric behaviour of PMN-xPT ceramics vs. Temperature @ 1 kHz [67]

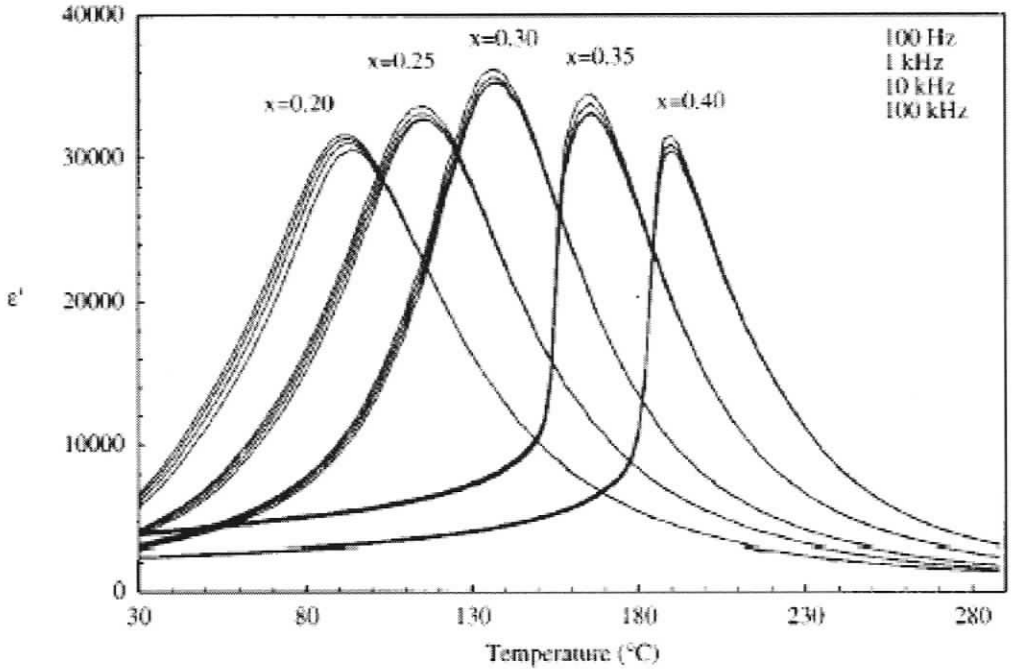

Figure 2-35 Dielectric behaviour of PMN-xPT ceramics vs. Temperature @ various Hz [68]

The effect of further increases in PT composition on the temperature of the relaxor transition in PMN–PT ceramics is illustrated in Figures 2-34 and 2-35, which show the temperature dependence of the dielectric constant K, or the real part of the permittivity e', reported by Choi et al. [67] and Noblanc et al. [68]. Both figures show that the temperature T_m of the maximum in dielectric constant increases with increasing additions of PT. The peaks in Figure 2-35 also display the relaxor effect, i.e. a decrease in peak height and a shift to higher temperatures with increasing frequency of the measuring electric field. While all of the plots deviate from the Curie-Weiss law at higher temperatures, a distinct change in the shape of the peaks occurs between 0.3PT and 0.4PT. For compositions above 0.325PT, the peaks are distinctly asymmetric (typical of a

normal ferroelectric transition), but still show a small degree of frequency dependence around the temperature T_m. As expected, these compositions were found to display more normal piezoelectric properties, as opposed to the electrostrictive properties observed at the lower PT compositions [68].

The addition of PT to PMN has the additional advantage that the substitution of Ti^{4+} ions for Mg^{2+} & Nb^{5+} ions reduces the amount of Nb^{5+} in the ceramic, so that the impurity phase $Pb_2 Nb_2 O_7$ is less likely to form with increasing mole fractions of PT [69]. The compound $Pb_2 Nb_2 O_7$ is very difficult to prevent, and remove, during the synthesis of PMN ceramics [33]. This very stable phase has the cubic pyrochlore structure, with m3m centrosymmetry, and thus significantly reduces the electrostrictive properties of PMN [2]. Laboratory samples of pyrochlore free PMN have been produced by Ho *et al.* [69] using freeze-drying and spray-drying methods to activate the precursor powders. Pyrochlore free industrial powders and ceramics of PMN-PT ceramics have also been prepared by Sensor Technology, Ltd., Collingwood, ON, in collaboration with the Ceramics Laboratory of NRCAN, Ottawa, ON, using a refined grinding, pressing and sintering technique [72, 73].

2.2.2.2. Physical Properties of PMN-PT Ceramics

Table 2-3 Characteristics of PMN-PT Electrostrictors and Soft PZT Piezoelectrics [6]

	Soft Piezoelectrics		PMN-0.1PT	
	Value	**Comment**	**Value**	**Comment**
Curie Temp.	$T_C < 200$ °C	Low	$T_m = 38$ °C	Near RT
Dielectric Const.	K = 2750 - 3250	High	K =22,000	Very high
Dissipation Fact.	tan δ = 1.6 – 2.0 %	Moderate	tan δ = 0.08	High
Coercive field	$E_C = 0.88$ MV/m	Med-high	N/A	
d-constants	$d_{33} = 600 \times 10^{-12}$ m/V	Med-large	$d_{33} = 650 \times 10^{-12}$ m/V	Med-large
	$d_{31} = 275 \times 10^{-12}$ m/V	Med-large	$d_{31} = 290 \times 10^{-12}$ m/V	Med-large
Piezo. Hysteresis	15 -20 %	High	-----	Very low
Piezo. Linearity	2-10 %	Larger	-----	
Coupling Factor	k = 0.4 – 0.7	High	k = 0.41 – 0.55	Med-high
Mechanical Q	$Q_M = 70 – 80$	Low	-----	
Ageing	Ageing rate = 0.5 – 1.0	Low	-----	
Applications	Actuators, low-power resonators		Actuators	

The electrostrictive properties of a typical PMN-PT relaxor ferroelectric are compared to the properties of a soft PZT piezoelectric in Table 2-3. The Curie temperatures of the relaxors tend to be relatively close to room temperature, as the increase in T_m obtained with increasing PT composition is offset by the increasing degree of piezoelectric properties, as discussed above. The relaxor ceramics have exceptionally high dielectric constants and high tan δ dissipation factors. The d-constants are only slightly greater than those of the soft piezoelectrics and their coupling factors are very slightly lower. However, their real advantage lies in the very low hysteresis, and deviation from linearity, observed in strain vs. field plots. The electromechanical properties of relaxors do not display aging characteristics, because they do not sustain remanent polarization,

on removal of an applied field. The PMN-PT relaxors are thus being developed for actuator applications in which a high degree of control and reversibility is required, particularly for micromanipulation.

Electrostrictive PMN-PT compositions are subjected to a dc biased electric field (E_{dc}), to align the nano-polar regions, for use in transducer applications. When an AC field is superimposed upon the DC bias field, the ceramic acts in a piezoelectric manner with an effective piezoelectric coefficient, d*, [70, 71]:

$$d^* = \Delta S/E_{ac} \qquad (2\text{-}47)$$

It has been shown that the $*d_{33}$ and $*d_{31}$ coefficients of pure PMN and PMN-PT in a field induced state, display a very weak ageing rate within the experimental time scale, at temperatures near the dielectric maximum temperature (T_m) [70].

2.2.2.3 Phase Diagrams for the PMN-PT Ceramic System

In ferroelectric perovskite-based ceramics, such as BM532, etc., the temperature of the dielectric transition from paraelectric to ferroelectric, and the accompanying structural change from cubic to tetragonal, are almost coincident, so phase diagrams for ceramic systems such as PZT are commonly based on the compositional dependence of the temperatures of the dielectric transitions. Following this practice, Choi et al. [67] produced the "phase diagram" for the PMN-PT system shown in Figure 2-36, which has been widely quoted by other investigators (see for example: 70, 74). The data points, which refer to measured values of T_m in the relaxor region (see Figure 2-34), and T_C

values in the ferroelectric region, fall on two linear plots, which are displaced slightly in the region of 0.29PT. This discontinuity between T_m and T_C is most likely an artifact, due to the level of accuracy of the experimental methods, since more recent studies have shown that the compositional dependence of T_C is strictly linear from PMN up to a composition of PMN-0.45PT [68, 75]. Choi et al. [67] made no measurements to

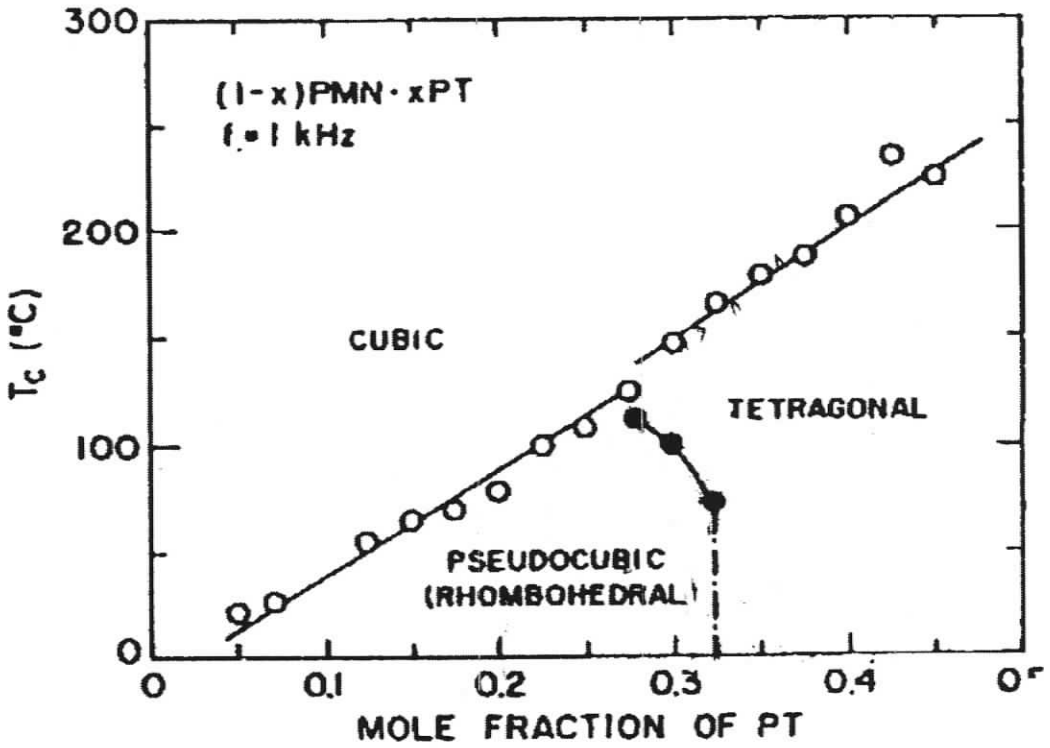

Figure 2-36 Graph of dielectric constant vs. temperature for PMN-0.10PT [67]

determine the composition and temperature dependence of the morphotropic phase boundary (MPB) that occurs between the relaxor region and the normal ferroelectric region. They simply drew in a vertical line in the region of PMN-0.32PT and added some curvature as it approached and intersected the T_C plot, as shown in the figure. The diagram produced by Choi et al. [67] thus represents the compositional and temperature

dependence of the dielectric states (as opposed to the structural forms) of ceramics in the PMN-PT system.

It is common practice [67] to insert the structural phases associated with the dielectric states defined in diagrams such as Figure 2-36. At the time when Choi et al. produced their diagram of the PMN-PT ceramic system, the paraelectric state was associated with the centrosymmetric cubic perovskite structure, the relaxor state with a pseudocubic structure containing dispersed polar regions with rhombohedral distortions, and the ferroelectric state with the polar tetragonal structure [48]. The T_C derived from the sharp increase in dielectric constant observed at the onset of spontaneous polarization in the ferroelectric region (i.e. above 0.3PT) is expected to lie very close to the temperature of the first order phase change from the cubic perovskite to the tetragonal structure [5]. However, the common assumption that the T_m versus composition plot in the relaxor region (derived from the maxima of broad dielectric peaks) is coincident with a sharp phase boundary associated with the second order phase change between the cubic and pseudocubic structures has not been questioned. Since the relaxor transition occurs over a range of temperature, as shown in Figures 2-22, 2-34 and 2-35 there should be a two phase region, rather than a sharp boundary between the structural regions on the diagram. Further, any analysis of the structural transformation between the cubic perovskite structure and the pseudocubic structure should also take into account the intense lattice stiffening, indicated by a distinct decrease in thermal expansion coefficient, that has been regarded as a criterion for identifying the relaxor transition [38, 38, 41], as discussed in Section 2.1.4.2 above.

A further phase diagram for the PMN-PT system ceramic system has been produced by Noblanc et al. [68], based on impedance measurements and high resolution X-ray powder diffraction. As these authors were primarily interested in defining the precise form, and location, of the morphotropic phase boundary between the relaxor and the ferroelectric regions, they only examined compositions between PMN-0.2PT and PMN-0.4PT. As shown in Figure 2-38, they used published data for T_m in the relaxor region below PMN-0.2PT, to link up with their higher PT composition T_m and T_C results in Figure 2-35. They also included published data for the de-poling temperature T_d at lower PT compositions of the de-poling temperature T_d [75, 76], to link up with their results for the maximum temperature at which the rhombohedral structure was observed in poled samples. It should be noted that T_d lies very close to the freezing temperature T_f of Viehland et al. [53, 53] defined in Section 2.1.4.4. The X-ray diffraction results of Noblanc et al. [68] for the temperature of onset of the cubic - tetragonal phase transformation fall on the compositional dependence of the T_d plot. The cubic and tetragonal phases coexist over a temperature range of about 30 °C at a composition of 0.2PT, but the range of coexistence of these phases goes to zero at the composition PMN-0.4PT, at which the T_d plot intersects the T_C plot. The X-ray diffraction results indicated that the temperature of the onset of a lower temperature phase transformation from tetragonal to rhombohedral is independent of composition and that this phase transformation does not go to completion at room temperature, where the amount of rhombohedral phase is 90% in PMN-0.25, but only 20% in PMN-0.4PT. This finding is the first time that a phase diagram for the PMN-PT system has acknowledged that two-

phase regions can exist in ferroelectric systems. Noblanc et al. did not determine the location of the MPB, or the boundary between the pseudocubic and the rhombohedral phases, but in place of the usual vertical lines, they inserted curved dotted lines that covered ranges of composition, as shown previously in Figure 2-36.

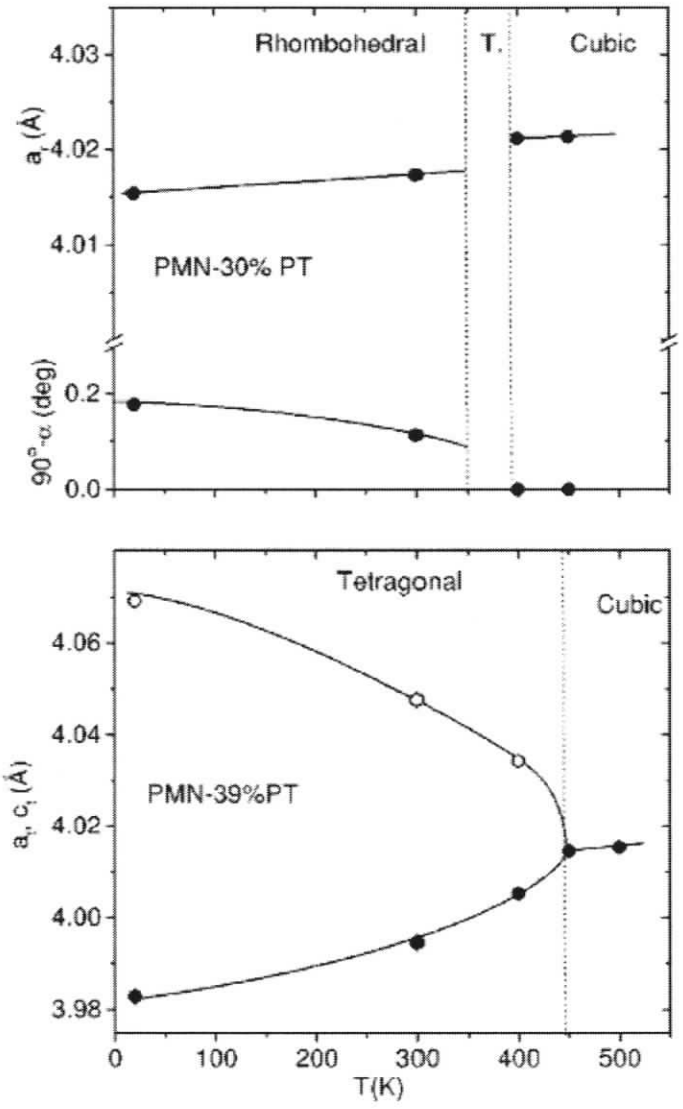

Figure 2-37 Lattice parameters vs. Temperature for a) 0.30PT (M_A) b) 0.39PT (M_C) [83]

The composition region of the MPB in the PMN-PT system has been extensively studied by a variety of sophisticated techniques during the last two to three years. When samples were cooled in an applied electric field, it was also shown that the modification of PMN with additions of PT results in a gradual change from relaxor to normal ferroelectric behaviour for compositions of PMN-≤0.34PT, while normal ferroelectric behaviour occurs at compositions of PMN->0.35PT [78]. Single crystals of PMN-0.33PT poled along the [101] direction are reported to be orthorhombic [78]. PMN-0.35PT single crystals poled along the [001] direction exhibited the M_A type of monoclinic symmetry

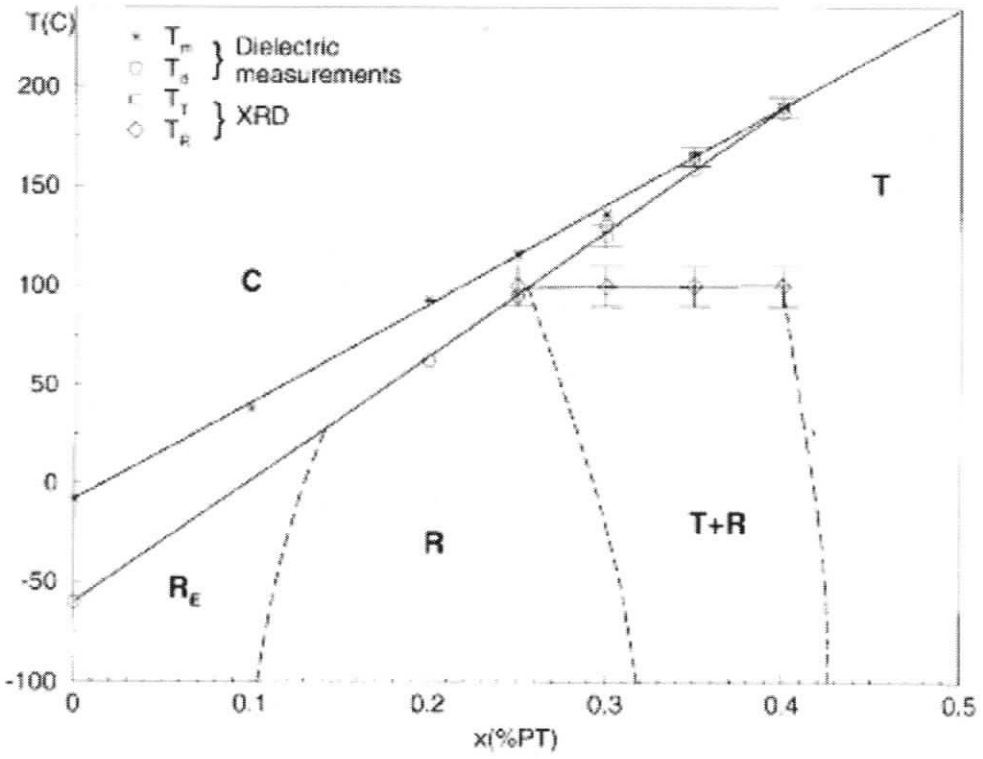

Figure 2-38 PMN-PT phase diagram using XRD and dielectric measurements [68]

shown in Figure 2-37A, while unpoled crystals of this composition have the rhombohedral structure [79]. The M_C type of monoclinic symmetry (see Figure 2-37B)

has been observed in PMN-0.35PT at low temperatures and in PMN-0.34PT at room temperature [80, 81].

On the basis of synchrotron radiation experiments, Noheda et al. [83] have produced the modified phase diagram for the MBP region of the PMN-PT system shown in Figure 2-39. In contrast to the phase diagram of Noblanc [68], they insert the M_C monoclinic phase in place of the low temperature rhombohedral structure, and the temperature of the decomposition of the tetragonal phase is no longer constant temperature, but decreases steeply with increasing fractional composition of PT between 0.3 and 0.4. These authors also state that the region labelled M_C is not a homogeneous phase, because secondary

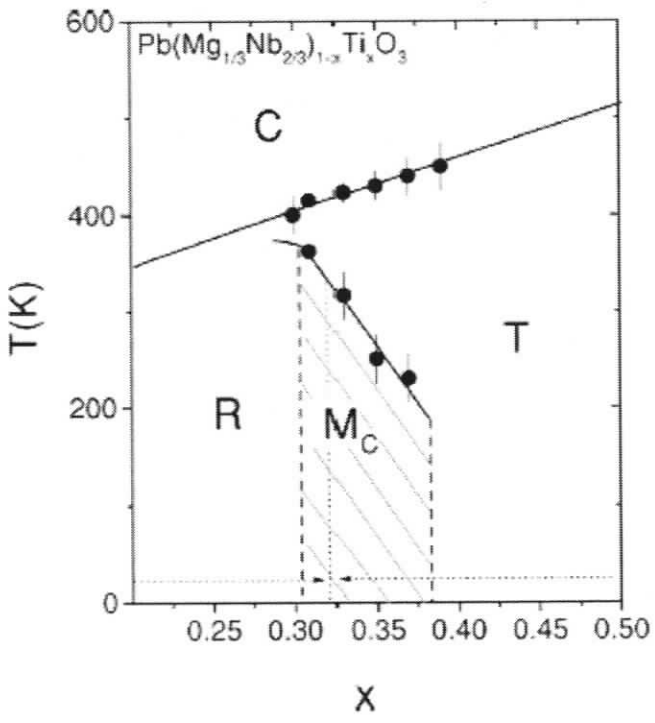

Figure 2-39 PMN-PT phase diagram using XRD and dielectric measurements [83]

phases with tetragonal, rhombohedral or orthorhombic symmetry are also present. Further, while Noblanc et al. [68] showed an MPB with a pronounced negative slope,

Noheda et al. [83] delineate the composition boundaries of the M_C region by vertical dotted lines at 0.31 and 0.37 mole fractions of PT.

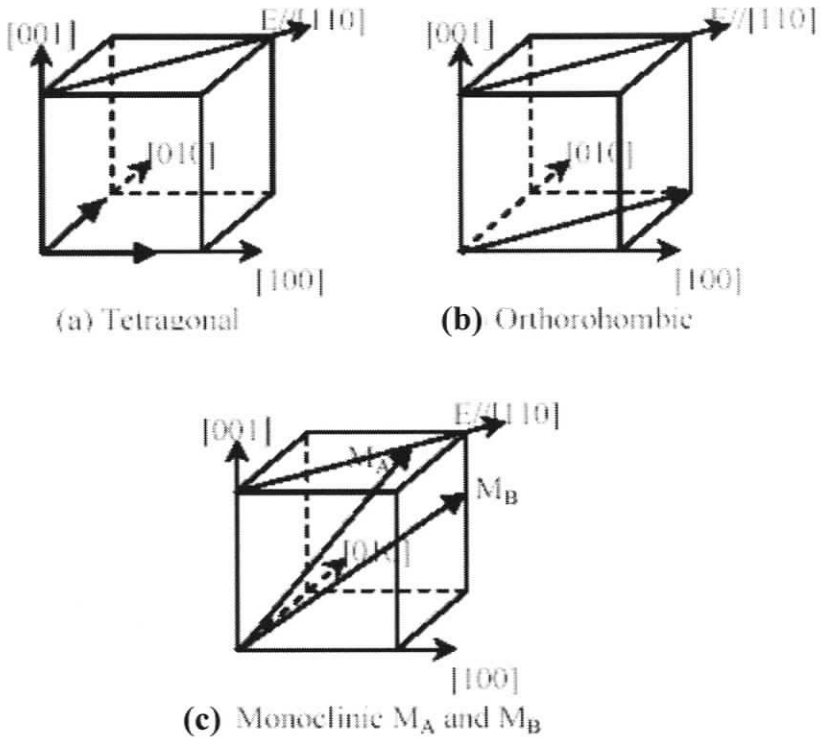

Figure 2-40 Schematic of tetragonal, orthorhombic and monoclinic MC phases in PMN-30% PT with E along [110]. Arrows indicate the polar vector. Panels (a) are twin domains developed in the tetragonal phase and only two polarizations are constrained within (001) plane; panel (b) shows the single domain developed in the orthorhombic phase; and panel (c) indicates the domains developed in the MB/MA phase, in which the polarization vectors are constrained with the (110) plane [85]

In more recent studies of the MPB region of the PMN-PT phase system, single crystals of composition PMN-0.3PT have been examined by neutron scattering and X-ray diffraction to determine the sequence of structures that occur when samples are cooled in, or subjected to, an electric applied on different directions with respect to the crystal axes. Bai et al. [84] have shown that cooling in the absence of an applied field gives the

sequence cubic - tetragonal - rhombohedral; cooling in an applied field along [001] gives cubic - tetragonal - monoclinic M_C - monoclinic M_A; while the application of an applied field along [001] to a sample cooled in zero field gives rhombohedral - monoclinic M_A - monoclinic M_C- tetragonal. On the other hand, Cao et al. [85] have shown that for crystals cooled in a field along [110], the phase sequence is cubic – tetragonal – orthorhombic - monoclinic M_B (see Figures 2-40 and 2-41), while the application of a

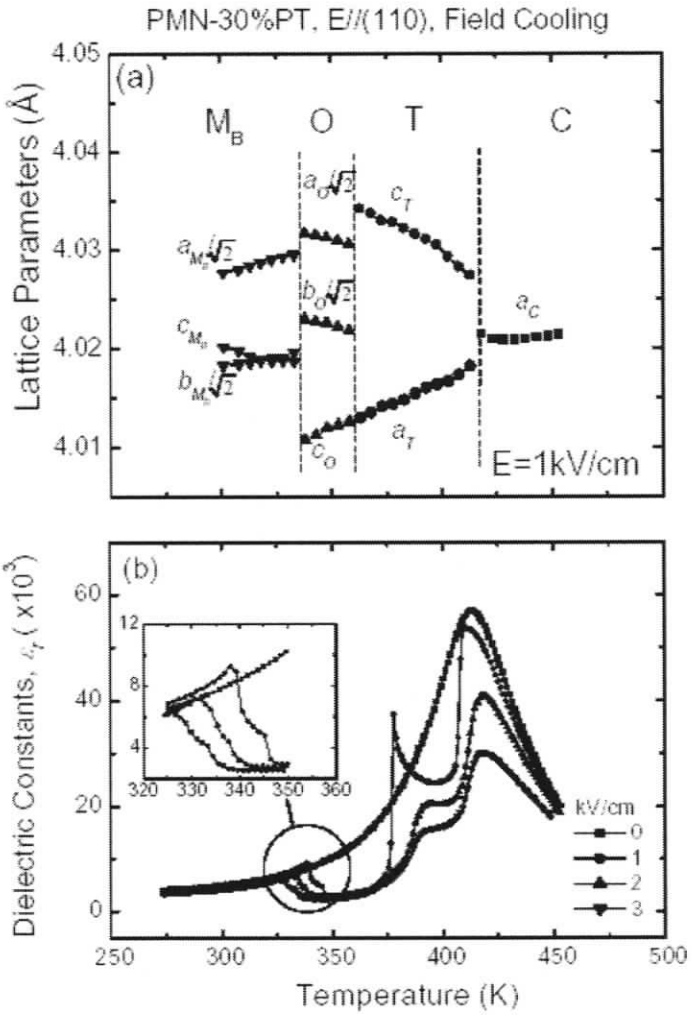

Figure 2-41 Lattice parameter vs. Temperature for PMN-0.30PT, M_B phase [85]

field along this direction to a crystal cooled in zero field gives the sequence rhombohedral - M_B - orthorhombic. These findings indicate that the phase diagram of Noheda et al. [83] should be modified to include a transformation from the M_C phase to the rhombohedral phase, but none of the recent authors have put forward new phase diagrams, even though some of them are close colleagues of Noheda.

Recent studies of the relaxor region of the PMN-PT system have exposed a controversy between researchers using powder samples and those using single crystals. Examining powder samples by high resolution X-ray diffraction and neutron diffraction, B. Dkhil et al. [45], observed a first order transformation from the pseudocubic relaxor structure to a rhombohedral ferroelectric structure at temperatures below ~12°C, as illustrated by the

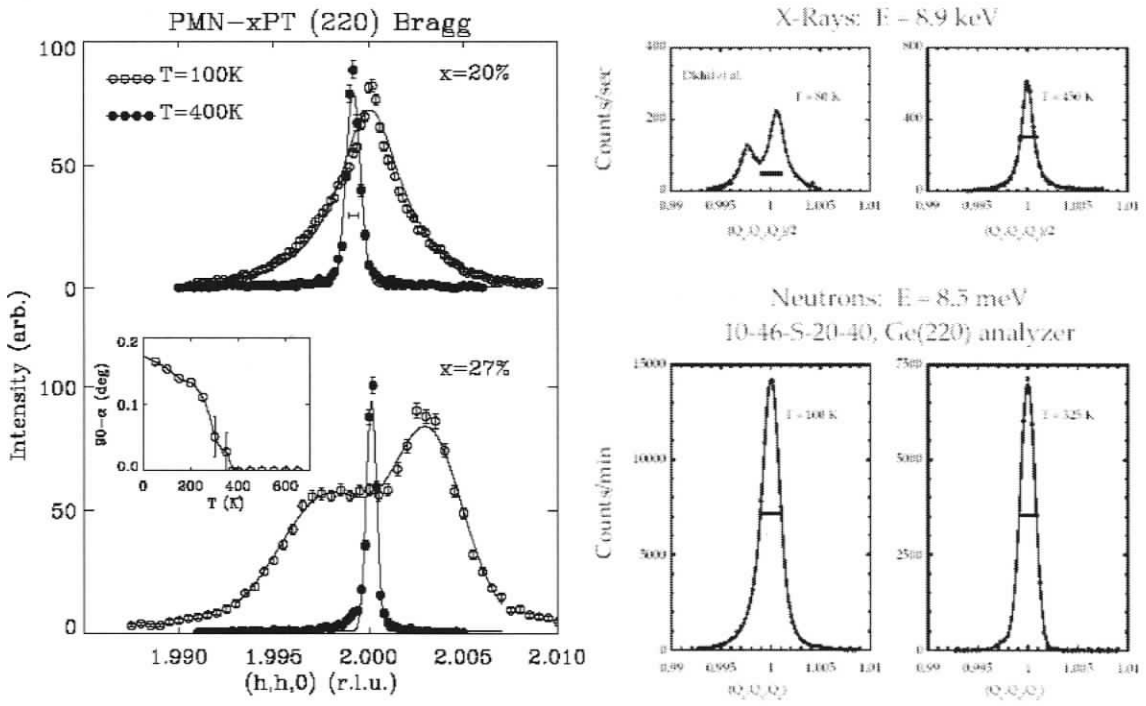

Figure 2-42 A) Diffraction peaks by Xu et al. [34] and B) Gehring et al. [86]

rhombohedral splitting of 222 diffraction peak at 80 K, shown in the upper section Figure 2-42B. Gehring et al. [86] examining single crystals of the same composition by neutron diffraction, obtained a broadened 111 diffraction peak, but with no splitting, at the closely similar temperature of 100 K, as shown by the diffraction profiles in the lower section of the figure.

A similar result was obtained by Xu et al. [34], for the 220 neutron diffraction pattern of a single crystal of composition PMN-0.2PT at 100K, as shown by the diffraction profiles in Figure 2-42A. The profiles in Figure 2-42A also show that rhombohedral splitting of the 220 peak at 100 K did occur in a single crystal of the higher PT composition of 0.27 mole fraction, which is in conformity with the previous results of Noblanc et al [68], and the field-free cooling results of Bai et al. [84] and Cao et al. [85], for single crystals of composition PMN-0.3PT. Gehring et al. [86] and Xu et al. [34] both claim to have identified a new phase "X", in which a rhombohedral distortion is confined within a cubic lattice. This rhombohedral confinement is postulated to break down with increasing PT concentration, so that a global rhombohedral phase is observed at low temperatures in PMN-0.27PT. In fact, the cubic phase they postulate is the same as the pseudocubic phase that is observed at temperatures down to 5 K in pure PMN [76].

Based on a finding in the closely related relaxor PZN-0.1PT [87], Gehring et al. [86] and Xu et al. [34] reconcile the differences observed between the powder X-ray data and the single neutron data, by suggesting that a ~50 μm outer layer of the single crystal of PMN-0.1 PT undergoes a rhombohedral distortion at low temperatures, while the interior

volume of the crystal retains the "X" cubic structure. The lower energy X-rays only penetrate to a depth of ~10 μm and will thus detect the rhombohedral structure, while the higher energy neutrons will pass through the narrow rhombohedral layer and diffract from the internal cubic volume. Similarly, neutron diffraction experiments on fine powder specimens will give only the rhombohedral structure. While this explanation for the observed differences between the X-ray powder results and neutron single crystal results is unquestioned, it should be noticed that these authors do not give any rationale as to why the rhombohedral phase only forms in a thin surface layer of the single crystal.

One possibility for the narrow rhombohedral region is a possible loss of a chemical constituent at the surface. The most likely candidate would be PbO [72, 73] but, as this would increase the proportion of both Ti and (Mg+Nb), it would be unlikely to move the PT composition into the rhombohedral region. An alternative explanation, which would be effective regardless of any constituent loss at the surface, is that the decomposition of the phase "X" at low temperatures is prevented by pressure constraints, generated by the elastic strains created by the rhombohedral distortions that are confined within it, as shown in Figure 2-25. Gehring et al. [86] and Xu et al. [34] have both drawn attention to these strains, by pointing out that the cubic profiles recorded at 80-100 K are significantly broader than those recorded at 400 K (Figure 2-42 A & B). This situation is analogous to the inability of partially stabilized zirconia to transform to the stable low temperature monoclinic phase, when it is embedded in zirconia toughened alumina, because the required increase in volume is prevented by the constraint of the surrounding alumina matrix [7]. However, if a free surface is opened up within the constraining alumina

volume, e.g. by the penetration of a crack, the constraint is released and the transformation takes place spontaneously and, incidentally, provides a mechanism for arresting the growth of the crack. On this basis, it is reasonable to infer that the cubic - rhombohedral transformation in the cubic phase "X" is inhibited by the pressure imposed on the rhombohedral volumes that are constrained within the single crystals, but the transformation can still occur in a thin 15 μm layer at the unconstrained surfaces of the single crystals, and throughout the unconstrained thickness of the 1 – 10 μm powder specimens. In the present context of a composition – temperature equilibrium diagram, the constrained cubic phase "X" should be properly regarded as a metastable (i.e. pressure stabilized) structure, while the rhombohedral phase that forms at the free surfaces should be regarded as the true low temperature equilibrium phase. This conclusion has an interesting consequence, because, on the basis of their research, Gehring et al. [86] have proposed a "universal phase diagram" for relaxor systems such as PMN-PT and PZN-PT, in which the constrained cubic "X" phase is considered to be the low temperature equilibrium phase!

In view of the importance of this relaxor ceramic system for engineering applications, it was decided to investigate the many contradictions in the published phase diagrams for the PMN-PT ceramic system, by examining the phase transformations in industrially prepared ceramics, using *in situ* high temperature X-ray diffractometry.

2.3. Fracture and Fatigue

2.3.1. Fracture of Brittle Materials

Cracks in Engineering components can be characterized as either external or internal, as illustrated in Figure 2-43. Both types of crack reduce the cross-sectional area available to support the load, so that the stress in the vicinity of the crack tip is greater than the average stress supported by the component. The concentrated stress σ_{tip} at the crack tip is given by the relationship [88]:

$$\sigma_{tip} = 2\sigma\sqrt{\frac{c}{\rho}} \qquad \text{Equation 2-48}$$

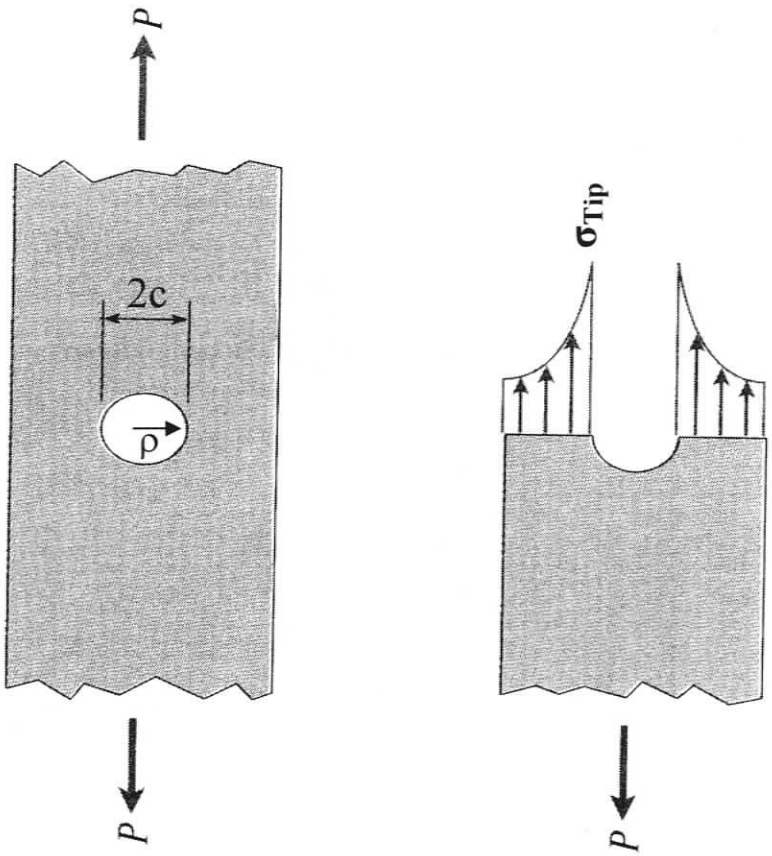

Figure 2-43 Internal crack showing stress concentrations at crack tip [89]

where 'c' is the length of an external crack (or half the length on an internal crack), 'ρ' is the radius of the crack tip and 'σ_{avg}' is the average stress supported by the component.

The three modes of loading that can contribute to crack growth are shown in Figure 2-44. In mode I, the crack is subjected to a force normal to the direction of propagation, while in modes II and III the crack is subjected to shear or torsional forces, respectively. The

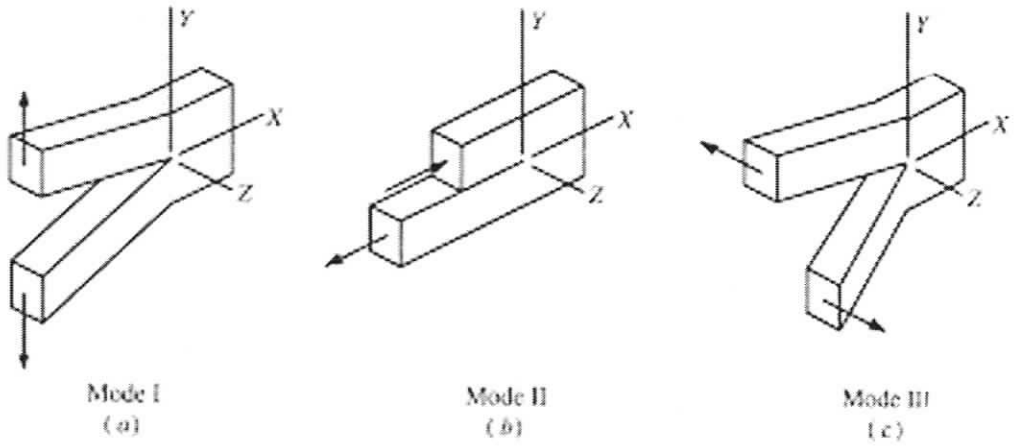

Figure 2-44 Cracking modes [7]

mode I condition is applicable to the experimentation in this thesis, where a low cycle electric field is applied normal to pre-existing cracks in piezoelectric and electrostrictive ceramics.

The factors governing the propagation of cracks in brittle materials were studied by Griffith [90] who developed the following equation for the critical stress σ_c at which an elliptical crack of length 2c will grow spontaneously:

$$\sigma_C = \sqrt{\frac{2E\gamma}{(\pi c)}} = \frac{K_{IC}}{(\pi c)^{1/2}} \qquad \text{Equation 2-49}$$

where E is Young's modulus of the material and γ is the energy associated with the creation of the new surfaces of the crack (by breaking inter-atomic bonds). The term 2γ is referred to as the crack resistance, R, and the term $[2E\gamma]^{1/2}$ (or $\sigma_c[\pi c]^{1/2}$) is referred to as the fracture toughness, which is given the symbol K_{IC}, where "I" refers to mode I in Figure 2-44. The parameters R and K_{IC} are both material properties.

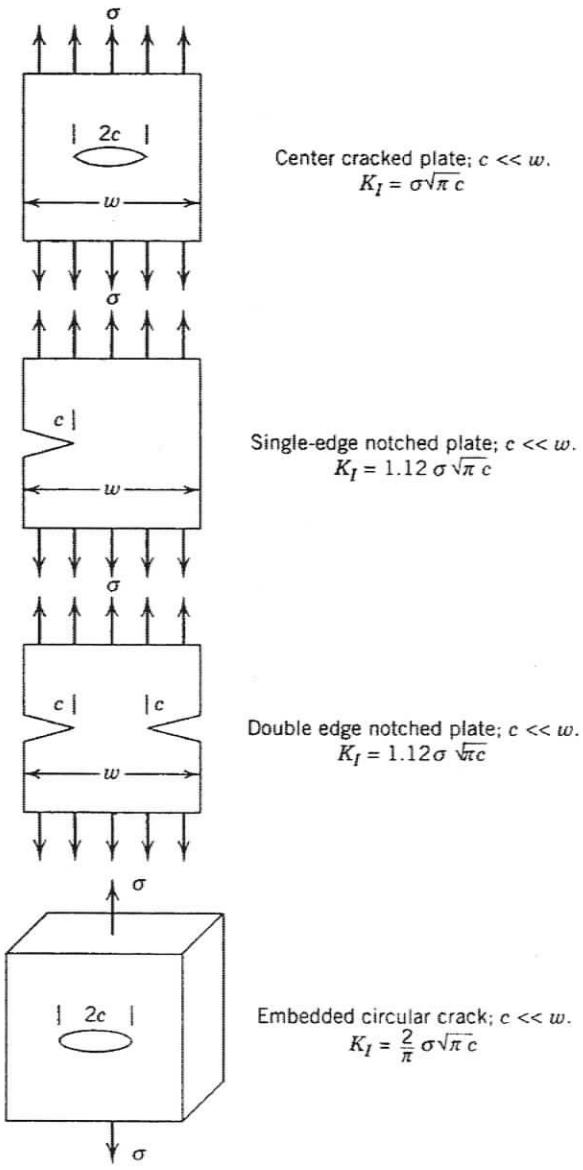

Figure 2-45 Mode I cracking for various geometries [7]

Using the relationship of equation 2-49, K_{IC} can be measured experimentally, by determining the critical stress σ_c at which a pre-existing crack of known size will propagate. This fracture toughness value is referred to as the critical stress intensity factor since, once this stress intensity is exceeded (either by increasing an applied load, or by increasing the length of a crack), the crack will propagate spontaneously through the thickness of the component. Stress intensity factors, calculated from the geometry of a crack subjected to Mode I loading, are illustrated by the examples in Figure 2-45. Ductile metals do not follow the Griffith criterion for crack growth, because some of the

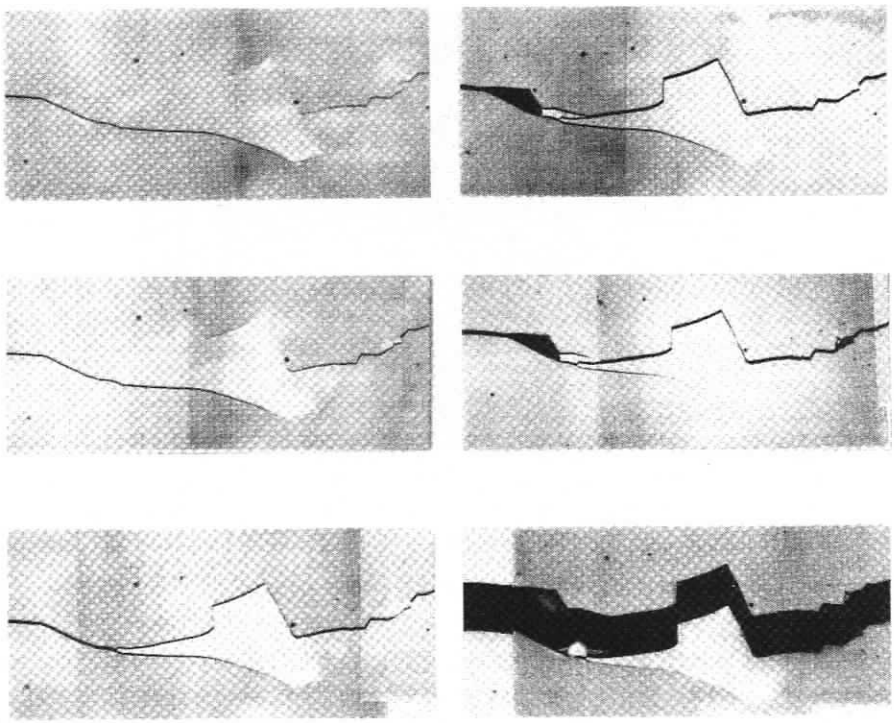

Figure 2-46 Crack bridging by a grain in coarse-grained alumina [7]

energy from an incident load causes plastic deformation, which blunts the crack tip and thus reduces the concentrated stress σ_c. Orowan [91] thus proposed that the Griffith equation should be extended by adding an effective surface energy term (γ_P) related to the work required to blunt the tip of a crack in ductile materials, i.e.:

$$\sigma_C = \sqrt{\frac{2E(\gamma + \gamma_P)}{(\pi c)}} = \frac{K_{IC}}{(\pi c)^{1/2}} \qquad \text{Equation 2-50}$$

The term γ_P is zero in homogeneous brittle materials, such as glass, so that once the critical stress is exceeded, fracture occurs spontaneously across the thickness of the component. In many ceramics, however, the propagation of a crack can be arrested by obstacles that impede its progress, so that an increase in stress is required for further

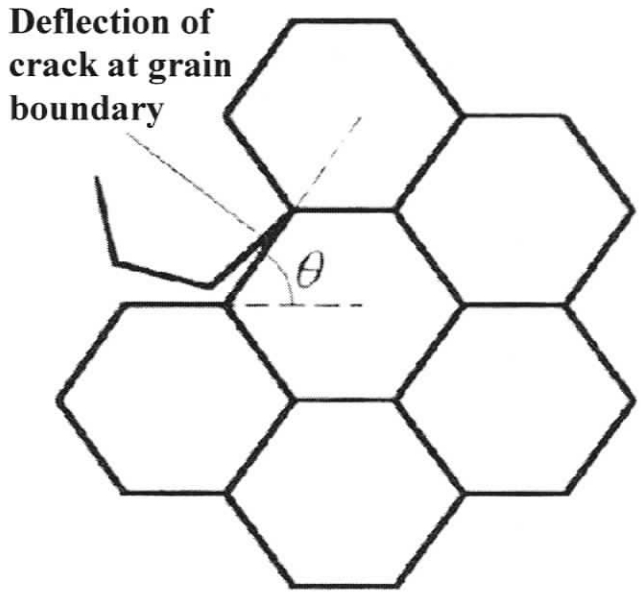

Figure 2-47 Schematic of crack deflection at grain boundaries [88]

crack growth. This situation can be expressed by introducing an additional effective surface energy term similar to γ_P in equation 2-50. The effect of this term is to increase both the fracture resistance, R, and the fracture toughness K_{IC}.

The form of obstacles that impede crack growth include agglomerates, particles, grain boundaries and microcracks, while short and long fibres in ceramic matrix composites slow down crack growth by crack bridging [7]. Crack impedance by bifurcation is illustrated in Figure 2-46, while crack deflection due to grain boundaries and microcracks is shown in Figures 2-47 and 2-48. Crack growth in a brittle matrix such as alumina can also be impeded by constrained particles of a metastable phase such as partly stabilized zirconia. The free surface created by a crack passing through these particles enables them to transform to a more stable structure, with a resultant 12% increase in volume, which

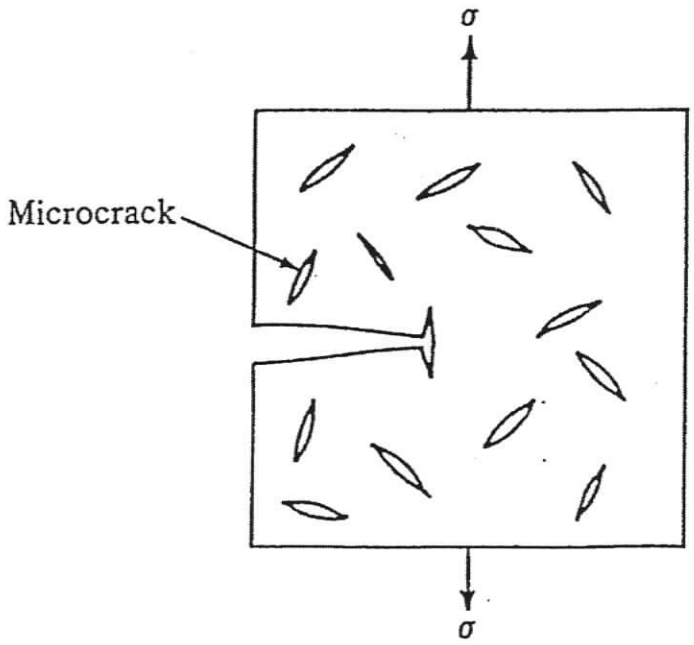

Figure 2-48 Crack propagation stopped by microcrack

sets up an elastic stress that opposes further crack propagation, as illustrated in Figure 2-49.

The stress-strain curve for a toughened ceramic is shown in Figure 2-50. A brittle material will fail at the fracture stress at the point X. In a toughened ceramic there is a

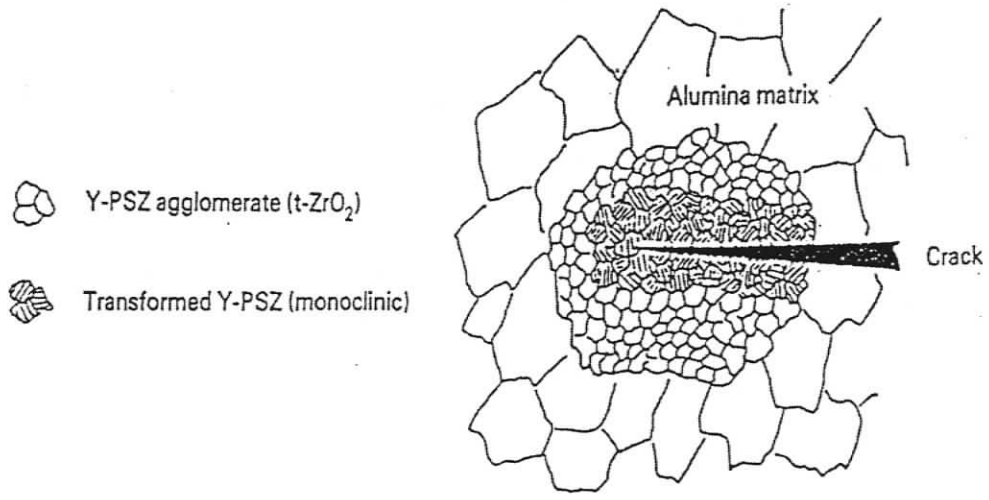

Figure 2-49 Zirconium Transformed Alumina (ZTA)

change in slope in the elastic region, caused by microcracking. At the critical stress for crack propagation, the toughened sample does not fracture catastrophically, but the critical crack increases in discrete steps as successive obstacles are overcome. The modulus of toughness of the ceramic, which is indicated by the area under the stress-strain curve, is thus progressively increased and the gradual failure occurs over a significant degree of strain.

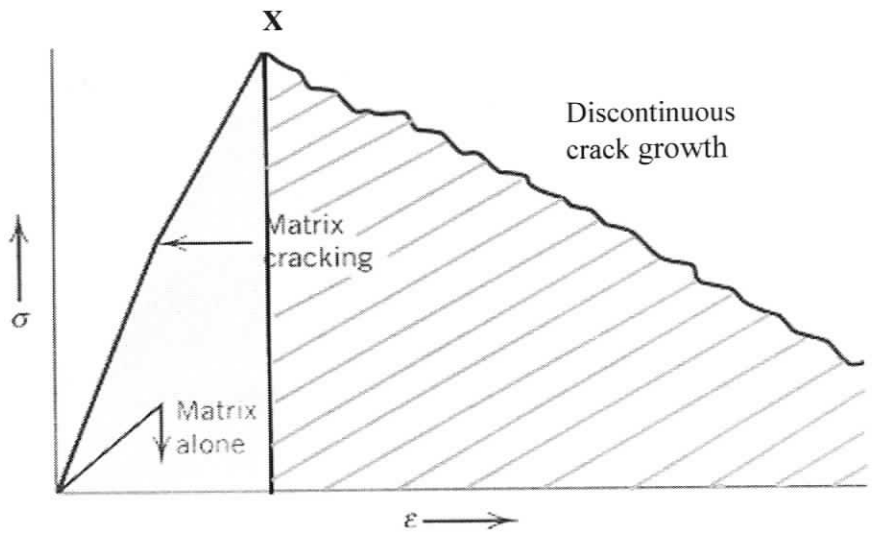

Figure 2-50 Schematic stress-strain curve showing added toughness [7]

The difference between the behaviour of brittle and toughened ceramics is also illustrated by the effect of flaw size on the fracture toughness parameter K_{IC}. As shown in Figure 2-51, a ceramic conforming to the Griffith relationship exhibits no increase in K_{IC} with increasing crack length, while the increase in K_{IC} observed in toughened ceramics is referred as "R curve behaviour". It is also shown that, in the absence of R curve behaviour the strength of the ceramic falls steeply and continuously with increasing crack size, while in toughened ceramics the decrease in strength is much smaller and maintains a relatively constant value over a wide range of crack extension.

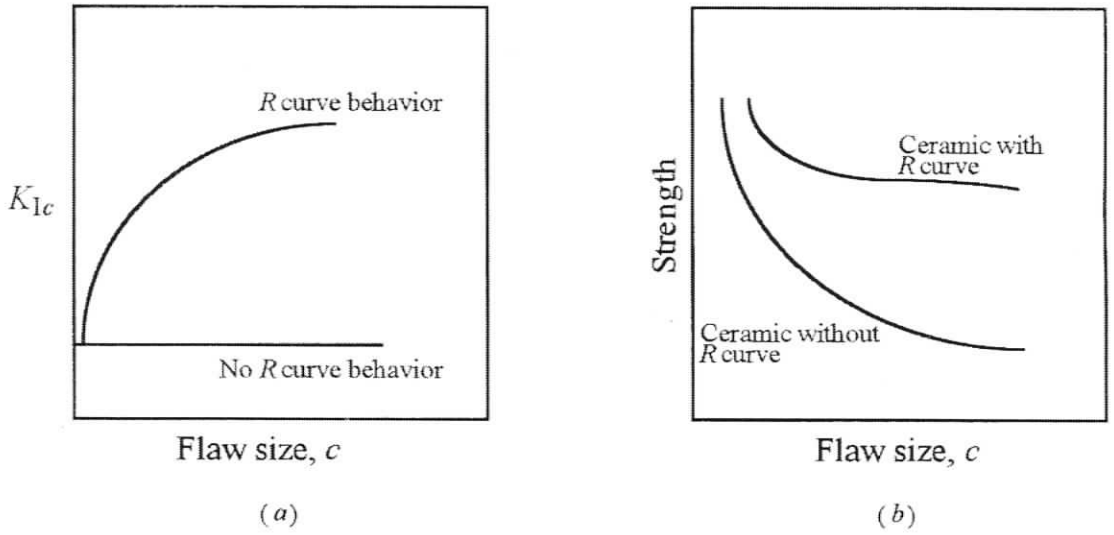

Figure 2-51 Effect of flaw size on R-curve behaviour [88]

2.3.2. Fatigue in ceramics

Fatigue is the tendency for a material to break under a repeated stress that is lower than the normal breaking stress. The repeated stress can take the form of cycles of tension-tension, compression-compression or tension-compression [88]. The mechanism of fatigue involves the progressive growth of cracks due to local stress concentrations. In this context, it is interesting to note that toughened ceramics that display significant R curve behaviour exhibit lower resistance to fatigue compared to brittle ceramics that show Griffith behaviour. If cracks in the latter are above the critical size, the component will fail on the first cycle, but no crack growth will occur in cracks below the critical size. In toughened ceramics, small cracks can grow progressively with repeated stress, which can lead to failure after a limited number of stress cycles.

Specimens used to measure fatigue are typically have either smooth crack-free surfaces or surfaces with cracks that are long in respect to the material structure [88]. The amplitude of the cyclic stress is defined by the following equation [88]:

$$\sigma_{amp} = \frac{\sigma_{\max} - \sigma_{\min}}{2} \qquad \text{Equation 2-51}$$

The load ratio is given as:

$$Load\ ratio = \frac{\sigma_{\max}}{\sigma_{\min}} \qquad \text{Equation 2-52}$$

The crack-free specimens are usually subjected to the cyclic stresses until failure. The data is then used to generate S/N curves where the stress amplitude is plotted against the number of cycles to failure. For specimens with long cracks, the crack growth rate per cycle (dc/dN) is measured as a function of ΔK_I, which is defined as follows [88]:

$$\Delta K_I = \xi (\sigma_{\max} - \sigma_{\min}) \sqrt{\pi c} \qquad \text{Equation 2-53}$$

where ξ is a geometric factor on the order of unity.

2.3.3. Electric Field Induced Fatigue in Piezoelectric and Electrostrictive Ceramics

The dielectric breakdown in capacitors has focused attention of the effect of electric fields on crack propagation in piezoelectric and relaxor ceramics. Early observations of the premature failure of these materials under the combined action of electrical and mechanical forces was first noticed by McHenry and Koepke [92], who attributed the observed crack growth to concentrations of electrostrictive forces in the region of flaws,

such as cracks and internal electrodes. By adding another term to the Griffith crack propagation model, the effect of applied fields on crack growth was later analyzed in terms of the total energy release rate [92, 93, 94, 96, 97]. Park and Sun [97] also pointed out that an electrostrictive model, which implies that the presence of an electric field of any sign would always impede crack propagation, is not appropriate for piezoelectrics where the observed strain is dependent on the sign of the applied field. These authors thus suggested that the mechanical energy release rate should be used, as this factor is affected by stresses ahead of the crack, caused by strains induced by local enhancements of the applied electric field. More detailed models based on the fracture mechanics of the non-linearity of stresses that build up in the region ahead of the crack have been suggested by Yang and Suo [98] and Zhu and Yang [99], but the situation in piezoelectrics remains confused because of contrary experimental observations.

Cao and Evans [101], for example, have reported a type of electrical fatigue in 58/42 PZT, whereby cracks emanating from the corners of a Vickers diamond hardness indent grow in a direction normal to applied low frequency cyclic electric fields, with peak to peak amplitudes less than the coercive field, E_C. These authors also report that extensive crack growth, at a rate independent of the crack length, occurs in cyclic fields with amplitudes greater than E_C. In contrast to these results, Lynch *et al.* [102] showed that pre-existing cracks in 8/65/35 PLZT grow rapidly to a length of the order of the separation of the electrodes, when subjected to fields greater than E_C. They also report that the crack growth observed in unipolar cyclic fields was significantly greater than the crack growth in bipolar fields, indicating that the negative component of a bipolar cyclic

field is ineffective for causing crack growth. Park and Sun [97] using Mode I compact tensile specimens report that positive electric fields (with respect to the direction of the polarizing field) tend to open cracks and thus lower the load to fracture, but Wang and Singh [102] using the Vickers indentation method report that cracks propagate less under a positive applied field, whereas crack propagation is enhanced in a negative applied field.

In a more recent paper Shieh et al. [104] report that the initial high rate of field induced crack growth, from a notched specimen of PZT, decreased with increasing number of electric cycles, to a point where growth is arrested. These authors focused their attention on the crack growth rate, as opposed to the limiting crack size at the arrest point. In PLZT, they report that no crack growth occurs in fields of $0.9E_C$ and $1.0E_C$, but crack growth does occur after initial incubation periods of $10^1 - 10^3$ cycles in fields of $1.2E_C$ and $1.5E_C$. After the incubation period, the field induced crack growth in PLZT passes through a steady state regime, before it is arrested after a defined number of electric field cycles. These results indicate that perhaps the contrary findings of Cao and Evans [101] arise because they did not run their experiments for a sufficient number of electric field cycles to achieve a limiting crack size. Using scanning electron microscopy, Shieh et al. [104] observed that a propagating crack in PZT is wedged apart by a narrow zone of intergranular cracks, while in PLZT a relatively broad band of microcracks is propagated normal to the direction of the applied field. They also observed that the crack growth rate (da/dN) in both ceramics increases qualitatively with the amplitude of the applied field and, after examining a number of possible correlating parameters, they obtained an

exponential correlation between the crack growth rate and the amplitude of the range of electrical displacement, which was obtained by dividing the peak to peak change in charge on the silvered surface of the specimen, by the area of the surface.

With the concentration of interest in piezoelectrics, the only significant research on the effect of electric fields on cracks in relaxor ferroelectrics has been performed by Raynes *et al.* [105]. Vickers diamond indentation cracks were generated in PMN ceramics, with a small but unspecified amount of PT, while the specimens were subjected to an applied electric field. The authors report that cracks were intergranular in nature and that cracks oriented perpendicular to the applied field were consistently shorter than similar cracks generated in the absence of an electric field.

In view of the importance of the PZT piezoelectrics, for transducer, sonar, sensor and hydrophone applications and of the PMN-PT relaxors, for actuator applications in smart structures, the study of crack growth Navy specifications of PZT and in selected compositions of PMN-PT has been included in the experimental research of this thesis.

3.0 Project Aim

3.1. Background

There is a reasonable body of literature concerning the initiation and growth of cracks in PZT ceramics under the action of applied electric fields, but similar studies have not been reported on PMN-PT actuators. Further, much of the work on the cyclic loading of PZT is contradictory, with authors claiming varying results. It is intended to repeat the work of these authors by performing similar experiments (i.e. by applying alternating fields on both static and dynamic mechanical loads). The experiments will be applied to PMN-PT ceramics for the first time to investigate their use in braking systems and to determine whether crack growth can be detected electronically. As the literature review has also revealed that there are many errors in the published structural phase diagram for the PMN-PT system, high temperature x-ray experiments will be conducted on a range of compositions to clarify the temperatures and structures of the structural transformations associated with their electromechanical properties.

3.2. Statement of Objectives

The objective of this work is two-fold:

> To characterize the electromechanical properties of commercial piezoelectric and electrostrictive ceramic actuators for potential use as actuators in electric braking systems.

To determine the location of the temperature/composition boundaries between the structural phases that occur in the ceramic system PMN-PT.

The objective with respect to electromechanical properties includes the following subsets:

i) Measurements of dielectric and piezoelectric properties for comparison with structural transformations observed in the same specimens of PZT and PMN-PT.

ii) Investigation of crack growth in cyclic electric fields in a range of PZT and PMN-PT compositions for possible correlation with known, or measured, piezoelectric or relaxor properties.

iii) Investigation of a possible non-destructive method for detecting the incidence and growth of field induced cracks with lengths below the level detectable by low magnification light microscopy.

The objective related to the structural transformations in PMN-PT can be divided into three subsections:

iv) Measurement of the temperature dependence of lattice parameters for a range of PMN-PT compositions, to determine the temperatures at which lattice stiffening occurs.

v) Investigation of changes in the shapes of selected Bragg profiles as specimens are cooled to identify the temperatures of the onset of structural transformations.

vi) Correlation of the temperatures of the onset of lattice softening, and the onset of structural phase transitions, with known temperatures of dielectric transitions, to develop a more realistic phase diagram for the PMN-PT ceramic system.

4.0 Experimental Methods

4.1. Types and Compositions of Ceramics

PZT ceramics based on selected US Navy specifications were prepared under industrial conditions at Sensor Technology Ltd., Collingwood, ON. The SensorTech designations for the Navy types selected for the present field induced crack growth experiments are given in Table 4-1. BM532, which conforms to Navy specification Type VI, was selected as a representative soft PZT piezoelectric and BM800, which conforms to Navy specification Type III, was selected as a representative hard PZT piezoelectric. An experimental hard piezoelectric BM200, which is under development at Sensor Technology, was also included in the field induced crack growth experiments. For convenience, the BM designations are used to identify the PZT piezoelectrics in the

Table 4-1 Designations of PZT Ceramics

SensorTech Designation	Navy Specification	Characteristics
BM532	Type VI	Doped with niobium pentoxide or lanthanum oxide to create soft piezoelectric properties
BM200 BM800	-- Type III	Doped with nickel, iron, or strontium oxides to induce hard piezoelectric properties

sections of this thesis that are concerned with Experimental Methods and Results and Conclusions.

PMN-PT ceramics have not as yet been formulated into military or industrial specifications, but individual companies have produced their own designations for a few compositions. The SensorTech designations for the ceramics used in the high temperature investigation of the phase diagram of the PMN-PT system are listed in Table 4-2. Since the BM designations are not correlated with the PT compositions, the PMN-PT ceramics are referred to by their PT mole fractions, i.e. the composition $[PMN]_{(1-x)}[PT]_x$ is referred to as: PMN-xPT.

Table 4-2 Designations of PMN−PT Ceramics

SensorTech Designation	PT Mole Fraction	Characteristics
BM600 BM620 BM610 BM640	0.00 0.08 0.10 0.20	These compositions are primarily relaxor ferroelectric at room temperature, but show increasing aspects of piezoelectric behaviour, with increasing PT content
BM660 BM680	0.30 0.35	These composition exhibit piezoelectric properties at room temperature

4.2. Preparation of Powder and Ceramic Specimens

Sensor Technology uses the direct synthesis technique [6] for manufacturing industrial powders and ceramics. As shown by the flow chart in Figure 4-1, appropriate weights of precursor powders of the oxides of lead, zirconium, titanium, magnesium and/or niobium, to give the required compositions of PZT, or PMN-PT, were ball milled to produce an intimately mixed powder with a particle size of ~1μm. The ball milled powder was agglomerated by spray drying, to obtain intimately mixed particles that were calcined by heating at 1110-1200 °C, to form the mixed oxide perovskite phase. To ensure that the PMN-PT samples were homogeneous and free of the unwanted pyrochlore phase, the

Powders	Ceramics
Weigh out raw oxide materials	Press powder to shape (uniaxial or hydrostatic)
Ball mill	Bisque
Spray dry	Sinter
Calcine	Grind or lap
Ball mill to desired particle size	Electrode (if required)
Spray dry	Polarize
Evaluate powder (repeat ball mill, calcine & spray dry)	Test properties (dielectric, piezoelectric and aging)

Figure 4-1 Sensor Tech process for manufacturing powders and ceramics

initial calcined product was crushed, milled and calcined a second time. The final calcined product was crushed and ball milled to a particle size of ~ 1 μm for use as x-ray powder specimens.

For ceramic specimens, the powder was spray dried with binder and lubricating additives and pressed into discs 10 – 20 mm diameter and 1 mm thick. The green disks were bisqued at ~300 °C, to remove the volatile organic binders and lubricants, and then sintered at 1100-1200 °C, to obtain the desired ceramics. The flat faces of the disks were ground or lapped to obtain smooth parallel surfaces, which were screen printed with Johnson Matthey epoxy silver paste, when electrodes were for required for polarizing, or for dielectric and electromechanical property measurements.

The purity of the powders was confirmed by the absence of second phases in X-ray diffraction patterns, while the macrostructural quality of the ceramics was assessed by comparing measured densities, derived by dividing the total weight of ten samples by the sum of their individual volumes, with theoretical densities derived from the parameters of the crystal structures. The microstructure of the ceramics was examined with a Zeiss polarizing light microscope at magnifications up to 1000X, and by scanning electron microscopy (SEM) using a Hitachi H-3500N. The distribution and homogeneity of the component elements were investigated using an EDAX energy dispersive X-ray analyser mounted on the scanning electron microscope.

4.2.1. Specimens for X-ray Examination

The spray dried calcined powder was used directly for some X-ray diffraction experiments. Solid specimens 19 mm x 12.5 mm x 1 mm thick were cut from uncoated sintered ceramic disks, using a diamond saw, for X-ray examination at non-ambient temperatures. The lapped 19 mm x 12.5 mm parallel faces of these specimens were exposed to the incident X-ray beam.

4.2.2. Specimens for Electromechanical Property Measurements

Uncoated sintered ceramic disks, or sections cut from larger disks, were used for density measurements. Silver coated disks, or sections cut from coated disks were used for measuring the temperature dependence of capacitance. Specimens 12.7 mm x 3 mm x 1.27 mm with silver coating on the 12.7 mm x 3 mm parallel faces were used for studying crack growth in incident cyclic electric fields. The narrow 12.7 mm x 1.27 mm faces of these specimens were polished with 600 and 2000 grit silicon carbide and then lapped with 6 μm diamond paste, to obtain a smooth flat surface for indentation with a Vickers, or Knoop, hardness tester diamond. For convenience, these specimens were also used for measurements of the field dependence of polarization and strain, and for measuring impedance to investigate vibrational spectra.

4.3. X-ray Diffraction Measurements

4.3.1. X-ray Diffraction Equipment

X-ray diffraction experiments were performed on a Scintag XDS 2000 theta-theta X-ray diffractometer equipped with a copper X-ray tube ($\lambda_{CuK\alpha 1}$ = 1.54060 Å), which was operated at 44 kV and 40 mA. The diffracted beam was scanned with a high-resolution

Peltier-cooled drifted Si detector and a Buehler HDK 2.3 high temperature attachment was used for measurements between room temperature and 300°C, as illustrated in Figure 4-2. A roll-a-round stand was constructed to support a new Haskris refrigeration unit, for cooling the X-ray tube, the Peltier detector and the walls of the Buehler high temperature chamber, as described in Appendix 8.1.1.

The specimen mount of the Buehler furnace was designed for powder specimens supported on a thin platinum or nichrome heater strip, the ends of which are wrapped around the water cooled posts for the electrical leads. This set-up creates a thermal gradient along the specimen, so that only the 10 mm centre section of the strip is at the

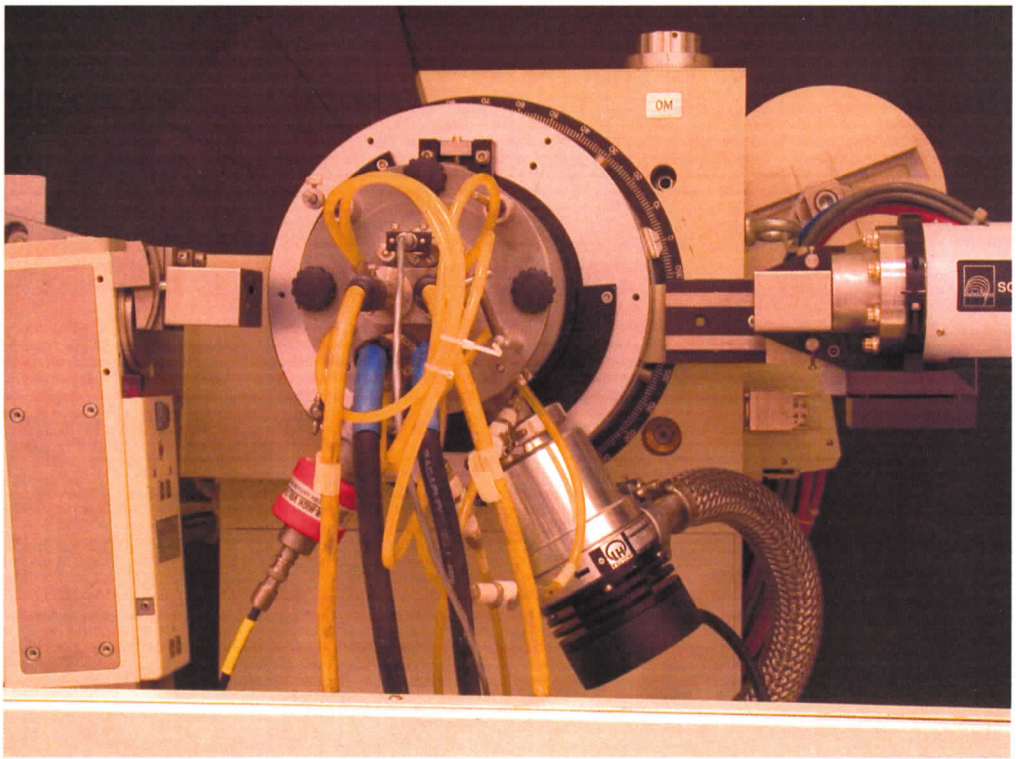

Figure 4-2 Scintag theta-theta X-ray diffractometer with Buehler high temperature chamber

temperature indicated by a thermocouple welded to the underside of the strip. When using thick powder specimens of insulator materials supported by the heater strip, the sample surface is significantly cooler than the indicated temperature [106] and this error is even greater when using solid ceramic specimens that do not conform exactly to the contour of the heater surface.

As the present experiments were not intended to go above 300 °C, it was decided to dispense with the heater strip and use only the surround heater of the Buehler furnace as the heat source. To eliminate temperature gradients along the irradiated length of the

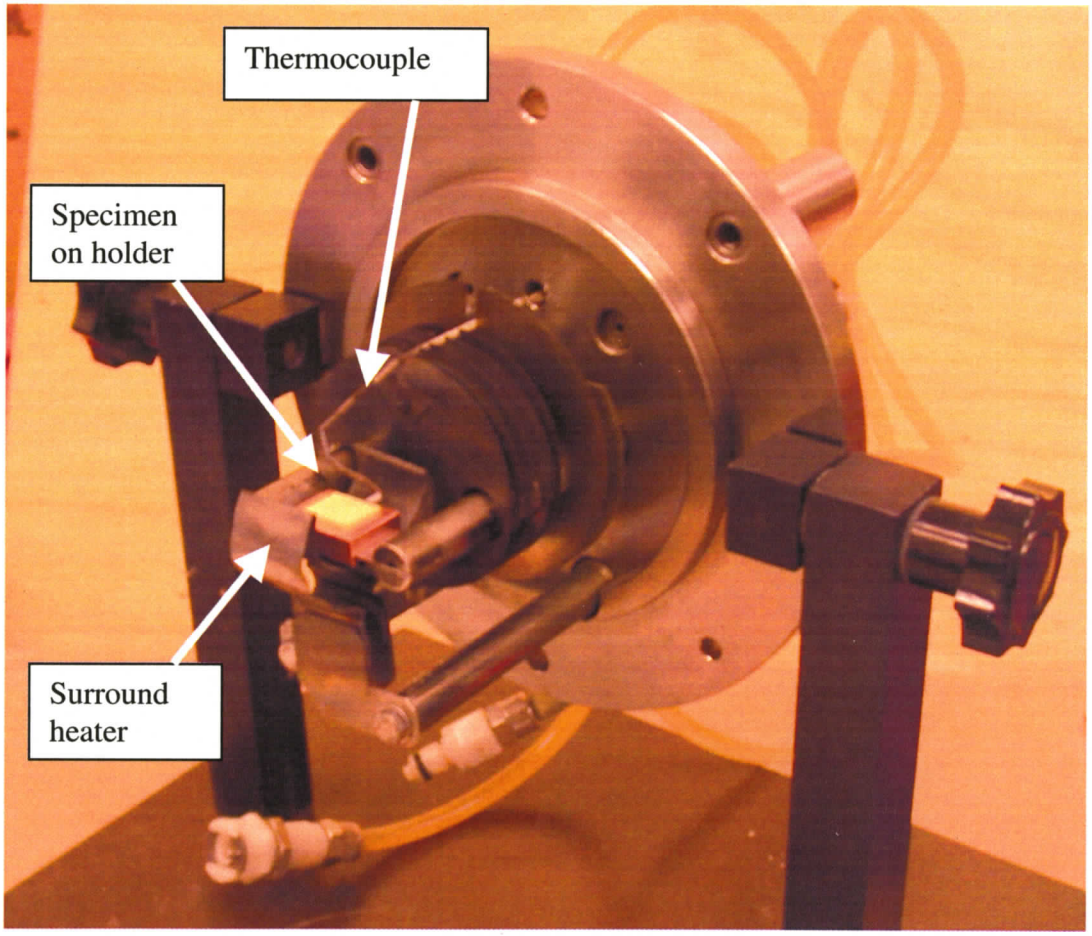

Figure 4-3 Specimen mount for high temperature X-ray diffraction

specimen, a new specimen mount was designed and constructed, as shown in Figure 4-3. The central section of 19 mm is composed of high thermal conductivity copper, to provide a uniform temperature along the irradiated length of the ceramic specimen, the temperature of which is measured by an attached Pt/Pt-13%Rh (type S) thermocouple. The ends of the specimen holder are attached to the cooling posts by stainless steel clips, which have significantly lower thermal conductivity than the copper support. One of the attachments of the specimen mount to the cooling tubes is in the form of a slide, to permit free thermal expansion. The top surface of the holder is machined to be flush with the top edge of the support tubes, which are directly coincident with the alignment path provided by the manufacturer's alignment device.

The rotational alignment of the specimen surface was adjusted by turning the furnace in its mounting bracket, until the offsets for the tube and the detector that permit an X-ray beam to pass through the device were less than 0.01°, as shown in Figure 4-4A. The vertical alignment was then achieved by raising, or lowering, the furnace until these offsets were equal and opposite as shown in Figure 4-4B. Tests showed that the temperature of a sample heated in air, by only the surround heater of the Buehler furnace, could be controlled to ± 1 °C with respect to a set point, when using the Micristar controller supplied with the Buehler furnace.

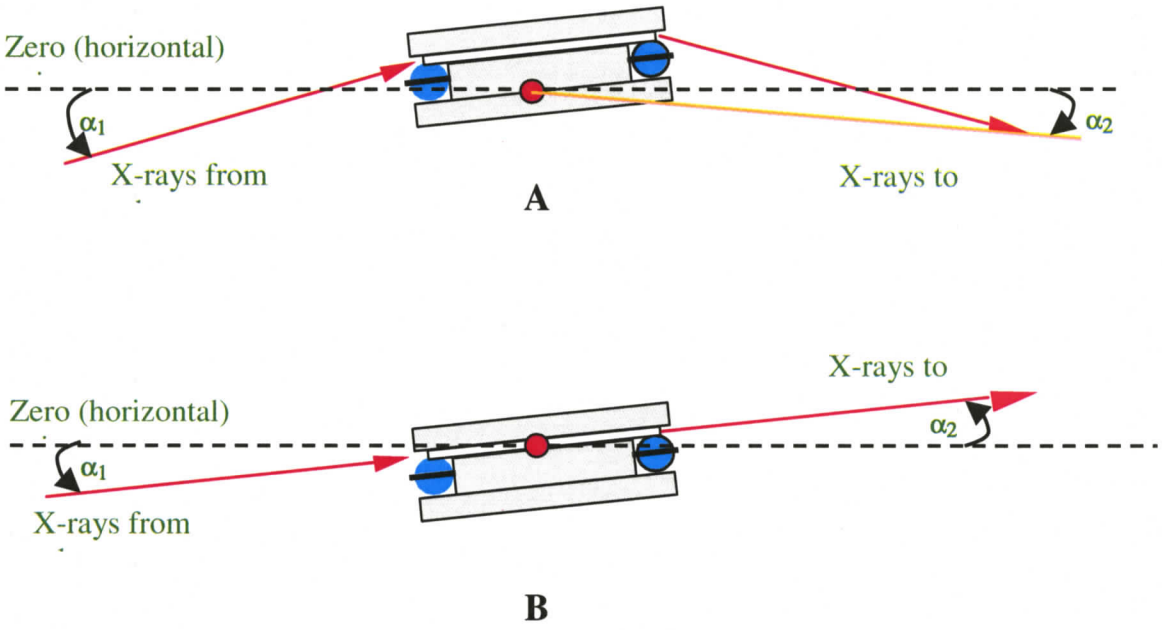

Figure 4-4 Alignment procedures for high temperature X-ray mount

For low temperature X-ray studies between 77 and 400 K, samples were cooled using a Joules-Thompson cold finger mounted on a flange plate fitted to the Buehler vacuum chamber, as illustrated in Figure 4-5. Temperatures down to 77K were obtained by expanding high-pressure nitrogen gas (1800 psi) through the fine passages in a glass sample holder and exhausting to atmosphere through a flow gauge and a roughing vacuum pump. The temperature was measured by a silicon diode and controlled to ± 0.1 K by offsetting the cryogenic cooling with a heater embedded in a gold plated copper block that supports the sample. A smear of vacuum grease was used to obtain good thermal contact between solid samples and the surface of the mounting block. A vacuum of at least 10^{-3} Torr was necessary to provide thermal insulation and to prevent condensation of water vapour on the cold sample surface.

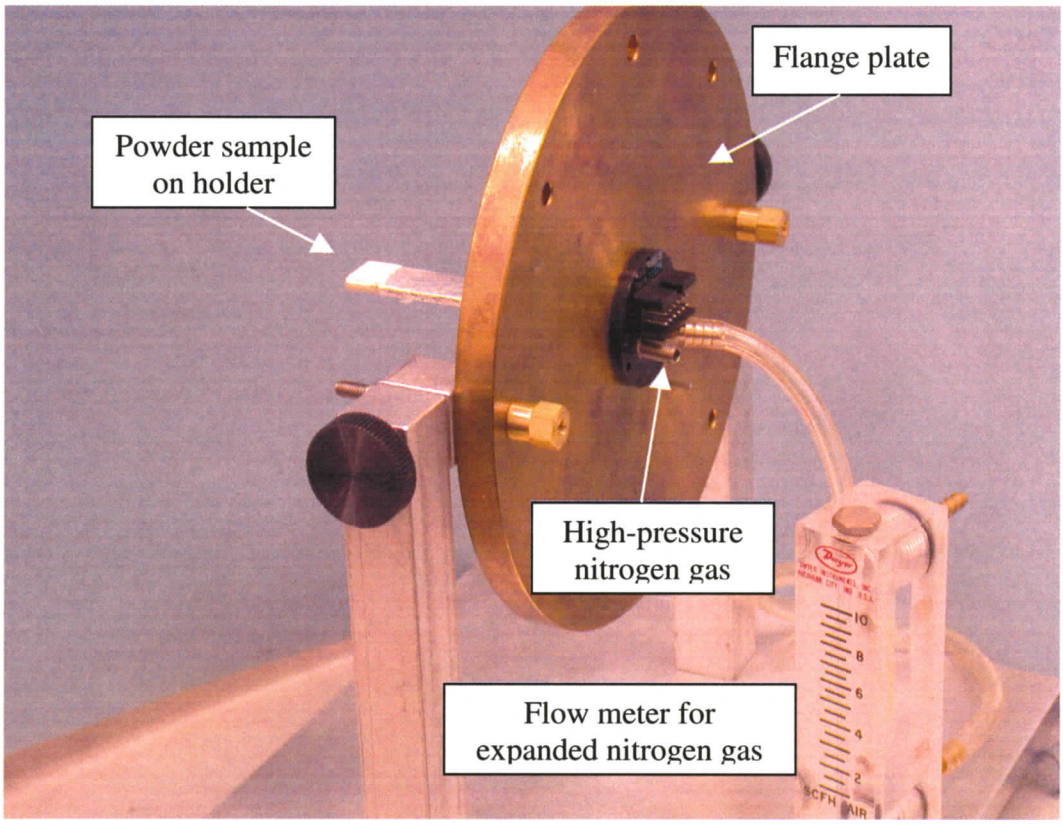

Figure 4-5 Cryogenically-cooled specimen holder mounted in flange plate

Previous users of this type of cold finger sample mount have recommend that it be aligned in the vertical direction by matching the Bragg angle peaks from the gold plating with angles derived from known values of the lattice parameter of gold [107]. However, as this technique does not allow for the thickness of a solid sample, which is of the order of 1 mm, the low temperature sample holder was aligned by adjusting the surface of a known specimen until the angular positions of its room temperature Bragg peaks agreed with those obtained when using the high temperature sample mount on a carefully aligned diffractometer.

4.3.2. Determination of Lattice Parameters

Lattice parameters, at both high and low temperatures, were calculated from the peak positions of diffraction profiles recorded at Bragg angles > 60 °2θ, as these are subject to minimum experimental errors [108]. However, certain high-angle Bragg peaks were excluded from the analyses, because their peak intensities could not be discerned with certainty, compared to the background radiation. Nevertheless, at least nine Bragg peaks per sample were measured for all lattice parameter determinations. To reduce the experimental time without loss of positional accuracy [108], these peaks were step-scanned using a step size of 0.06° and a dwell time of 2.5 seconds.

To ensure that the X-ray beam irradiated a significant length of the specimen, a divergence slit of 2 mm was used for Bragg angles from 50 to 100 °2θ and slit of 3 mm from 97 to 141 °2θ, while a receiving slit of 0.3 mm (equal to the projected width of the X-ray source), was used for all lattice parameter determinations. To eliminate angular dependent instrumental and measurement errors, the lattice parameters calculated from the positions of the measured Bragg peaks were plotted against the function $\cos\theta\cot\theta$ [108, 109]. The error bars for such a plot produce a triangular shaped plot (a cone in 3-D), where the error is reduced to zero at $\theta = 90°$ [108, 109]. Using the built-in functions available in Microsoft Excel, a linear trend line and its equation were applied to each plot. The lattice parameter at $\cos\theta\cot\theta = 0°$ (i.e. at $\theta = 90°$) was taken to be the intercept value in each equation. The accuracy of such lattice parameter determinations is estimated to be ±0.00005 Å [108].

4.3.3. Recording the Shapes of Diffraction Profiles

For structural identification, and for the investigation of phase transformations to structures of lower crystal symmetry by peak splitting, selected Bragg peaks over the range from 90 to 141 °2θ were step-scanned under conditions to enhance resolution, i.e. using a step size of 0.06°, with an extended dwell time of 20 seconds. A divergence slit of 3 mm was used, to ensure that the X-ray beam irradiated a significant length of the specimen, with a receiving slit of 0.3 mm to give high resolution. Selected Bragg peaks were successively scanned over the ranges of temperature at which phase transformations were expected to occur for specific ceramic compositions.

4.4. Electromechanical Measurements

4.4.1. Apparatus for Temperature Dependence of Capacitance

Preliminary measurements of the temperature dependence of the capacitance of selected PMN-PT ceramics were made at Sensor Technology, Ltd., Collingwood, ON, using a Hewlett-Packard HP4262A capacitance meter. This instrument was also used to measure the dissipation factor of the specimens. For a more complete study of the capacitance of the ceramics in the PMN-PT system, a new apparatus was designed and constructed, as illustrated in Figure 4-6. The parallel silver coated faces of the specimen are held in contact with the electrodes at a constant pressure by the mass of a 70 g copper bock. The shape of the specimens is not critical, provided the area of the coated faces is less than that of the electrode probes, in order to minimize end effects.

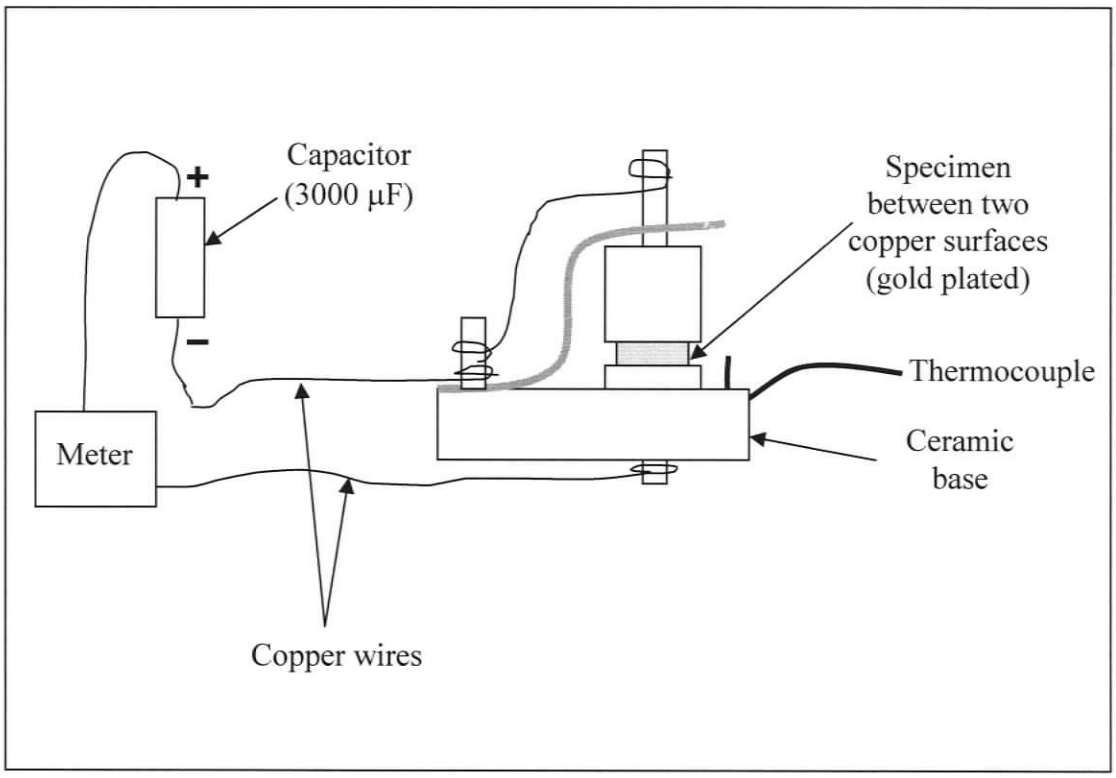

Figure 4-6 Schematic drawing of capacitance measurement apparatus

For measurements over the temperature range from room temperature to 300 °C, the apparatus was installed in a "Blue M Lab-Heat" (model # M25A-2A) muffler furnace, with an internal cavity 12 cm x 12 cm x 25 cm. To prevent oxidation of the electrical contact faces, and all other surfaces, the entire capacitance-measuring device was gold plated. The temperature of the specimen was measured by a chromel/alumel thermocouple, located adjacent to its surface, as indicated in the figure. A 3000 μF standard capacitor was placed in series in the measuring circuit, to enable the capacitance of the specimens to be measured to an accuracy of ± 0.001 μF, over the range from 0 to

3000μF, when using a Hewlett-Packard HP4262A capacitance meter. The capacitance measurement apparatus used for the dielectric measurements is shown in Figure 4-7.

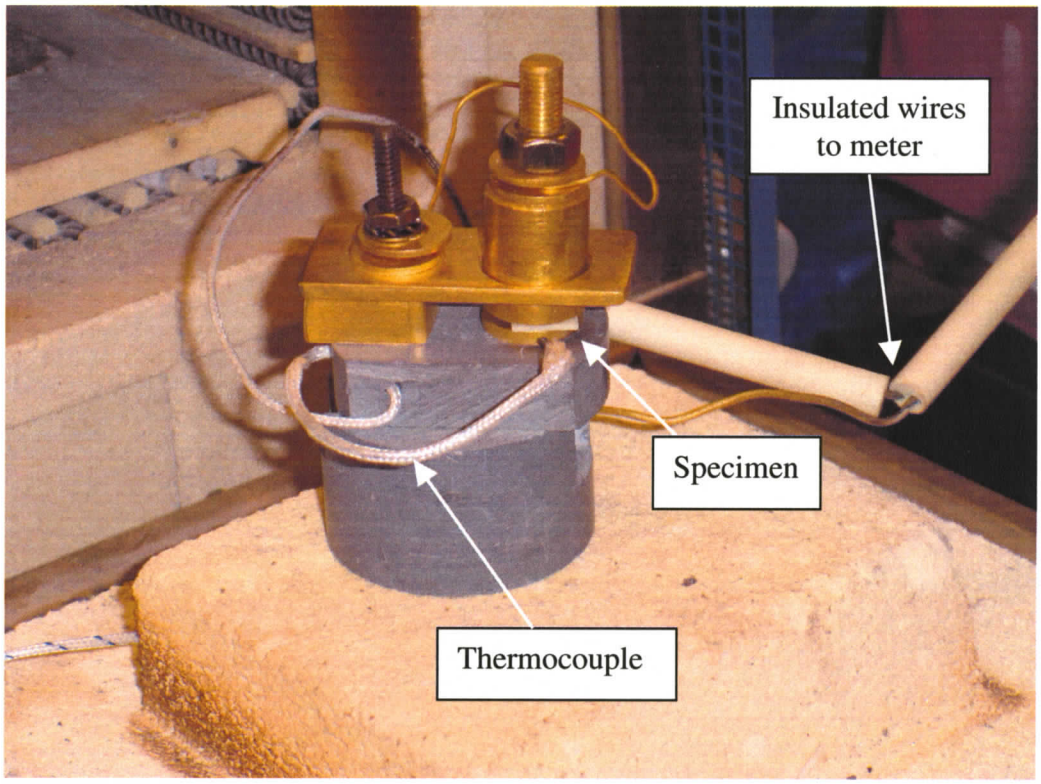

Figure 4-7 Capacitance measurement apparatus used for experiments

4.4.2. Field dependence of Polarization and Strain Measurements

Cyclic electric fields were produced by a Trek 609E-6 high voltage amplifier, with a maximum output of ±4 kV at ± 20 mA. The amplifier was incorporated into a combined electrical circuit with a common computer for the control and analysis of polarization and strain measurements, as shown in Figure 4-8.

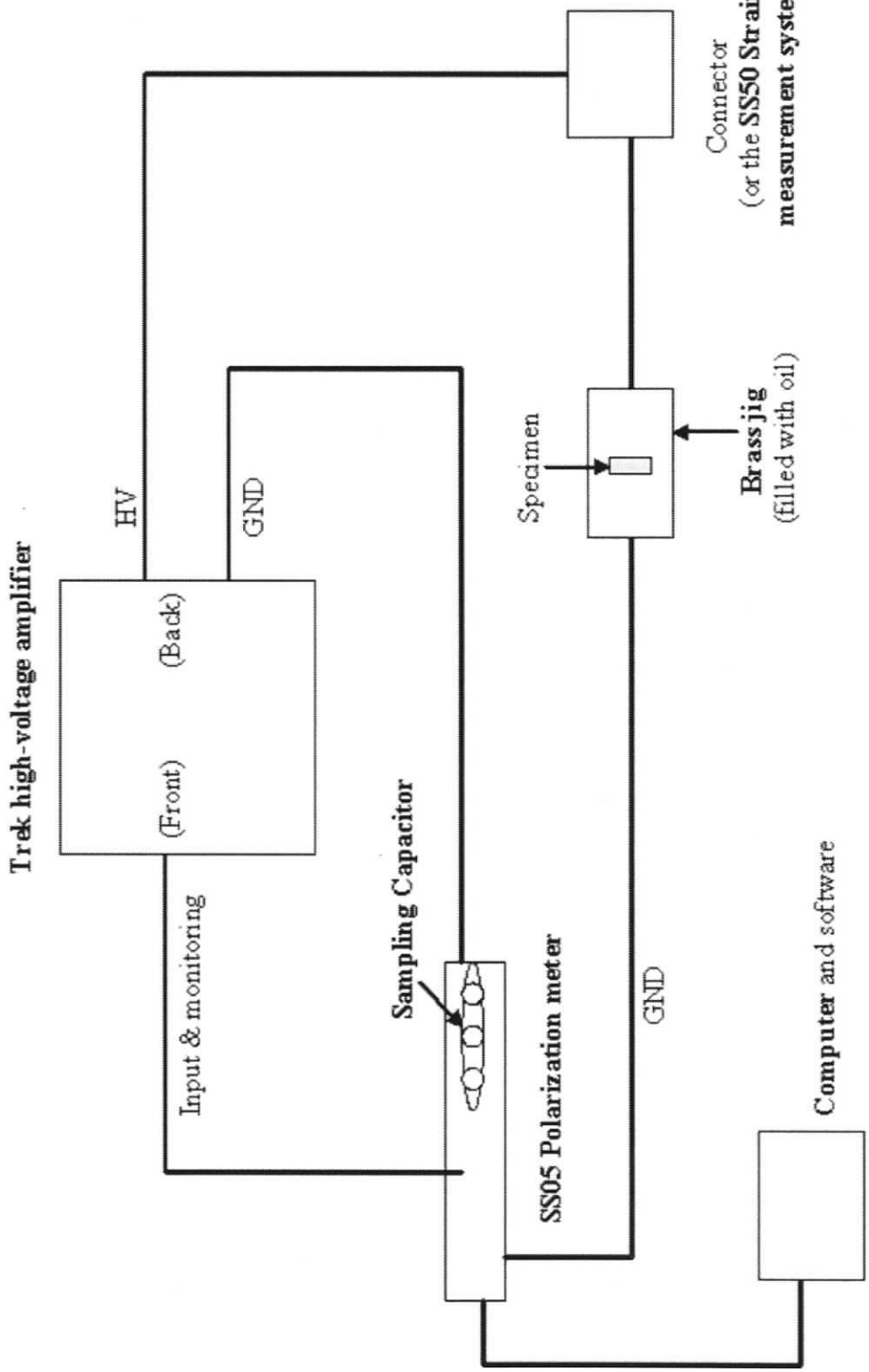

Figure 4-8 Apparatus for applying cyclic fields and for measuring polarization and strain

Polarization as a function of applied field was measured by a Sensor Tech SS05 polarization unit [110], which incorporates a low voltage sine wave generator with a frequency range of 0.001 – 10 Hz and interchangeable plug-in capacitors rated at 5 and 15 μF. The output from this device was fed to the control computer for analysis. The coercive fields and the saturation and remanent polarization of the samples were read off the polarization vs. field plots.

Strain versus field measurements were made with a Sensor Tech SS50 strain measurement unit [110]. This instrument incorporates an LVDT with a stroke of 1.3 mm, a non-linearity of ±0.25% and a sensitivity better than ± 200 mV/V/mm. The ±10 V output from the LVDT was also fed to the computer via a signal conditioner, which has an output sensitivity of 100 mV rms to 5.5 V rms (i.e. up to 10 V DC) with a ripple less than 10 mV rms.

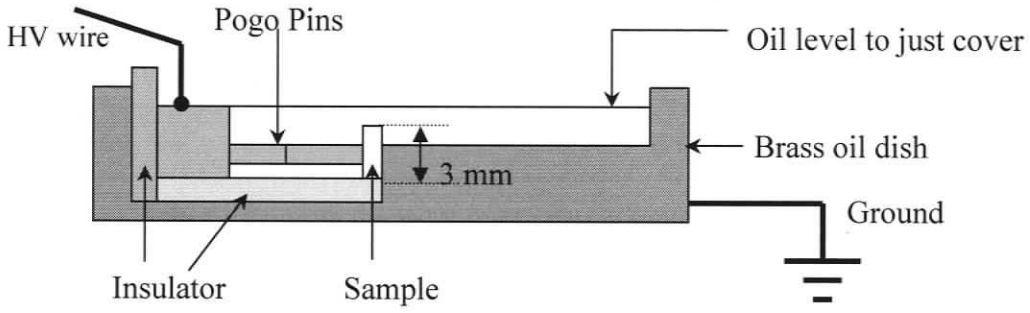

Figure 4-9 Specimen holder for physical property and crack growth measurements

The 12.7 mm x 3 mm x 1.27 mm specimens used for the polarization and strain measurements were mounted in the specimen holder shown in Figures 4-9 and 4-10. The specimens were rigidly clamped in position by two pogo pins, which act as electrodes for

applying electric fields to one of the 12.7 mm x 3 mm silvered surfaces. These pins also ensure that the opposite silvered face of the sample is maintained in good contact with an electrically grounded brass block, which forms the other electrode.

To prevent possible arcing when using applied fields in the vicinity of 3.15 MV/m, the sample and electrical probes were immersed in insulating oil. With the narrow specimen

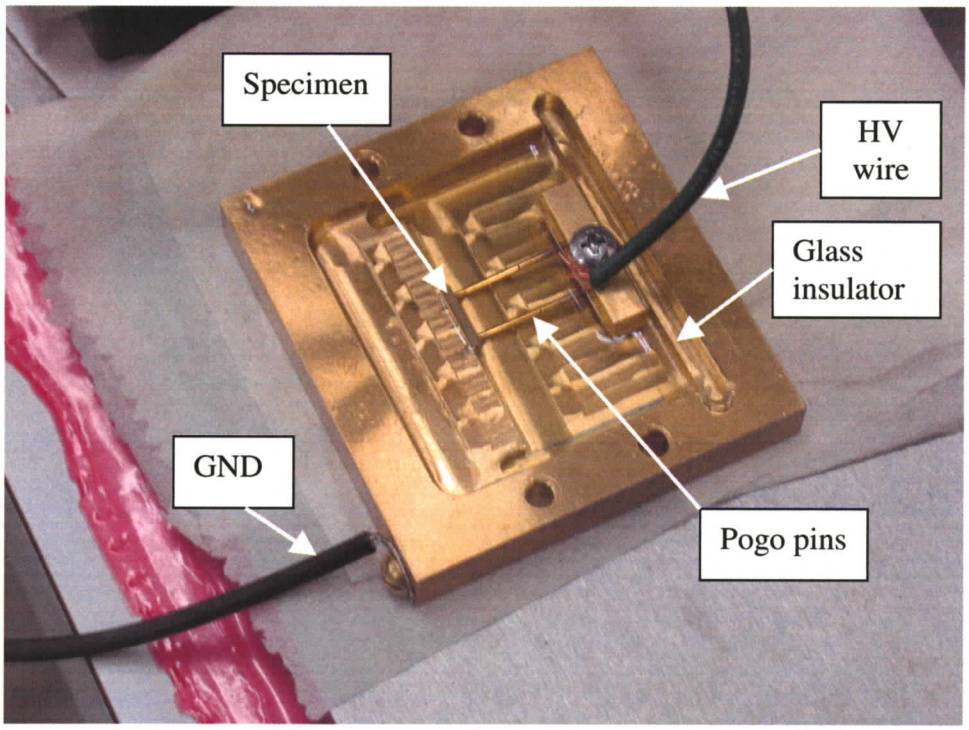

Figure 4-10 Brass specimen mount used for experiments

width of 1.27 mm between the silvered faces, the maximum field generated by a 4 kV output from the Trek is limited to 3.15 MV/m. The samples are thus not vulnerable to dielectric breakdown, which typically occurs in the range of 4-8 MV/m in PZT compositions [110].

4.4.3. Crack Growth Measurements in Cyclic Electric Fields

Cracks were initiated in the 12.7 mm x 3 mm x 1.27 mm ceramic specimens by imposing a Vickers hardness diamond indenter on one of the narrow (12.7 mm x 1.27 mm) polished faces for a period of 10 sec, under a load of 20 N. The samples were oriented in the hardness tester so that one set of the corners of the diamond indent was aligned parallel, and one set normal, to the silvered electrode faces, as shown in Figure 4-11. This orientation ensured that a set of cracks emanating from the corners of the indent would be parallel to the silvered electrode surfaces, i.e. normal to an applied cyclic electric field.

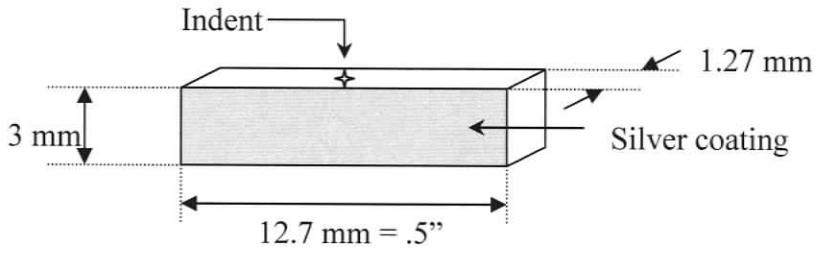

Figure 4-11 Specimens used for crack growth studies in cyclic fields

Similar indents made with a Knoop diamond applied at load of 20N for 10 sec, were oriented so that the acute angle corners of the indent, which are more likely to generate cracks, were aligned parallel to the silvered surfaces. The nature of the cracks, i.e. transgranular or intergranular, was investigated at a magnification up to 800X using a Zeiss photographic microscope, that was adapted for use with a Nikon 995 digital camera, as described in Appendix 8.1.2.

The indented specimens with pre-existing cracks were placed in the specimen holder shown in Figure 4-9, which in turn was mounted on the stage of Fisher Scientific Micromaster CK optical microscope, so that the cracks normal to the applied field were aligned parallel to the translation direction of the stage. When the specimen holder (on the microscope stage) was incorporated into the combined circuit shown previously in Figure 4-8, low cycle electric fields, with frequencies of 2 to 10 Hz, and amplitudes up to 4kV, were applied to the silvered faces of the specimens using the Trek 609E-6 high voltage amplifier. The length of a selected crack was measured, before and after the application of a predetermined number of field cycles, by translating the stage of the

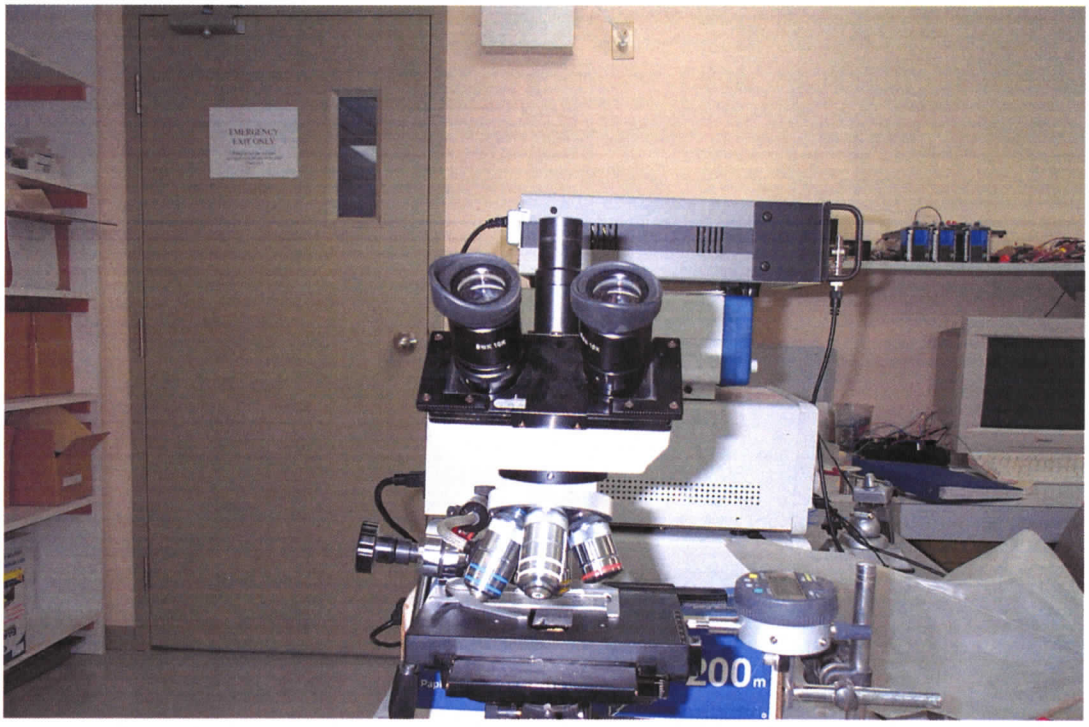

Figure 4-12 Apparatus for measuring crack lengths in ceramics

microscope so that a cross hair in the eyepiece traversed from one end of the crack to the other. The magnitude of this translation, which indicates the length of the crack, was measured with a Mitutoyo model ID-C112E displacement gage that was spring loaded

against one end of the microscope stage, as shown in Figure 4-12. The resolution of these crack length measurements was estimated to be ± 50 μm.

4.4.4. Resonant Frequency Measurements

The resonant frequencies of the 12.7 mm x 3 mm x 1.27 mm ceramic specimens in the pre-cracked condition, and after exposure to cyclic electric fields, were derived from

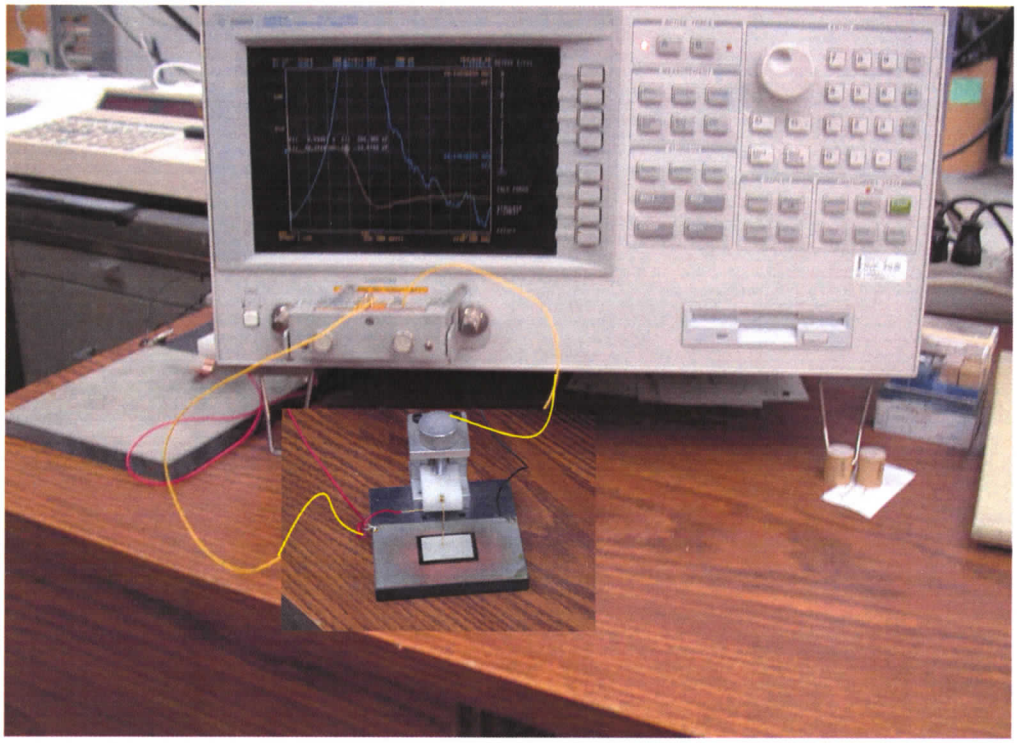

Figure 4-13 Agilent 4294A precision impedance analyzer with jig

impedance spectra measured with an Agilent 4294A precision impedance analyzer, using a constant voltage circuit of the type shown previously in Figure 2-15 in the Literature Review. The Agilent 4294A analyzer and in-house jig are shown in Figure 4-13. The length thickness extensional (LTE) resonance mode was used for these measurements, as it is the lowest frequency resonance dictated by the geometry of the specimens, which were silver coated on the parallel 12.7 mm x 3 mm faces.

5.0 Results and Discussion

5.1. Characterization of Powders and Ceramics

5.1.1. Purity and Particle Size of Powders

The room temperature X-ray diffraction patterns obtained for five ceramic specimens of PMN-PT are given in Figure 5-1. All compositions show Bragg peaks that can be indexed according to the cubic perovskite crystal structure. At Bragg angles less than 90 °2θ, the profiles are broadened so that the $K_{\alpha 1}$ and $K_{\alpha 2}$ peaks cannot be resolved. This broadening is caused by the deformation of the cubic perovskite structure into rhombohedral or tetragonal structures due to small shifts of the Nb and Mg ions along [111] or [100] directions from their body-centred positions in the unit cell [46]. As the magnitude of these ion displacements is not large enough to cause the Bragg profiles to split into the component hkl peaks of the deformed structures, the broadened peaks in all of the diffraction patterns can be indexed as pseudocubic perovskite structures.

The almost complete absence of the maximum intensity diffraction peak of the $Pb_2Nb_2O_7$ pyrochlore structure at 29 °2θ, confirms that the ceramic samples prepared by the Sensor Technology process are effectively free from this unwanted phase. The absence of diffraction peaks of the lead titanate (PT) structure also confirms that the PT component is in complete solid solution in the lead magnesium niobate (PMN) perovskite crystal structure; while the relative sharpness of the peaks in the diffraction pattern indicates that the particle size of the prepared powder is of the order of a few μm.

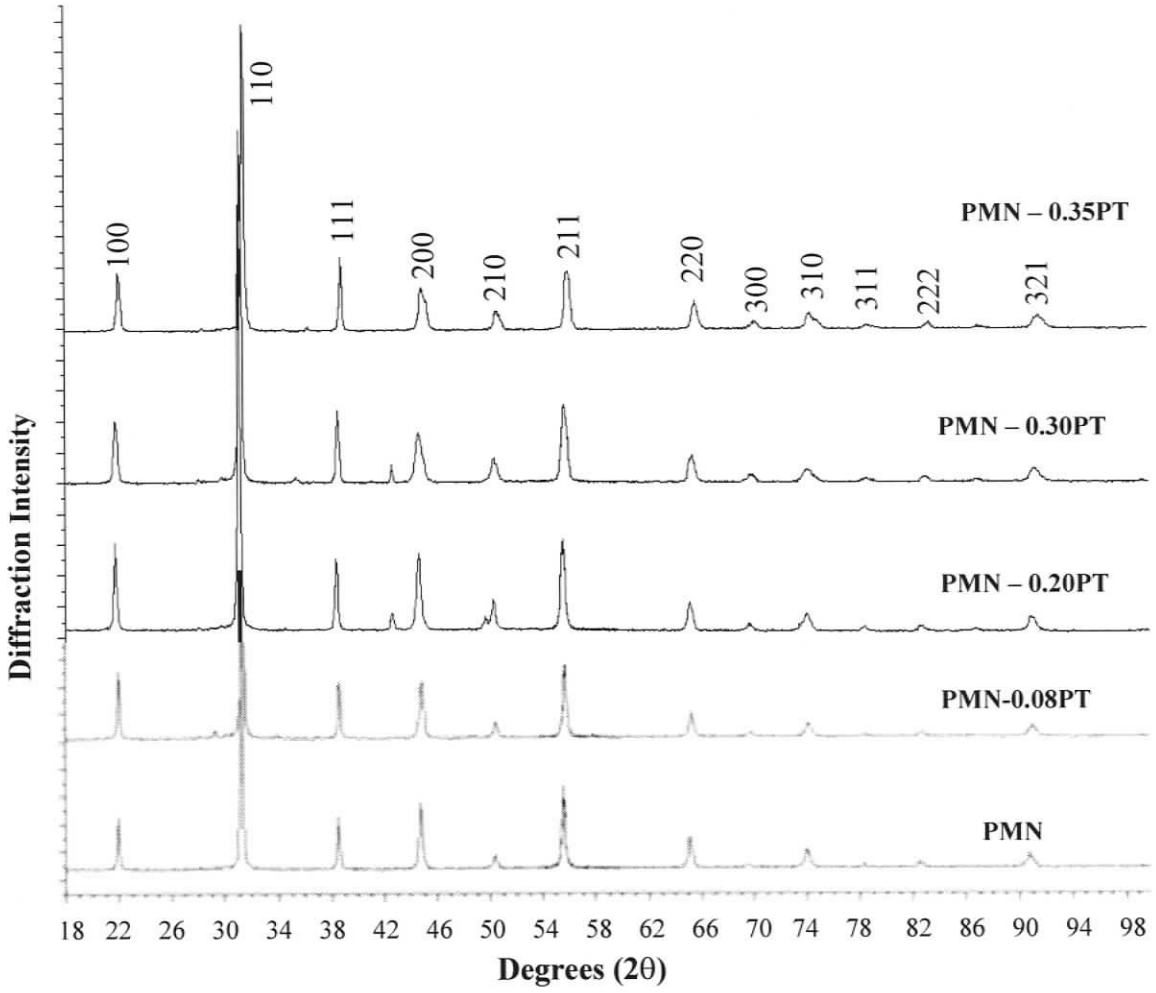

Figure 5-1 Low-angle X-ray diffraction patterns for PMN-PT ceramic specimens

5.1.2. Quality and Homogeneity of Ceramics

The densities of the PMN-0.08PT and PMN-0.3PT ceramics were found to be 7.77 g/cm^3 and 7.61 g/cm^3 respectively, based on measurements of the combined weight and volume of ten specimens. The 7.77 g/cm^3 is 99.6% of the Sensor Technology value of 7.8 g/cm^3 for BM600 (PMN-0.1PT). As these values are within 5% of the respective theoretical densities of 8.134 g/cm^3 and 8.023 g/cm^3, the pore densities of these sintered ceramics are considered to be less than 5%. This inference is confirmed by the SEM micrograph of the PMN-0.08PT ceramic in Figure 5-2, which is typical of all the ceramics examined, and shows no obvious pores in the field of view at high magnification.

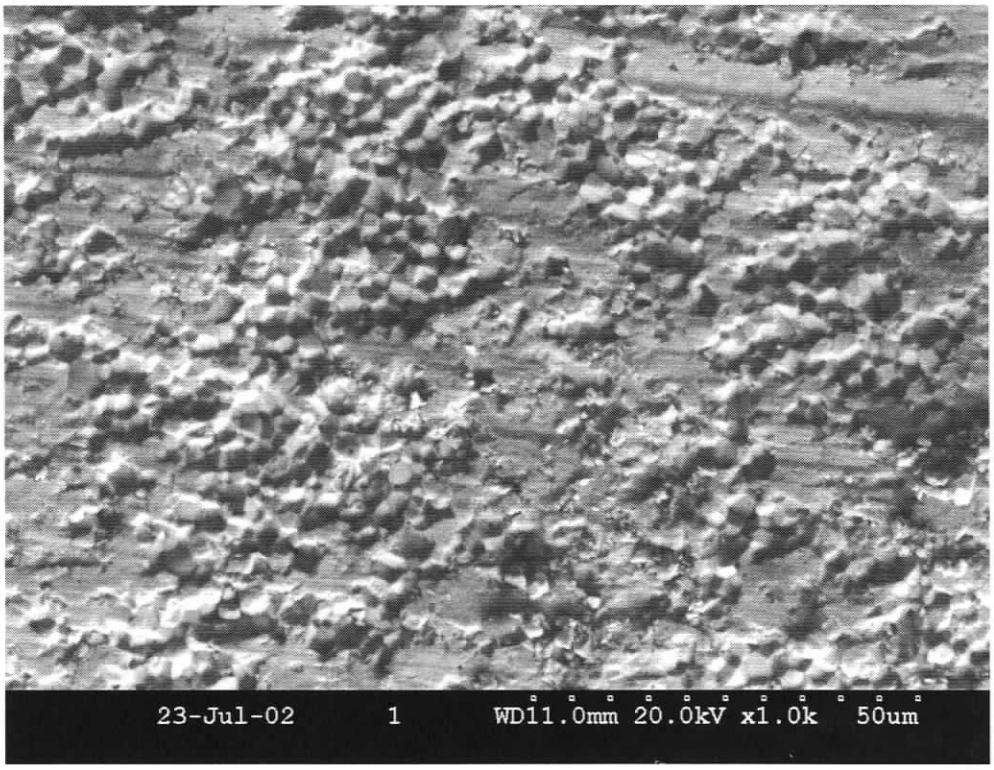

Figure 5-2 SEM micrograph of PMN-0.08PT ceramic

5.2. Physical and Electromechanical Property Measurements

The physical and electromechanical properties of PZT ceramics have been extensively studied over the past twenty years, so have not be re-measured unless specific information, such as coercive fields for particular formulations, is required to understand the new observations made on the effect of cyclic electric fields on the growth of pre-existing cracks. More measurements have been made on ceramics in the PMN-PT system, as these are relatively new materials, but once again the selected properties are directly relevant to understanding, or interpreting, observations made in other sections of the thesis, such as the nature of phase transformations in this ceramic system. Properties that have been measured include the temperature dependence of capacitance, the frequency dependence of impedance, and the field dependence of polarization and strain. With the exception of the asymmetry observed in the hysteresis loops of internally biased field hard piezoelectrics [112], the property measurements are discussed in the context of other observations to which they are relevant.

5.2.1. Temperature Dependence of Capacitance and Dissipation

In experiments conducted at the University of Victoria, the capacitance of the PMN-0.1PT sample was measured at decreasing temperatures over the range from 175 °C to -23 °C. As shown in Figure 5-3, the capacitance passes through a relatively broad maximum, typical of relaxor behaviour, at 41 ± 1°C, which is in close agreement with previously published values that lie between 38 °C and 40 °C [6, 33, 41, 113]. The

dissipation factor (tan δ) of this sample passed through a sharp maximum between 30 -31 °C, which is again in good agreement with previous values [6].

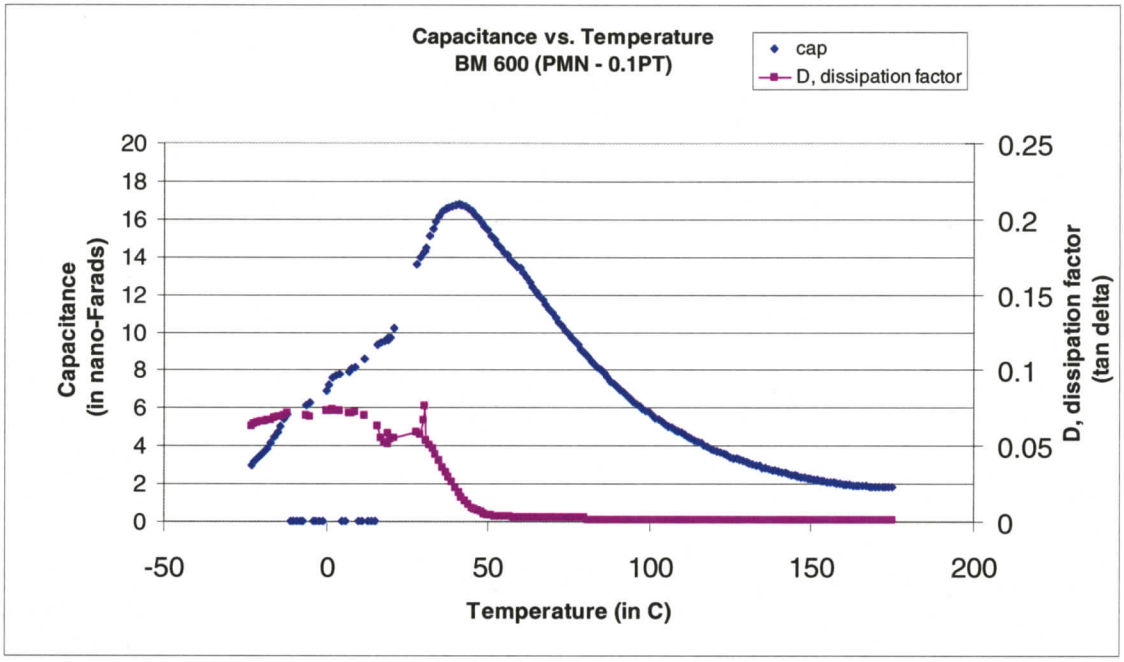

Figure 5-3 Capacitance vs. temperature for PMN-0.1PT

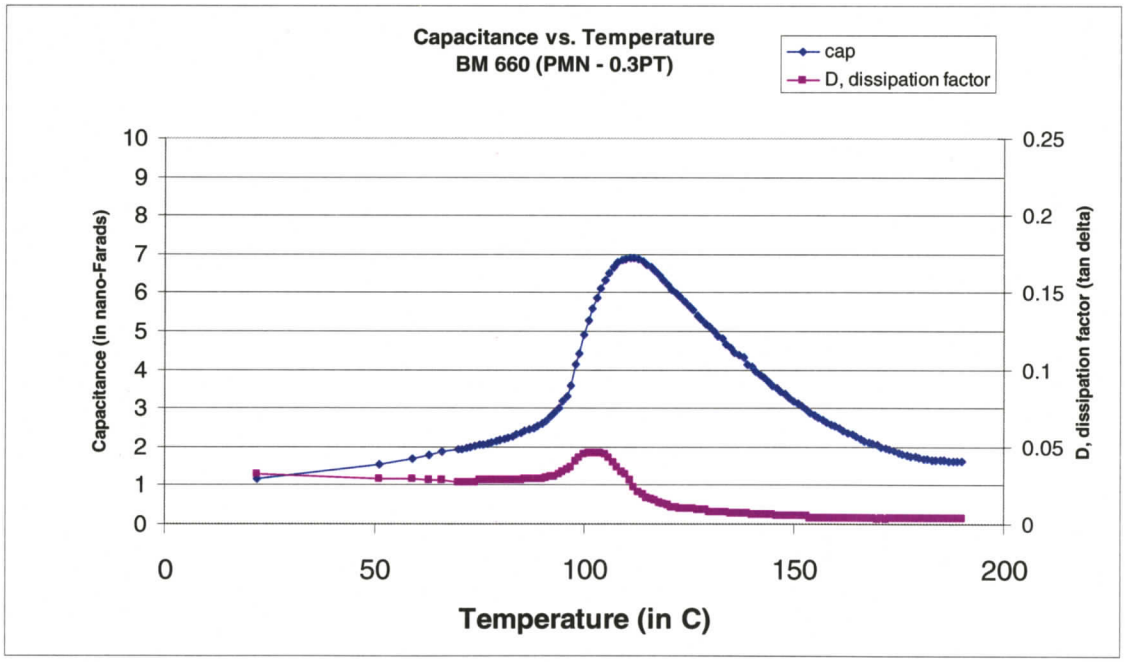

Figure 5-4 Capacitance vs. Temperature for PMN-0.3PT

Similar measurements made on the PMN-0.3PT specimen are shown in Figure 5-4. The capacitance of this sample also exhibited a broad maximum, which occurs at 111 ± 1°C, confirming that this composition also displays relaxor behaviour in this intermediate temperature region, before the onset of the piezoelectric properties observed at room temperature. The dissipation factor (tan δ) also passes through a relatively broad maximum, which occurs between 102 °C and 103 °C.

The temperature dependence of the capacitance of the experimental PZT BM200, which has not been well characterized, is shown in Figure 5-5. The capacitance vs. temperature plot displays distinct ferroelectric properties, with a very sharp increase in dielectric constant at a clearly defined Curie temperature of 455°C. This relatively high Curie

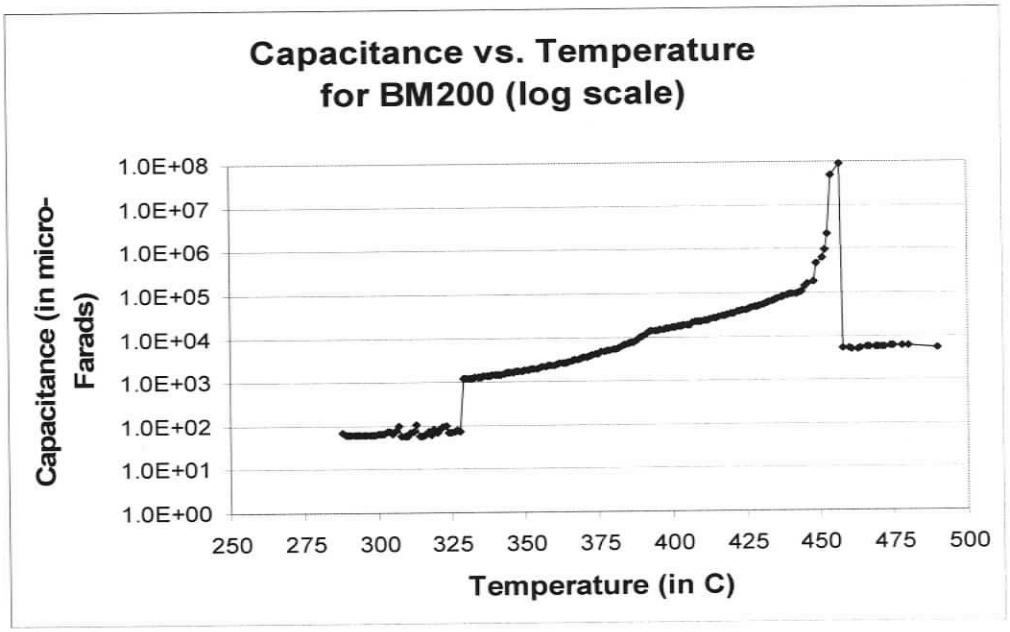

Figure 5-5 Capacitance vs. Temperature for BM200 (log scale)

temperature is to be expected for a biased field doped hard PZT piezoelectric (see for example the data listed in Table 2-2). The plot in Figure 5-5 shows a distinct drop, typical of a first order phase transformation, at a temperature of 330 °C, at which the PZT would be expected to cross the morphotropic phase boundary between the tetragonal and rhombohedral structures.

5.2.2. Polarization vs. Field Measurements

5.2.2.1. PZT Ceramics

The polarization vs. electric field plot for the PZT ceramic BM532 over the range of ± 2.8 MV/m is shown in Figure 5-6. The plot has a symmetrical square hysteresis loop, which is typical of a relatively soft piezoelectric [59]. The saturation polarization P_S of the sample is 0.42 C/m^2 and the remanent polarization P_R of 0.32 C/m^2 is 75% of saturation, as shown in Table 5-1. The sample displays very sharp switching in the sign

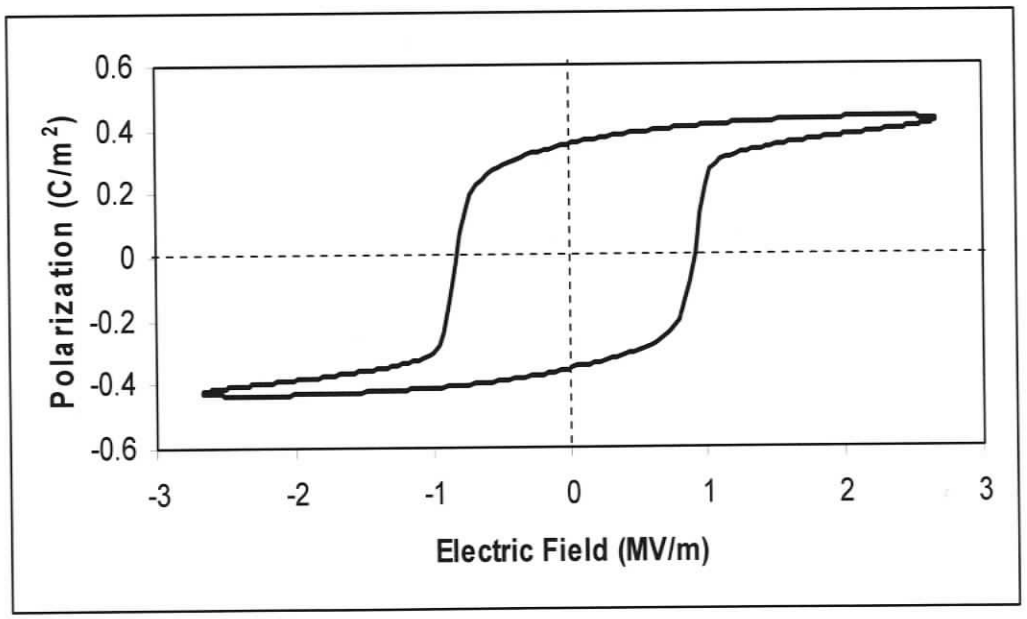

Figure 5-6 Polarization vs. electric field plot for the PZT ceramic BM532

of polarization on passing through the coercive field E_C, which has an average value of 0.88 MV/m, measured over several specimens. This value of coercive field was used to calculate normalized electric fields E/E_C, for use in later field dependent experiments on this ceramic.

The polarization versus field plots for PZT ceramics BM200 and BM800 over the range of ± 3.1 MV/m are given in Figure 5-7. The saturation polarization in these samples is 0.42 C/m^2 and 0.52 C/m^2, respectively. The remanent polarization is very high, at 95% of P_S, as shown in Table 5-1. The hysteresis plots for BM200 and BM800 are not completely square, so the switching of the sign of polarization at the coercive field is not quite as sharp as that observed in the soft piezoelectric BM532. The hysteresis loops also show significant asymmetry with respect to the zero point of the electric field scale, due to an internal bias field, E_i, which was induced by selective doping with the oxides of nickel, iron or strontium [59], to give these ceramics hard piezoelectric properties. The

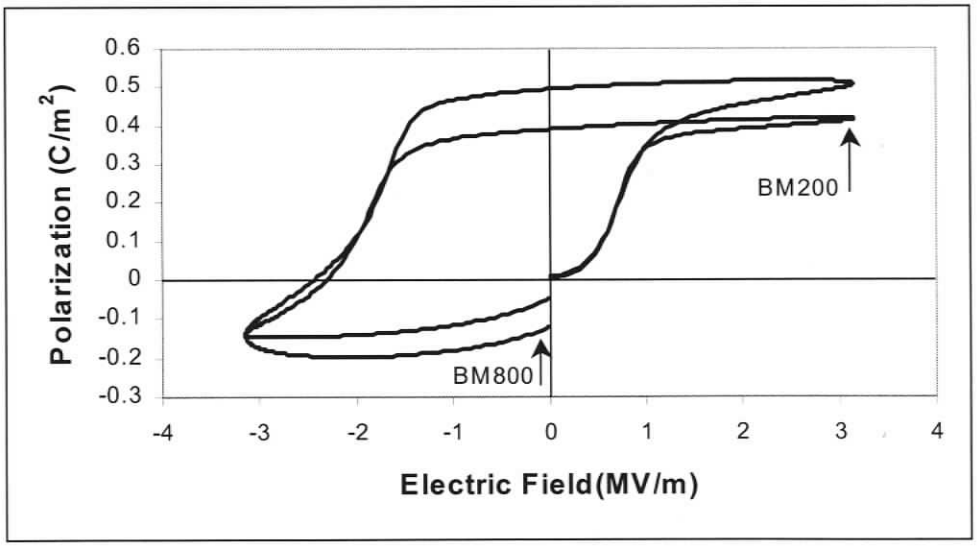

Figure 5-7 Polarization vs. electric field plots for the PZT ceramics BM200 and BM800

value of E_i, deduced from the horizontal displacement of the loop centre from the E = 0 axis [25] is equal to -0.61 MV/m for BM800 and -0.66 MV/m for BM200. The effective coercive fields, deduced from the left hand half-plane of the P-E loops, of -1.88 MV/m for BM800 and -1.94 MV/m for BM200 are significantly greater than the value of 0.8 MV/m measured above for the soft piezoelectric BM532 as shown in Table 5-1. These effective coercive fields were used to calculate normalized electric fields for use in subsequent experiments using these hard piezoelectrics.

Table 5-1 Ferroelectric Properties of PZT and PMN-PT Ceramics

Ceramic	P_S (C/m^2)	P_R (C/m^2)	P_R/P_S	E_C (MV/m)
BM532	0.42	0.32	75%	-0.88
BM200	0.40	0.38	95%	-1.88
BM800	0.52	0.50	95%	-1.94
PMN-0.3PT	0.30	0.23	75%	0.36
PMN-0.08PT	0.30	0.01	3%	0.01

5.2.2.2. PMN-PT Ceramics

The polarization vs. electric field plot for the ceramic of composition PMN-0.3PT is shown in Figure 5-8. The symmetrical square hysteresis loop of this plot is similar to that observed for BM532 in Figure 5-6, indicating that this PMN-PT composition is also a soft piezoelectric. The saturation polarization of PMN-0.3PT, at 0.3 C/m^2, is much smaller than the value obtained for BM532, as shown in Table 5-1, but the ratio of the remanent polarization to the saturation polarization is also 75%. The square loop indicates sharp switching on passing through the coercive field, which was determined as

0.36 MV/m, from the average of measurements made on several samples. This value, which is less than half that obtained for BM532 (see Table 5-1), was used to calculate reduced fields for subsequent experiments using this PMN-PT composition.

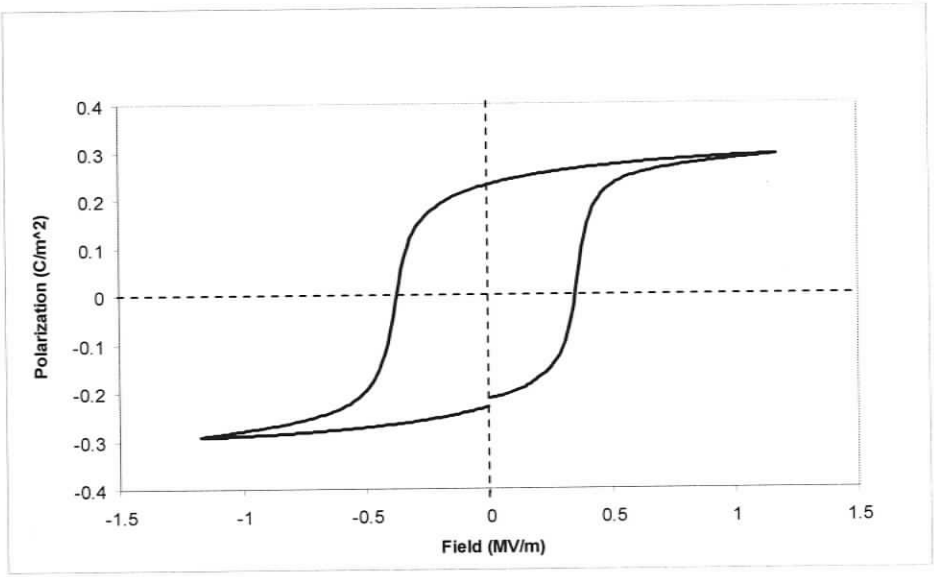

Figure 5-8 Polarization vs. electric field plot for PMN-0.3PT

The polarization vs. electric field plot for the ceramic of composition PMN-0.08PT shown in Figure 5-9 exhibits a saturation polarization of 0.3 C/m^2, which is closely similar to that observed for the piezoelectric composition PMN-0.3PT. However, the plot displays very little hysteresis when the field is reversed, and shows no significant remanent polarization when the electric field is reduced to zero. The coercive field when the direction of the field is reversed is also very close to zero, as indicated by the data in Table 5-1. This reversible type of hysteresis plot is indicative of electrostrictive, as opposed to piezoelectric, properties [65].

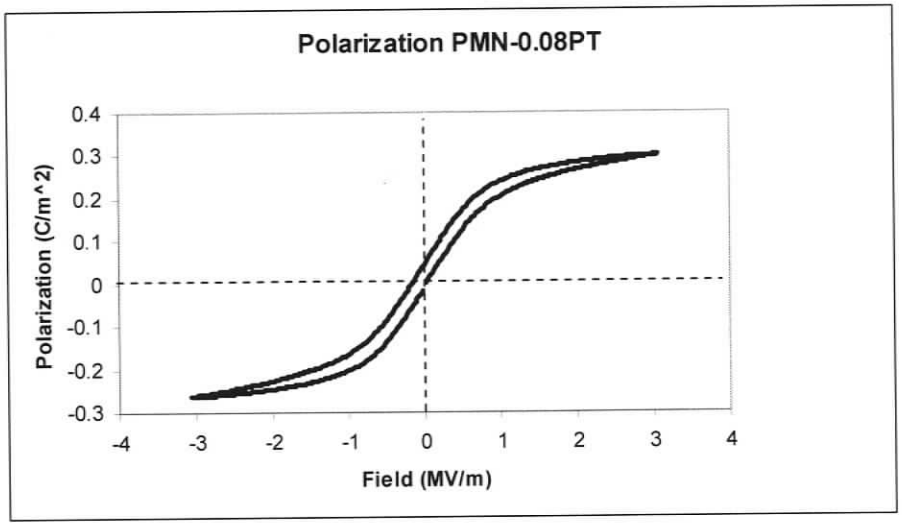

Figure 5-9 Polarization vs. electric field plot for PMN-0.08PT

5.2.3. Strain vs. Field Measurements

The strain vs. field plot for the piezoelectric PMN-0.3PT specimen in Figure 5-10 shows that this sample exhibits a strain of 0.15% in an applied field of 2 MV/m. The hysteresis observed on reversing the field occurs because the polarization that induces the strain is not linearly dependent on the applied field, as indicated above by the polarization vs. field plot in Figure 5-8. After the specimen is poled, by increasing the field to saturate the polarization and then reducing it to zero, there is a residual strain of 0.05%. The figure also shows that for practical applications using ceramics in the poled condition, the strain vs. field plot is approximately linear in applied fields 75 and 175 kV/m. For this reason, these piezoelectrics are often used in biased fields of ~100 kV/m [6].

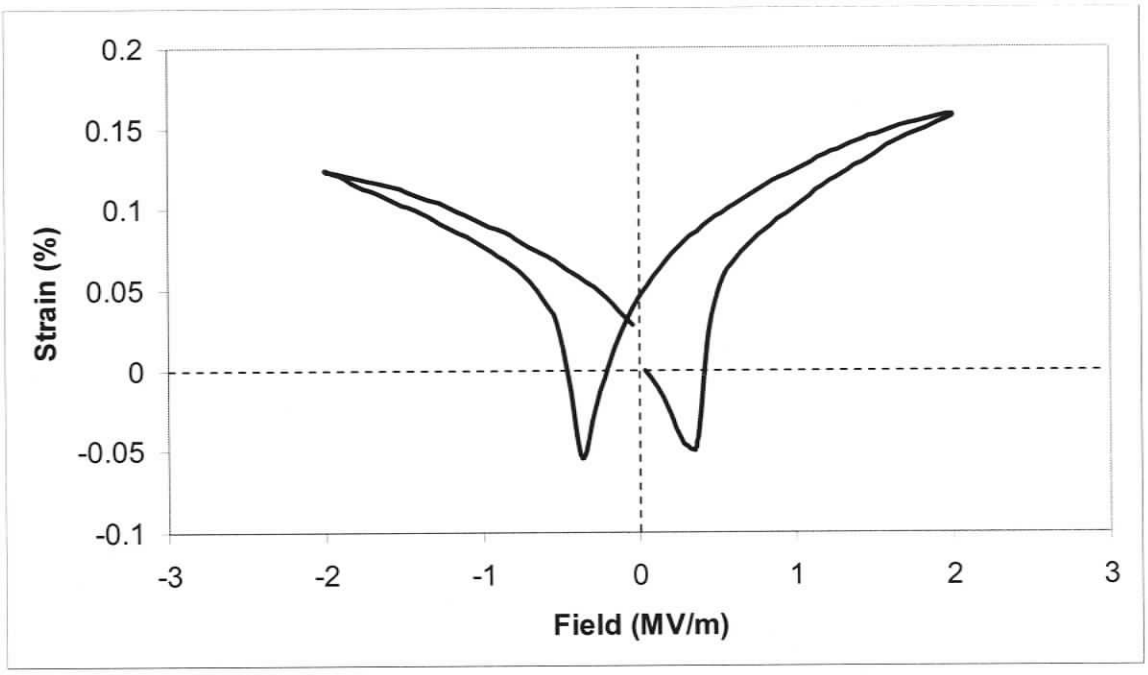

Figure 5-10 Strain vs. field plot for PMN-0.3PT

The strain vs. field plot for the PMN-0.08PT specimen is shown in Figure 5-11. The plot follows the E^2 dependence of strain on applied field that is expected for an electrostrictive ceramic [31], but shows considerable hysteresis in reversed fields. This observation is consistent with a relaxor ferroelectric which has a small degree of piezoelectricity, which is known to be present in PMN–PT ceramics, and to increase in amount with increasing PT content, as discussed in Section 2.2.2.3 above. The incidence of a small amount of piezoelectric behaviour could also explain why the polarization vs. field plot for this specimen in Figure 5-8 is not completely reversible.

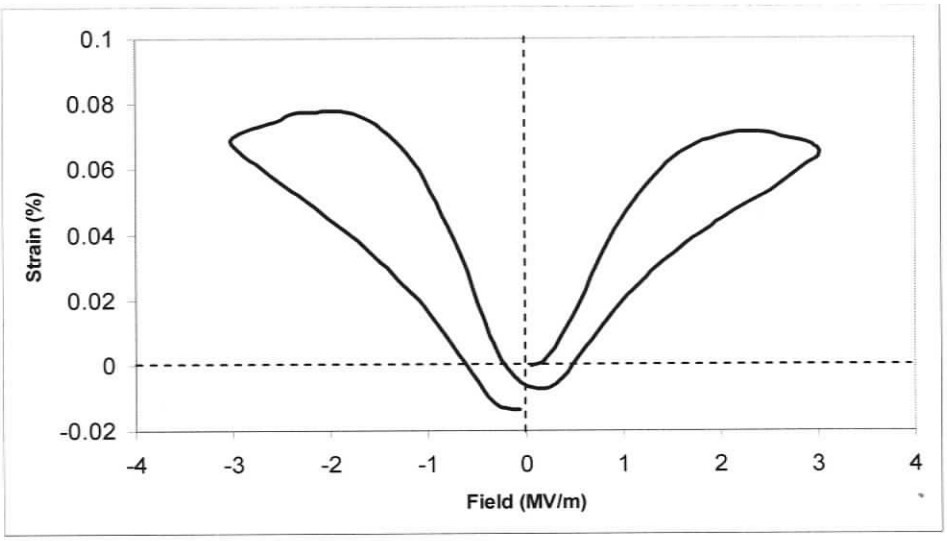

Figure 5-11 Strain vs. field plot for PMN-0.08PT

5.2.4. Discussion: Coercive Fields for Hard Piezoelectric PZT Ceramics

Since all commercial compositions of PZT contain some degree of internal bias, which is introduced by selective doping, measurements of the coercive field E_C taken from the resulting asymmetrical P – E hysteresis loops of the type shown in Figure 5-7 can be misleading, especially when there is a large internal bias in hard piezoelectrics such as BM200 and BM800. The hysteresis loop, which is symmetrical in soft piezoelectrics such as BM532, is offset horizontally from the zero axis due to the internal bias field, E_i. Since comparing only the E_C values does not take into account the span of the hysterisis loop, it is suggested that an effective coercive field E_C', be defined as:

$$E_C' = E_C - E_i \qquad \text{Equation 5-1}$$

Once the hysteresis loop has been shifted to its origin of symmetry, then:

$$+E_C' = -E_C'$$

In this manner, P – E hysteresis loops generated for both soft and hard piezoelectrics may be compared, without the offsets generated by internal fields, to give more meaningful comparative values for the various ferroelectric parameters.

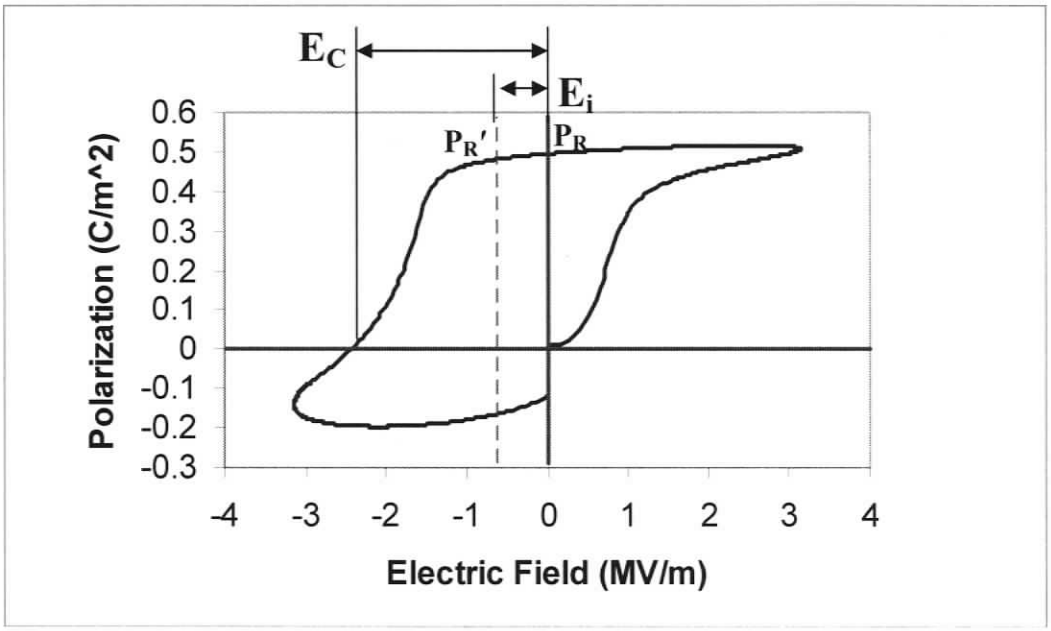

Figure 5-12 Hysteresis loop showing biased field (E_i) and E_C

Applying this parameter to the present results in Figure 5-7, gives $E_C' = -1.28$ MV/m for BM200 and -1.27 MV/m for BM800. Although these effective coercive fields are significantly reduced from the measured values of -1.94 and -1.88 MV/m, they apply in both negative and positive fields, and provide a reasonable comparison (of 1.45 times) the coercive fields for soft piezoelectrics, such as BM532.

5.3. Phase Transformations in PMN-PT Ceramics

The temperature dependence of the crystal structure transformations that occur in the vicinity of the Curie temperatures of the PMN-PT ceramics were investigated, in order to establish a more definitive phase diagram of this important ceramic system.

5.3.1. Preliminary X-ray Diffraction Experiments

5.3.1.1. Lattice Parameter Changes in Powder Specimens

In a preliminary experiment to locate the temperature of the second order structural phase transformation in PMN-PT, the lattice parameters of a powder sample of composition PMN-0.1PT were measured over a temperature range from -50 to 300 °C, in a vacuum of 10^{-3} torr. A distinct change in the slope of the lattice parameter vs. temperature plot was

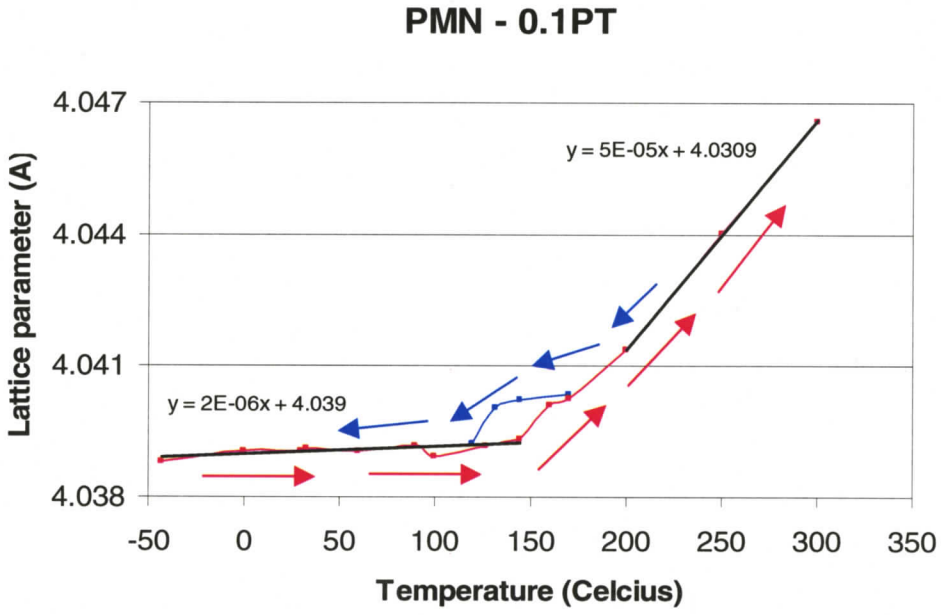

Figure 5-13 Lattice parameter vs. temperature for PMN-0.10PT powder sample

observed near 150 °C, as shown in Figure 5-13. This change in slope represents an order of magnitude increase in the thermal expansion coefficient of the specimen, which is one

of the defining characteristics of the second order structural phase change that occurs in relaxor ferroelectrics [38, 38, 114]. The thermal inertia observed in the region of the change in slope, is attributed to the measuring thermocouple being attached to the heater, as opposed to the specimen itself. As discussed in the Experimental Section above, this thermocouple attachment also causes the measured temperature to be several degrees hotter than the actual temperature of the irradiated surface of a poorly thermal conducting powder specimen [106]. However, this error does not of itself negate the general observation of a change in lattice stiffness on cooling through the region of the dielectric transition. To obtain a more precise measurement of the temperature of this stiffness change, further lattice parameter measurements were conducted on ceramic specimens using the surround heater of the Buehler furnace and the specimen mount described in the Experimental Section.

5.3.1.2. Effect of Vacuum on Temperature Dependence of Phase Stability

In further preliminary experiments, it was noticed that when ceramic specimens of PMN and PMN-0.08PT were heated to 300 C in a vacuum of 10^{-5} torr, the colour of the exposed surfaces changed from a light yellow to a medium shade of grey. It was suspected that this colour change may be related to the small local thermal hysteresis observed in the vicinity of the intersection of the heating and cooling plots, as shown in Figure 5-14. Subsequent heating of these and other PMN–PT specimens to 300 °C showed that no change in colour occurred when heating in atmosphere; so all remaining

lattice parameter experiments were conducted on ceramic specimens in atmospheric conditions.

Possible compositional variations through the cross-sections of samples heated in vacuum were investigated by both light microscopy and scanning electron microspectography, The light micrograph in Figure 5-14 shows that the discolouration of the PMN-0.08PT specimen is restricted to a narrow surface layer, which is on the right hand side of the picture. However, no changes in composition were detected by energy dispersive X-ray spectroscopy when the cross-section and outer surfaces of the specimens were examined by an EDAX attachment on a scanning electron microscope.

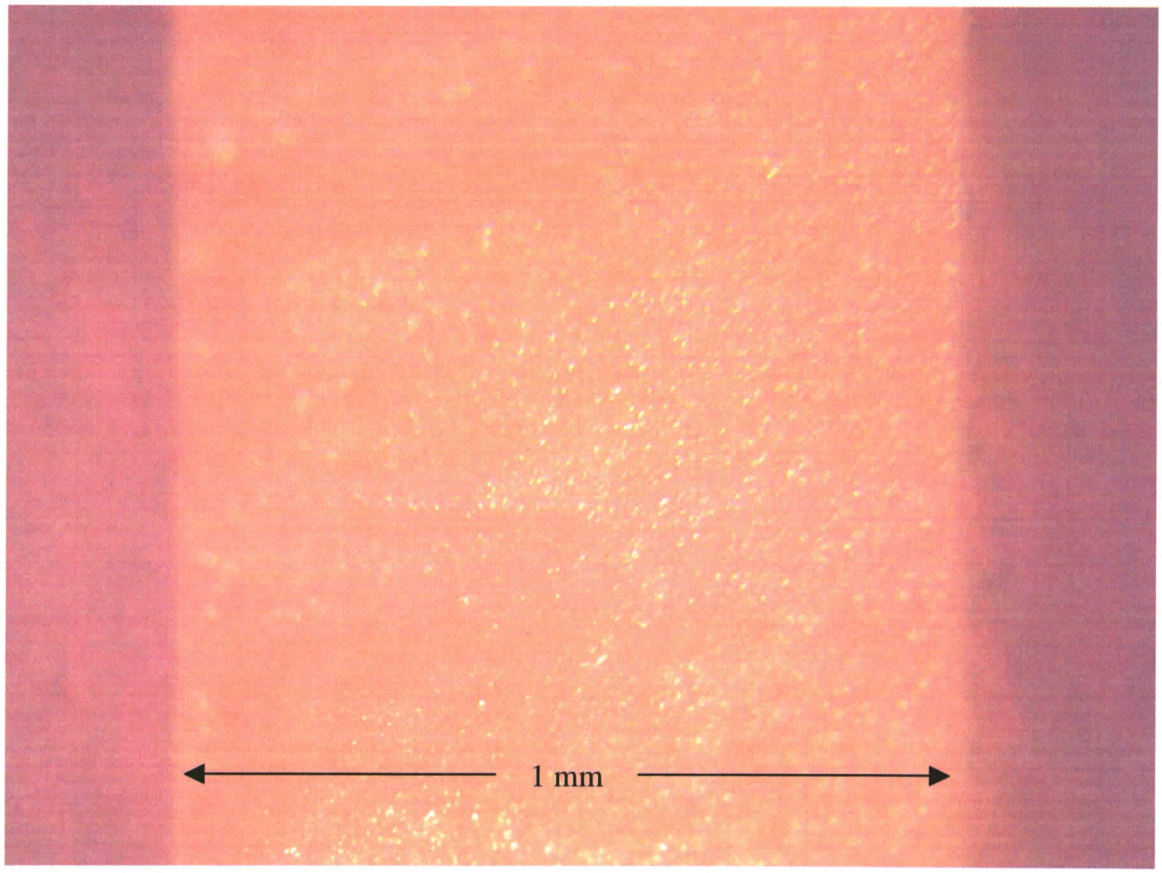

Figure 5-14 Light micrograph of the cross-section of PMN-0.08PT

5.3.2. Temperature Dependence of Lattice Parameters

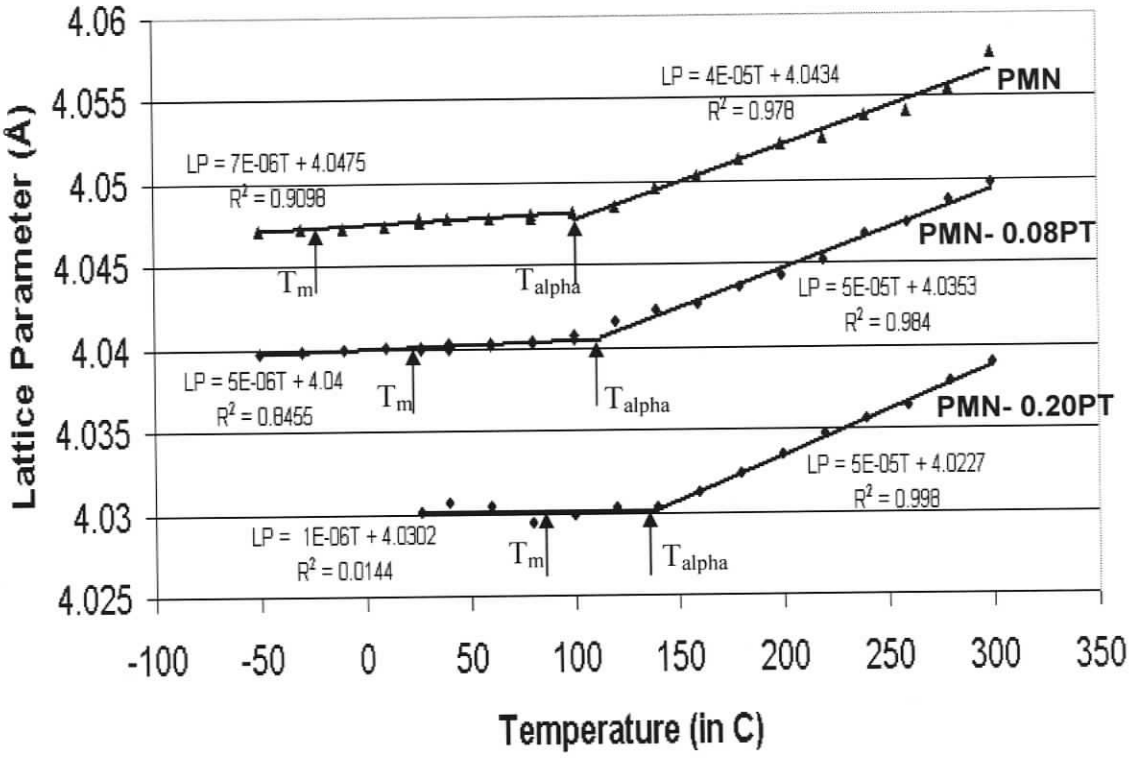

Figure 5-15 Lattice Parameters vs. Temperature for PMN-xPT, where x = 0.00, 0.08, 0.20

The *a* lattice parameters derived from pseudocubic indexing of the diffraction patterns of PMN–PT specimens containing 0.00, 0.08 and 0.20 mole fractions of PT are shown in Figure 5-15. Diffraction peaks in the high angle region were scanned at 20 °C intervals over the temperature range from -50 to +300 °C. At the higher temperatures, these lattice parameter vs. temperature plots are strictly linear with slopes consistent with a thermal expansion coefficient (α) of the order of 10^{-5} mm/mm per °C. However, all of the lattice parameter plots in Figure 5-14 show a very significant decrease in slope on cooling below a well defined temperature, labeled T_α. The slopes of these low temperature linear plots

indicate that the thermal expansion coefficients are decreased by an order of magnitude, to the level of 10^{-6} mm/mm per °C.

The pseudocubic *a* lattice parameters of PMN–PT specimens containing 0.30 and 0.35 mole fractions of PT were also determined at 20 °C intervals over the temperature range from 27 to 300 °C, as shown by the plots in Figure 5-16. The high temperature plots of these lattice parameters are again strictly linear, with slopes indicative of a relatively high thermal expansion coefficient of 5-6 x 10^{-5} mm/mm per °C. Once again, the plots show a sharp change in slope on cooling through a distinct temperature labelled T_α. The slopes of these lower temperature linear plots slopes are indicative of much smaller thermal expansion coefficients of 1-3 x 10^{-7} mm/mm per °C.

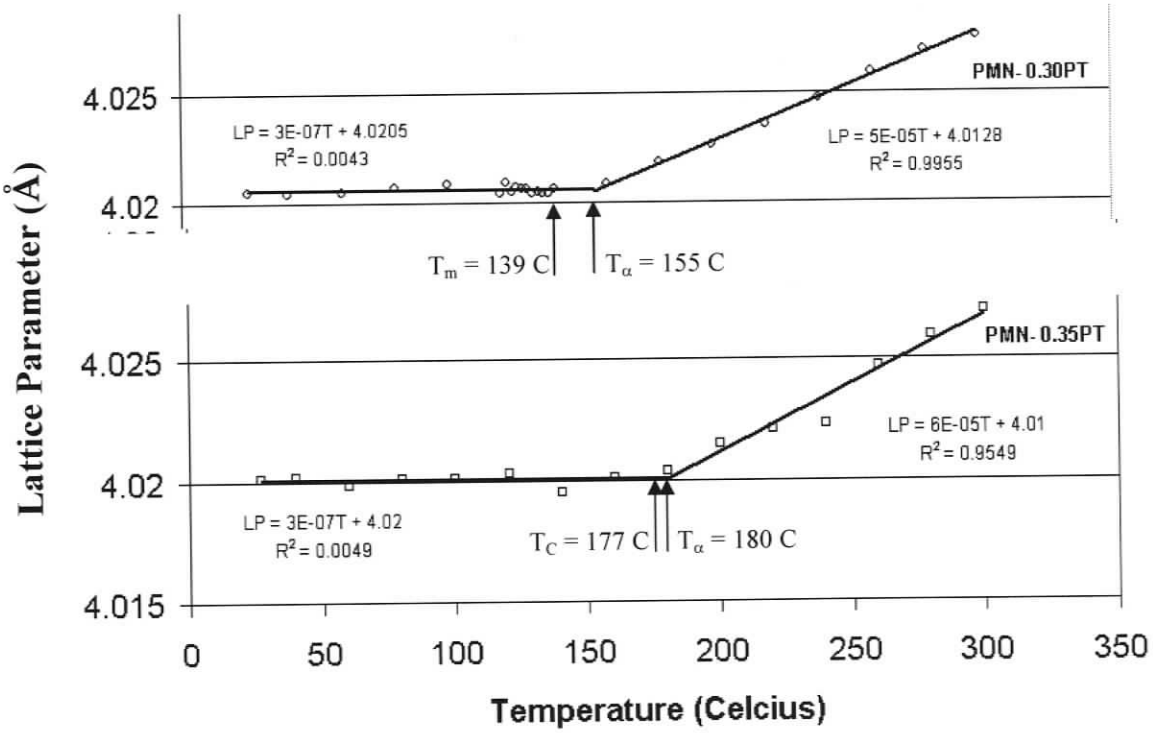

Figure 5-16 Lattice Parameters vs. Temperature for PMN-xPT, where x = 0.30, 0.35

It is significant to note that the pronounced decrease observed in the thermal expansion coefficient of these PMN–PT specimens is in qualitative agreement with the earlier lattice stiffening results of Smolenskii et al [38, 38] and with the sequence of perovskite structures observed on cooling $BaTiO_3$, where a 4% decrease in cell volume/molecule is observed on going from the cubic to the tetragonal, orthorhombic or rhombohedral structures [115]. The present results are also quantitatively consistent with the findings of Cross [114], who reported α values of 10^{-5} mm/mm per °C at 400 °C and $< 10^{-6}$ mm/mm per °C at room temperature, for a sample of PMN-0.1PT and with the recent lattice parameter results of Xu et al. [34], which are shown in Figure 2-24 above.

The results in Figures 5-15 and 5-16 , and the previous results of Xu et al. in Figure 2-24, show that the T_α temperatures at which lattice stiffening occurs are not directly related to the temperature T_m, associated with the maximum of the broad peak in dielectric constant, which is a characteristic of relaxor ferroelectrics. The T_α results in Figures 5-15 and 5-16 are compared to published T_m values in Table 5-2. The difference of 78°C between the T_α and T_m values for the present sample of PMN-0.08PT is in very close agreement with the equivalent temperature difference of 80°C, reported by Xu et al. [34] for a sample of PMN–0.1PT. It is also evident from the table, that the T_α temperatures obtained for the lower PT compositions deviate significantly from the respective values of T_m , but the difference between the two sets of temperatures decreases with increasing

PT content, so that the T_α of the piezoelectric PMN–0.35PT ceramic is in agreement with its T_C temperature, to within the accuracy of the two

Table 5-2 Temperatures of Changes in Coefficient of Thermal Expansion

	Present	Previous Results			
Ceramic	T_α (°C)	T_c (°C)	T_m (°C)	T_f (°C)	Refs. **[T_m / T_f]**
PMN-**0.00**PT	103	--	-15 to -18	-43 to -60	[67, 38 / 74, 68, 117, 118]
PMN-**0.08**PT	110	--	32	6	Interpolated values
PMN-**0.10**PT	110	--	38	18	[6, 64 / 116]
PMN-**0.20**PT	134	--	93	57	Interpolated values
PMN-**0.24**PT				80	[117]
PMN-**0.25**PT	------	--	127	77	[67 / 42]
PMN-**0.30**PT	155	--	139	--	[67, 68]
PMN-**0.35**PT	180	170-177	--	--	[67, 68]

measurements. The significance of the present T_α results is discussed in Section 5.3.4, in the context of the boundary between the cubic and pseudocubic phases in the PMN-PT ceramic system, which up to now have always been associated with the temperature of the dielectric maximum, T_m [34, 48, 67, 68, 83, 86].

5.3.3. Temperature Dependence of Diffraction Profiles

To identify more precisely the structural changes that occur in the PMN-PT ceramics, the profiles of selected diffraction peaks were recorded under high resolution conditions at temperature intervals of approximately 20 °C over ranges of temperature from -50 to +300 °C. The profiles shown in Figure 5-17 refer to the 332 peak, which was selected because it occurs at a high enough Bragg angle for the $K_{\alpha 1}$ peak at 126.35 °2θ to be clearly distinguished from the $K_{\alpha 2}$ peak at 126.95 °2θ, while its diffracted intensity is sufficiently large to be clearly distinguished above the background radiation. If the structure were to transform completely from cubic to the expected rhombohedral structure, the 332 peak would split into a triplet composed of a low angle 332 peak, a middle angle $33\bar{2}$ peak and a high angle $3\bar{3}2$ peak. If the rhombohedral unit cell angle, α, is sufficiently distorted from 90 °, the 332 peak would appear to be quite separate, but the $33\bar{2}$ and $3\bar{3}2$ peaks are likely to still be overlapped to some extent.

The results for the PMN-0.2PT sample reveal the clearest trend of structural changes on cooling. At 300 °C, the cubic 332 peak occurs at a lower Bragg angle, consistent with its

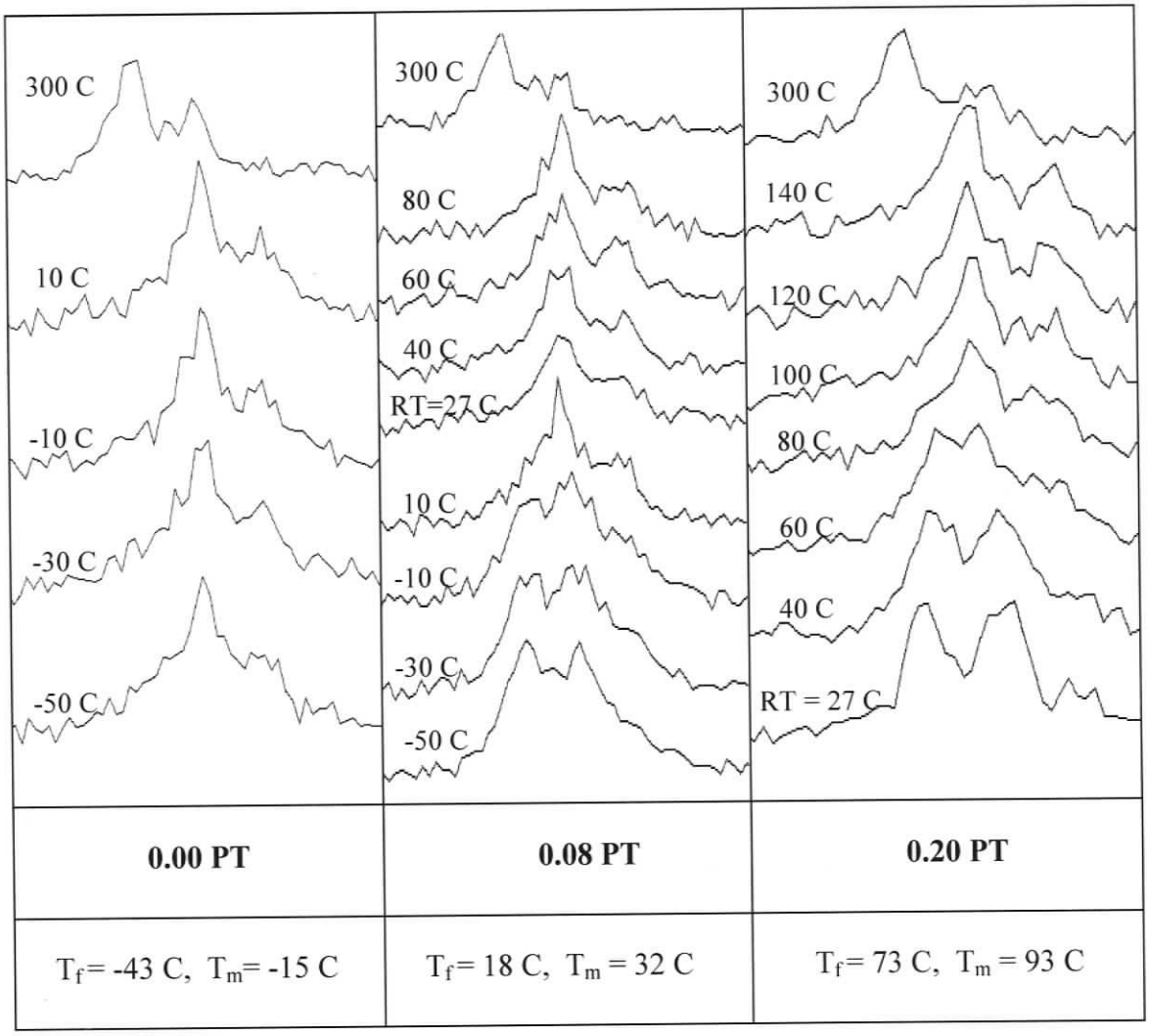

Figure 5-17 Temperature dependence of 332 profiles for PMN, PMN-0.08PT and PMN-0.20PT

larger lattice parameter. At 140 °C, which is just above the T_α temperature of 134 °C, the 332 peak is shifted to higher angles, but still shows the cubic $K_{\alpha1}$-$K_{\alpha2}$ doublet. The cubic $K_{\alpha1}$-$K_{\alpha2}$ doublet is retained on cooling to 80 °C, but the lower angle shoulder of the peak is broadened. On further cooling to 60 °C, a more distinct rhombohedral 332 peak appears at an angle below the cubic $K_{\alpha1}$ peak, while a broad unresolved rhombohedral $33\bar{2}$ - $3\bar{3}2$ peak appears in the angular range of the cubic $K_{\alpha2}$ peak. On further cooling, the rhombohedral structure is clearly evident, as a lower angle relatively sharp peak and a

higher angle broader peak with the same intensity. It is also significant to note that the rhombohedral structure does not form at the T_m temperature of 93 °C, but at some lower temperature between 80 and 60 °C, which is close to its T_f temperature of 73 °C.

Similar structural trends are evident from the diffraction patterns obtained during the cooling of the PMN-0.08PT sample. The broadened cubic 332 peak is observed at temperatures from above 80 °C down to room temperature, while the rhombohedral diffraction pattern appears between –10°C and +10 °C. It is again significant to note that the temperature of the onset of the rhombohedral phase does not concur with either the T_m of 32 °C, or with the T_f temperature of 18 °C. In the PMN-0.00PT sample, the broadened pseudocubic peaks are observed on cooling down to the lowest experimental temperature of -50 °C, which is well below both the T_m temperature of –18°C and near the T_f temperature -43 °C. These observations are consistent with similar profile broadening of the 332 peak of PMN-0.00PT observed at temperatures down to 5K by de Mathan et al. [47], who were able to fit their data to a model of the cubic structure containing nano-polar rhombohedral regions of the type shown previously in Figure 2-25. The practical importance of the X-ray diffraction results for these relaxor ferroelectrics is that the room temperature structures of the PMN and PMN-0.08PT compositions are pseudocubic with significant internal strains, as opposed to the rhombohedral structure observed at higher PT compositions in the PMN-PT ceramic system.

The temperature of the structural transformation from cubic to pseudocubic is more difficult to assess, as the cubic diffraction profiles are strain broadened due to the pressing-sintering fabrication treatment of these specimens. Referring again to the PMN-0.2PT sample, the cubic 332 peak shows additional broadening, particularly in the vicinity of the $K_{\alpha 2}$ peak, on cooling over the temperature range between 140 and 120 °C, which includes the T_α temperature of 134 °C. Similar broadening in the vicinity of the $K_{\alpha 2}$ peak of the PMN-0.08PT sample can be observed at 80 °C. While the onset of this broadening is consistent with the T_α temperature of 110 °C, the precise temperature of the onset cannot be derived from the presents results, as no profile measurements were made between 80 °C and 300 °C. The onset of broadening in the PMN-0.00PT sample occurs at some temperature in the range between 10 °C and 300 °C, which again includes the T_α temperature of 103 °C.

The profiles of the 332 diffraction peaks of the PMN-0.3PT and PMN-0.35 samples are shown in Figure 5-16. The PMN-0.3PT specimen exhibits a well resolved cubic $K_{\alpha 1}$-$K_{\alpha 2}$ profile at temperatures of 180 and 160 °C. Small satellite peaks on the shoulders of the cubic $K_{\alpha 1}$ peak at 140 °C are attributed to tetragonal splitting, the onset of which can be identified with the T_α temperature of 155 °C. Additional, more widely separated satellite peaks, observed on the lower slopes of the $K_{\alpha 1}$ peak at 120 °C are associated with the onset of an intermediate monoclinic, or orthorhombic structure, of the type observed by [79-85]. On further cooling, below 80 °C, when this sample would cross the morphotropic phase boundary at 77 °C [68], additional unresolved broad peaks appear

between the widespread peaks to create a broad plateau. This structural pattern extends to room temperature.

The 332 diffraction profiles of the PMN-0.35PT sample in Figure 5-18 also exhibit a well-resolved cubic K_{α_1}-K_{α_2} profile at temperatures down to 200 °C. The tetragonal splitting observed at 180 °C, and below, is consistent with cooling through the T_α temperature of 180 °C, which is almost coincident with the reported T_C of 177 °C [68].

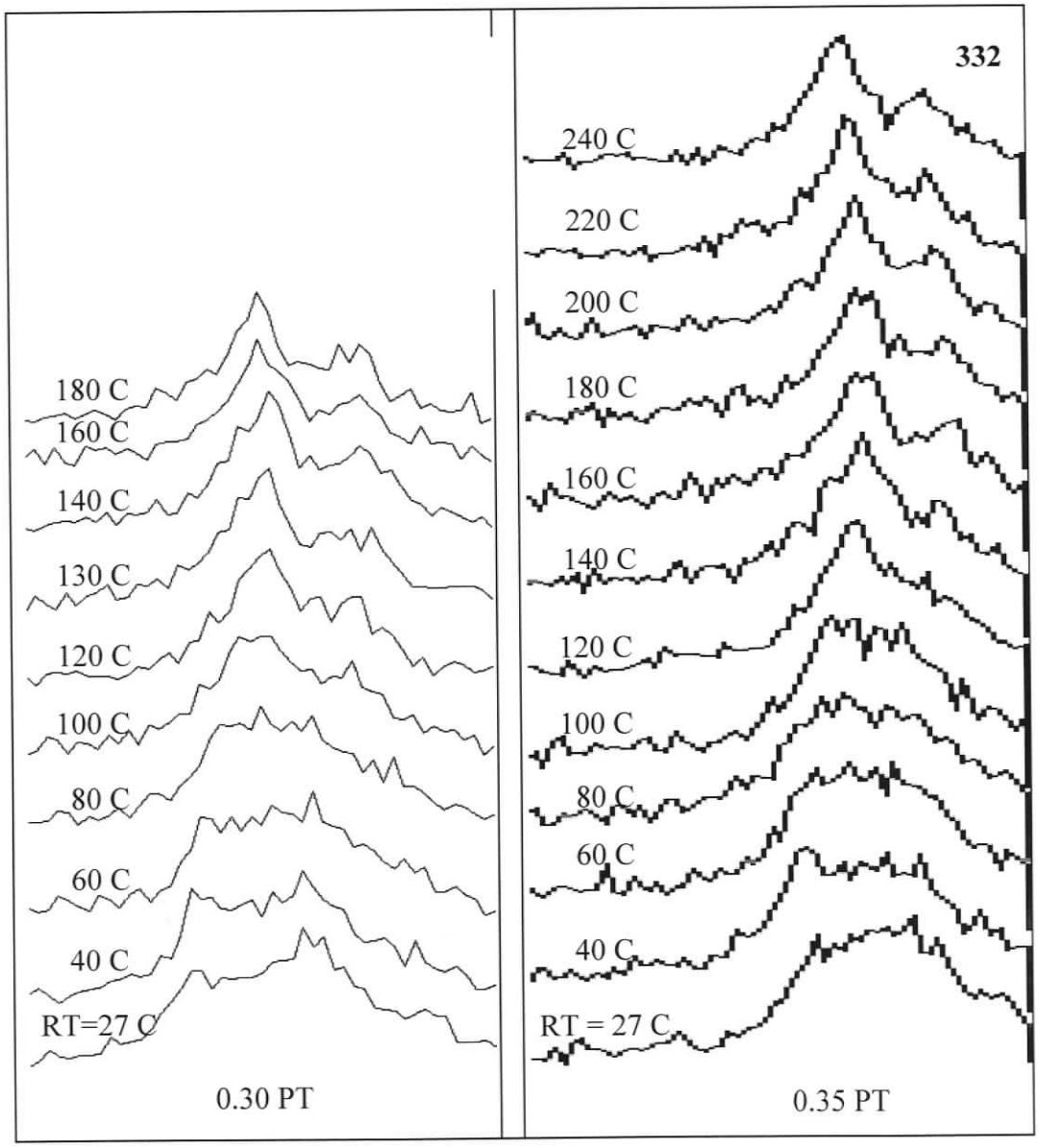

Figure 5-18 Temperature dependence of 332 profiles for PMN-0.3PT and PMN-0.35PT

Additional widespread satellite peaks associated with the intermediate monoclinic phase are observed between 100 and 120 °C. Widely separated peaks of the monoclinic structure are again observed on cooling between 120 and 100 °C. These satellite peaks disappear between 80 and 60 °C, when the pattern becomes a broad unresolved plateau of peaks.

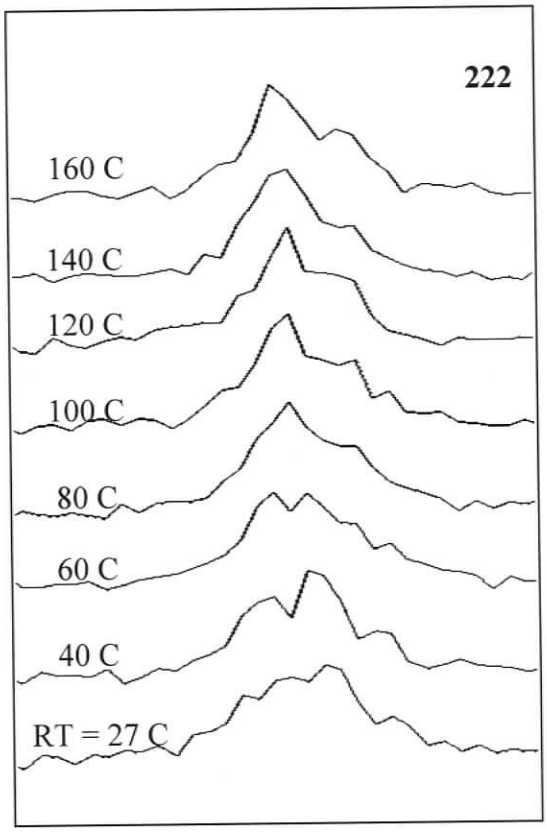

Figure 5-19 Temperature dependence of 222 profiles for PMN-0.35PT

In order to identify the temperature of the onset of the additional low temperature peaks, the 222 peak of the PMN-0.35PT sample was step scanned over the temperature range from 160 °C down to room temperature, to obtain the results given in Figure 5-19. The 222 Bragg peak was selected because it does not split into a tetragonal doublet, or a

triplet of orthorhombic peaks. These diffraction profiles show only a broadened $K_{\alpha 1}$-$K_{\alpha 2}$ peak on cooling to 80 °C. At 60 °C and below, the 222 peak shows splitting due to the separation of the 222 and $\bar{2}22$ peaks of the rhombohedral structure, confirming that these peaks contribute to the multiple unresolved peaks that are superimposed in the broad plateau of the low temperature 332 profile. This observation indicates that the PMN-0.35PT sample crosses the morphotropic phase boundary between 60 and 80 °C. These findings are in good agreement with the recent results of Kojima and Jiang [116], who report that PMN-0.35PT undergoes a cubic to tetragonal change at 158 °C and a further tetragonal to rhombohedral change at 60 °C.

It is significant to note that broadened profiles with multiple peaks were also observed for PMN-PT samples at room temperature by Ho *et al.* [48], but these authors did not analyze, or comment on, their findings. However, they did report that a sample of composition PMN-0.32PT had a bimodal microstructure at room temperature, composed of a small number of 4 μm grains mixed with a larger number of 9 μm grains, which implied the coexistence of two phases, i.e. the ceramics enter a two-phase region after crossing the morphotropic phase boundary. The progressive changes in the diffraction profiles shown in Figures 5-17, 5-18 and 5-19 also confirm that the boundaries between structural phases in the PMN-PT system, including the MPB, should be regarded as two-phase regions, rather than single width lines.

It is evident from the diffraction profiles in Figures 5-17, 5-18 and 5-19, that the structural transformations do not go to completion at the temperature of the initial

observation of a new structure, but the amount of the new phase increase with decreasing temperature, i.e. these displacive phase transformations have athermal characteristics. The temperature ranges of the observed structural transformations in PMN-PT ceramics are summarized in Table 5-3 below.

Table 5-3 Temperature Ranges of the Onset of Structural Changes in PMN-PT Ceramics

Ceramic	Cubic - Ps-cubic (°C)	Ps-cubic - Rhomb (°C)	Cubic - Tetrag (°C)	Tetrag - Mono (°C)	Mono - Rhomb (°C)
PMN	>-10	Not observed	--	--	--
PMN-0.08PT	>80	-10 to +10	--	--	--
PMN-0.20PT	120-140	60-80	--	--	--
PMN-0.3PT	--	--	140-160	120-140	60-80
PMN-0.35PT	--	--	180-200	60-80	RT-40

5.3.4. Discussion: A Revised Phase Diagram for the PMN-PT System

5.3.4.1. Compositions in the Region of the Relaxor Transition

The results presented in Sections 5.3.2 and 5.3.3 indicate that structural transformations can take place in relaxor compositions of PMN-PT, at temperatures well above the temperature, T_m, of the maximum in the temperature dependence of the dielectric constants. There are also indications that structural transformations can occur near the temperature T_f, at which spontaneous polarization is observed in relaxor ferroelectrics. These findings are somewhat contradictory to the published phase diagrams for the PMN-PT ceramic system, which are based primarily on the temperature dependence of dielectric properties [48, 67, 68, 83, 116, 119].

Since the broadened diffraction profiles shown in Figure 5-17 indicate that the onset of the cubic to pseudocubic phase transformation in relaxor compositions of PMN-PT may be associated with the temperature T_α at which the crystal lattice shows a marked increase in mechanical stiffness on cooling. It is of interest to plot the experimental values of T_α (see Table 5-2) on the "phase diagrams" of the PMN–PT system developed by Choi et al. [67] and Feigelson [74] from measurements of T_m. It is evident from the plots in Figure 5-20 that the T_α temperatures increase linearly across the relaxor region. The plot of T_α is widely separated from the T_m plot at the composition of PMN, but intersects the T_m plot in the region of the morphotropic phase boundary near PMN-0.30PT. The values of T_α also fall well below the maximum temperatures of 343 –345 °C at which Burns and Dacol [42] infer (on the basis of refractive index measurements), that randomly oriented regions of polarization can form in PMN. There is a lack of precise

data on the maximum temperature $TP_{s=0}$, at which the saturation polarization goes to zero in relaxors, but as this temperature is generally considered to be no more than 100 °C above T_m [33, 41], it is reasonable to associate it with the present values of T_α, at which the crystal lattice becomes significantly softer on heating. The lattice stiffening can thus be regarded as a necessary condition for the formation of stable oriented regions of polarization, which contribute to saturation polarization. The random orientation of these regions causes the structure to be macroscopically cubic, with broadened diffraction profiles, while the lower symmetry in the microscopic regions supports the distributed dipoles.

The observation of distinct rhombohedral peaks at a temperature below T_m for the samples of 0.92PMN–0.08PT and 0.9PMN–0.2PT in Figure 5-17, lends support to those who have suggested that the temperature T_f, at which the nano-polar regions become frozen so that remanent polarization is observed, should be used as the parameter to define the onset of the rhombohedral phase transformation [68]. T_f values of -43 °C, 18 °C and 77 °C, are published in the literature for the compositions of PMN [74], 0.9PMN-0.1PT [116] and 0.75PMN-0.25PT [42], respectively. Interpolating between these data gives the T_f values of 10 and 73 °C, which are listed in Table 5-2 for the present compositions of PMN-0.08PT and PMN-0.2PT. It is significant to note that these interpolated values for the PMN-PT samples lie within the composition ranges in Table 5-3, within which profile broadening associated with the onset of the rhombohedral phase was observed for the respective compositions. These values of T_f have thus been plotted in Figure 5-20 to indicate the temperatures at which rhombohedral structure forms on cooling. It is obviously necessary to obtain values of T_f at PT compositions between

0.20PT and 0.30PT, to determine the form of the plot as it approaches and intersects the morphotropic phase boundary.

As shown in Figure 5-20, the present T_α results for the higher PT compositions of 0.30 and 0.35, which display piezoelectric properties, fall very closely on the T_C plot, which has a slightly lower slope in this composition range. The respective T_α values fall within the temperature ranges (see Table 5-3) for the onset of the cubic-tetragonal phase transformation, based on the observed changes in profile shape. These observations confirm that the T_C plot represents the phase boundary between the cubic and tetragonal phases.

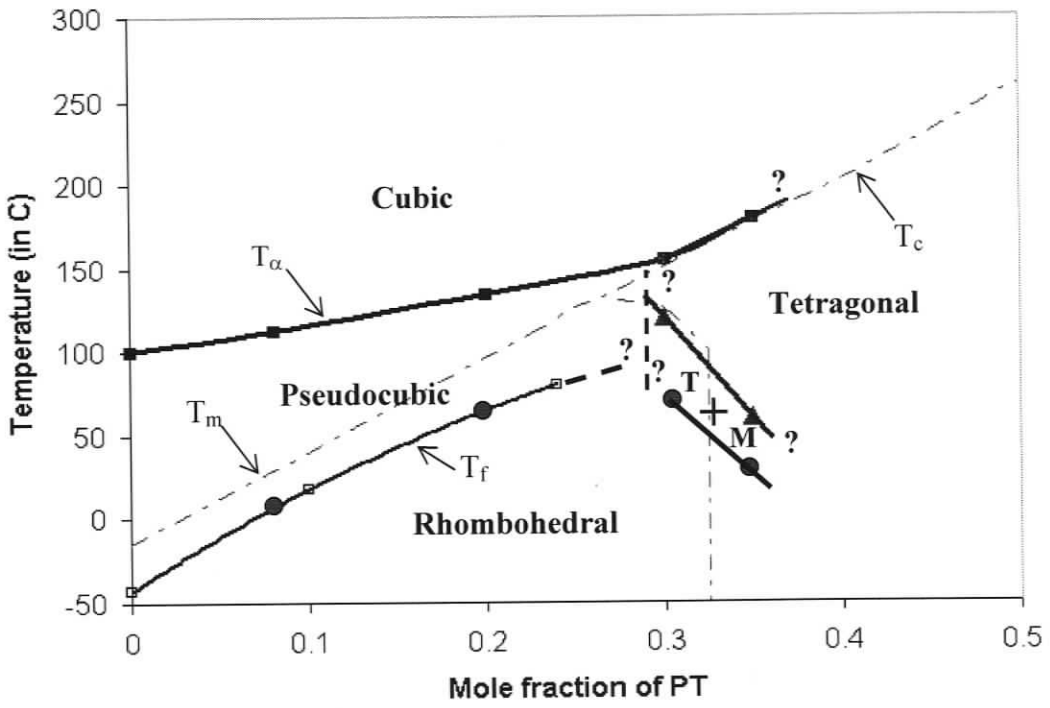

Figure 5-20 Structural phases and dielectric transitions in PMN-PT ceramic system [67]

The morphotropic boundary between the tetragonal and the rhombohedral phases is often shown as a vertical cut off, at a composition of x = 0.3 [63], or x = 0.35 [109]. However, the profile shape results in Table 5-3 show that the tetragonal phase breaks down to an intermediate monoclinic phase at temperatures in the ranges of 60-90 and RT – 40 °C, respectively, for the compositions PMN-0.3PT and PMN-0.35PT. When these results are plotted on Figure 5-20, they again fall closely on the boundary between the cubic and tetragonal phases suggested by Choi et al. [67] which has a negative slope, in contrast to the temperature independent results of Noblanc et al. [68] (see Figure 2-36). The present results are also confirmed by recent broadband brillouin scattering measurements [116], which indicate that this phase boundary has a distinct negative slope, so that small amounts of the tetragonal phase may transform to the rhombohedral phase even at compositions beyond 0.35PT. The recent phase diagram of Noheda et al. [83] (see Figure 2-37) also shows a negative slope to the boundary between the tetragonal phase and the intermediate monoclinic phase, and their boundary has been used in the subsequent phase diagrams suggested by Gehring et al. [86] and Xu et al. [34], which were shown earlier in Figures 2-38 and 2-39.

The unique finding of the profile change results in Table 5-3 relates to the temperatures of the transformation of the intermediate monoclinic phase to the stable low temperature rhombohedral phase. When these values are plotted on the diagram in Figure 5-20, the boundary between these two phases is seen to be a line, with a negative slope, that is parallel to the transformation line between the tetragonal and monoclinic phases.

Although the low temperature rhombohedral phase is continuous with the rhombohedral phase that forms from the pseudocubic phase at relaxor compositions, the boundary between the monoclinic phase and the pseudocubic phase at higher temperatures, which is shown as a dotted vertical line in Figure 5-20, can only be determined with precision by examining a number of PMN-PT composition in the range 0.25-0.30 PT. Similarly, the morphotropic phase boundaries between the tetragonal phase and the intermediate monoclinic phase, and the tetragonal phase and the low temperature rhombohedral phase, must be determined by examining a number of PMN-PT compositions in the range 0.35–0.45 PT.

The region of the diagram between the T_α and T_f plots in Figure 5-20 is labeled "pseudocubic", but in fact this is a two-phase region in which increasing amounts of randomly oriented nano-polar regions are formed, and increase in size, as the temperature is lowered. If the line T_m has any structural significance for relaxor compositions of $\leq$ 0.3PT, it can thus be associated with the temperature at which the nano-polar regions begin to grow in size, and interact with each other, as proposed in the relaxor model of Glazanov and Bell [56, 58]. The region below the T_f plot is labeled "rhombohedral", but a two-phase region (of uncertain width) composed of undecomposed pseudocubic structure and increasing amounts of the rhombohedral phase, exists just below the T_f plot, because of the athermal nature of this displacive transformation. The width of this two phase region can be established by investigating line profile changes over narrow ranges of temperature.

Similarly, there should also be a narrow two-phase region below the T_C plot, in which the cubic and tetragonal phase exist together, and two phase regions may also be determined at temperatures below the boundaries between the tetragonal and monoclinic phase, and between the monoclinic and rhombohedral phase, by a careful (and time consuming) study of peak splitting in a number of different diffraction profiles in the composition range between 0.30 and 0.4.5 PT. Hence, the entire range of compositions from PMN to 0.45PT needs to be examined, before a complete phase diagram can be obtained for the PMN-PT ceramic system. The present experimental work has defined the temperature dependence of the boundary between the monoclinic and the rhombohedral phase in the region of the morphotropic phase boundary and that the study of diffraction profiles over narrow ranges of temperature is an effective method for investigating displacive phase transformations in ceramic systems.

5.4. Electric Field Induced Fatigue

5.4.1. Soft Piezoelectric PZT Ceramics

Cracks introduced by a Vickers diamond hardness indenter in BM532 (Navy-Type VI) PZT are illustrated by the micrograph in Figure 5-21. Sharp cracks emanate from the corners of the diamond indent and propagate in a direction normal to the applied field, but no crack growth occurs from the corners that are aligned parallel to the field. The sharpness and linearity of the cracks indicate that they are transgranular, but the presence of any surrounding damaged material, of the type observed by Shieh et al. [104] could not be resolved at the relatively low magnification (of 100 X) available in the light microscope. The total length of these cracks, measured as the sum of the two cracks emanating from opposite corners, varied from 190 and 215 μm.

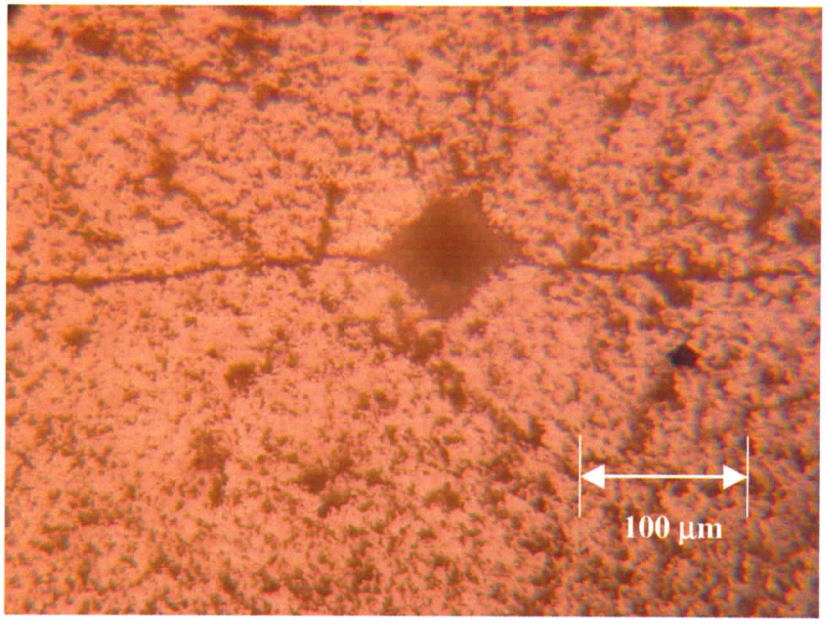

Figure 5-21 Indentation cracks in BM532

The crack growth observed in samples of BM532 at different peak to peak fields between 0.9 and 2.0 x E_C, is plotted against the number of applied field cycles in Figure 5-22. The cracks grow to a common size after a relatively few cycles of the applied field and then show very little, or no, subsequent growth. This result is contrary to the previous finding of Cao and Evans [101], that crack growth at electric fields E >E_C conform to steady state condition, in which the growth rate is independent of the crack length. It is consistent, however, with the findings Lynch et al. [102], who report that existing cracks in PLZT grow rapidly to a length of the order of the separation between the two electrodes when exposed to cyclic fields of 1.2-2.0 x E_C. The present results are also consistent with the findings of Shieh et al. [104] who observed crack arrest in PZT, after defined numbers of electric field cycles, the magnitude of which depended on the amplitude of the applied field. The limiting size of the cracks is a combined function of the specimen-electrode

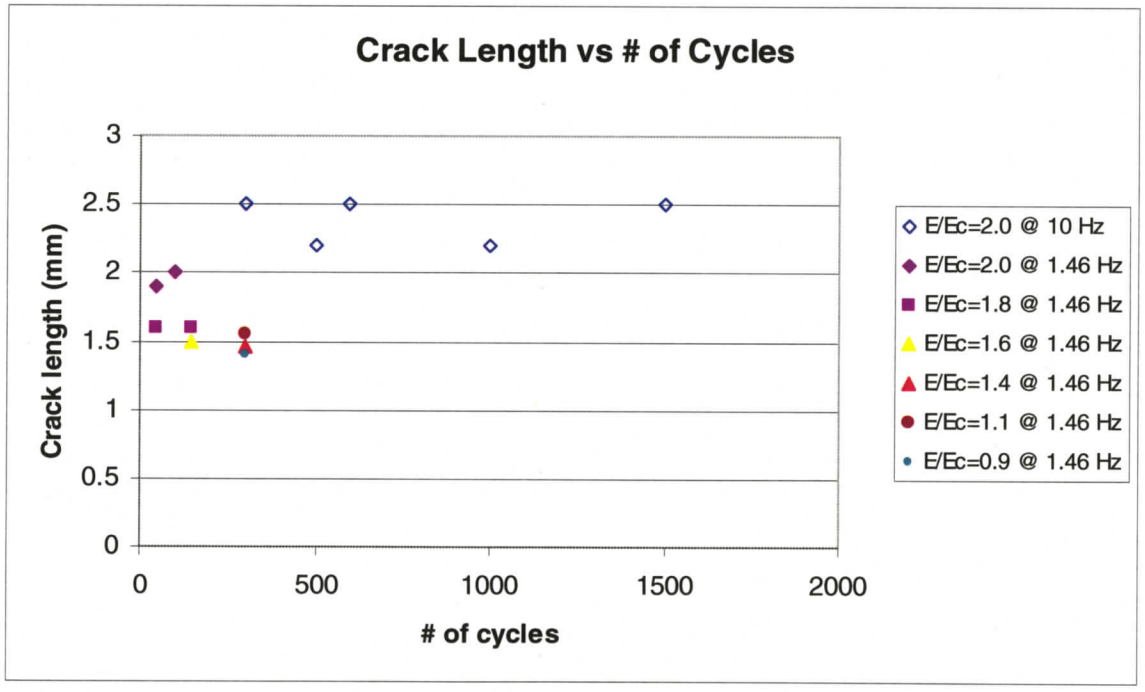

Figure 5-22 Crack length vs. number of cycles, for applied fields of 0.9-2.0 E_C (BM532)

geometry and possible toughening within the material, for example, by the formation of microcracks oriented parallel to the applied field, which would blunt the tips of the growing crack aligned normal to the field [102]. The results in Figure 5-22 also show that, while others have reported that there is very little frequency dependence of crack growth in the range of 1.5-5.0 Hz [102], for a given number of cycles at a common field of 2.0 x E_C, the increase in crack length at a frequency of 10 Hz is slightly greater than that observed at a frequency of 1.46 Hz.

The effect of peak-to-peak field intensity on crack growth, at a common frequency of 1.46 Hz, is shown in Figure 5-23. A small, but progressive, increase in crack length was observed at increasing fields over the range from 0.9-1.8 x E_C, while a distinct increase in crack length occurred when the reduced field was increased to 2.0 x E_C. This behaviour is

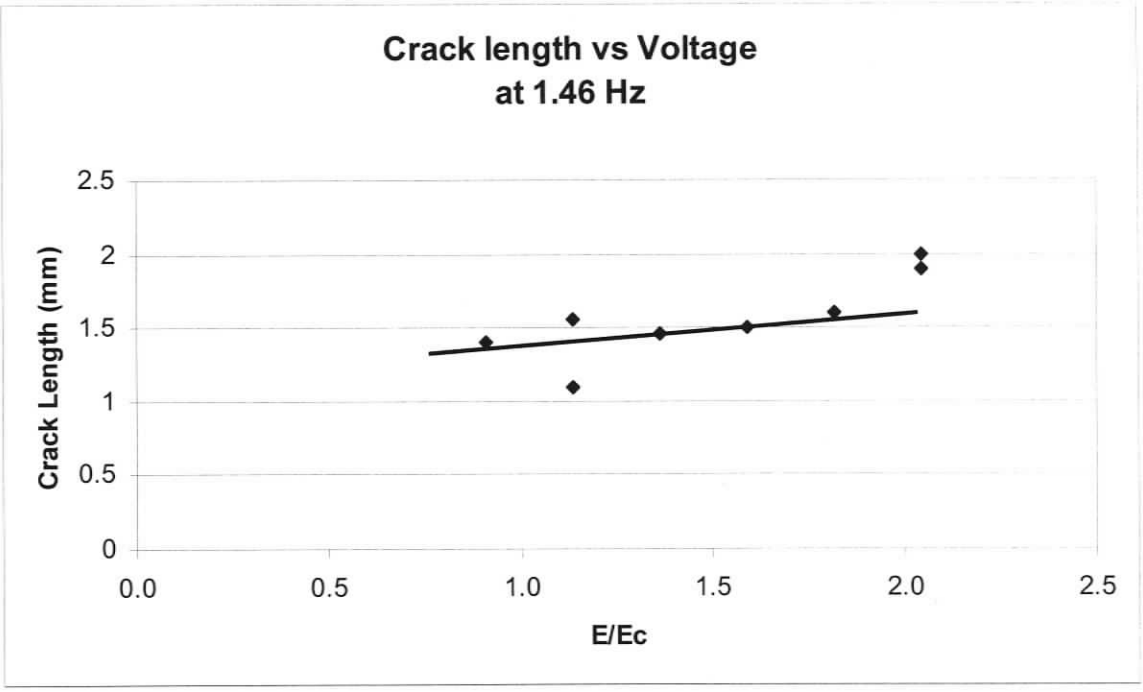

Figure 5-23 Crack length vs. applied field at a frequency of 1.46 Hz

analogous to the exponential increase in crack growth rate observed by Cao and Evans [101] in PLZT at reduced fields between 2.0-3.0 x E_C and is also consistent with the qualitative dependence of crack growth rate on field amplitude reported by Shieh et al. [104]. A possible explanation of this effect is that low electric fields simply extend existing transgranular cracks induced by the initial mechanical loading until they are blunted by microcracks, or other local deformation, while higher fields can provide additional electric stresses to drive the crack through damaged regions generated ahead of the tip. However, it has been reported by Shieh et al. [104], that further high magnification electron microscopy examination (that is beyond the scope of the present project) is required to clarify the electro-mechanical source of the fatigue cracking and the various mechanisms that can cause crack arrest in these piezoelectrics.

5.4.2. Soft Piezoelectric PMN-PT Ceramics

Cracks introduced by a Vickers diamond hardness indenter in the soft piezoelectric PMN-0.3PT ceramics are illustrated by the light micrograph in Figure 5-24. The sharp cracks emanate from the corners of the indent and propagate in directions parallel to the diagonals. The total length of these transgranular cracks, measured as the sum of the two cracks emanating from opposite corners, varied from 200 to 300 μm. In spite of the fact that these cracks are considerably longer than the largest cracks formed in the BM532 PZT sample, many of the PMN-0.30PT specimens showed cracks emanating from only one corner of the indent, while other samples showed no cracks after indentation.

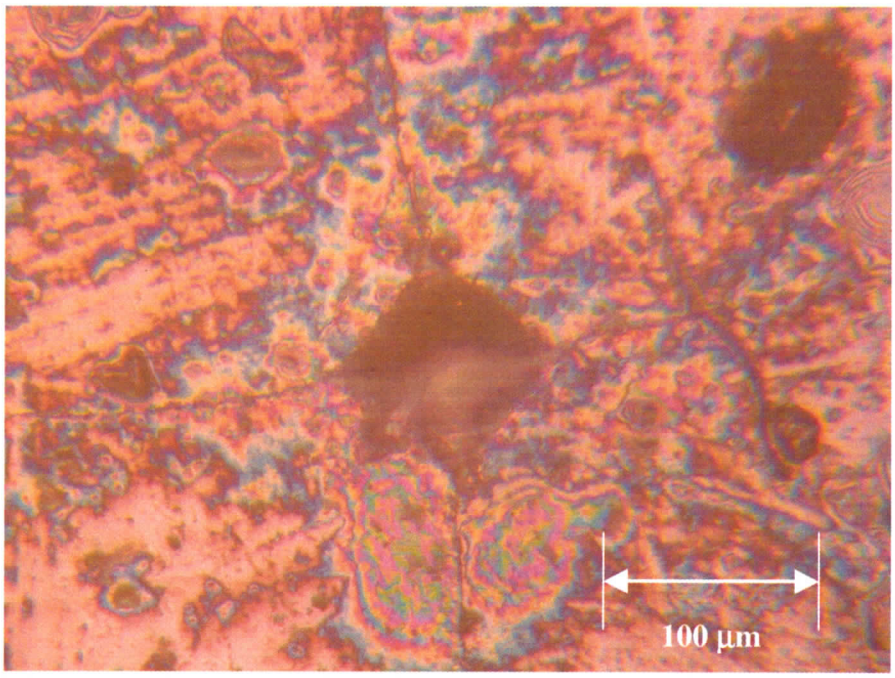

Figure 5-24 Indentation cracks in PMN–0.3PT

The extension of cracks subjected to various reduced electric fields in the range 2.18-5.60 x E_C, at a common frequency of 5 Hz, is shown in Figure 5-25. It is evident that cracks of different initial lengths all extend to a common limiting value, but the progress of the crack extension varies with the magnitude of the applied field. In the sample exposed to the lowest reduced field of 2.18 x E_C, no extension was observed until the field was imposed for 2000 cycles, after which the crack extended directly to a length of 0.49 mm. At an intermediate reduced field of 3.91 x E_C, the crack showed a series of discrete intermediate extensions before achieving the same length of 0.49 mm after 100 cycles. At the highest applied reduced field of 5.60 x E_C, the crack again displayed an intermediate step and then increased in length to 0.49 mm after only 10 cycles. Increasing the

magnitude of the applied field thus achieved the common terminal length in a reduced number of cycles.

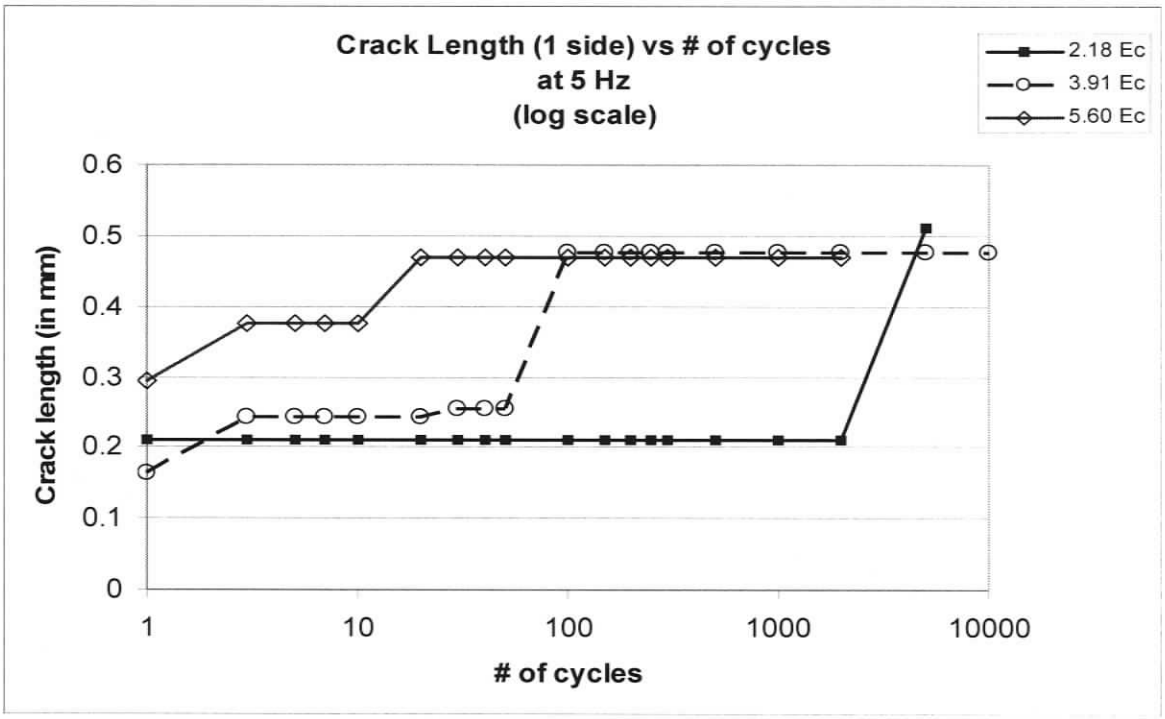

Figure 5-25 Crack length vs. number of cycles, for E = 2.18-5.60 x E_C (PMN-0.3PT)

The concept of a common limiting crack extension was further examined by plotting the terminal values of crack extension obtained (at various frequencies) against the applied reduced field over the entire experimental range from 0.64-5.60 x E_C, to obtain the plot shown in Figure 5-25. The individual extensions observed on each side of the indent are displayed in this plot and show that there are measurable differences in crack growth in the two opposing directions, both of which are normal to the applied field. At reduced fields in the region of 0.64-1.07 x E_C the terminal crack length lies between 0.2-0.3 mm, which is the range of values for the pre-existing cracks; i.e. there has been no crack growth. When the reduced field was increased to 1.13 x E_C, the crack on one side of the

indent increased, but no growth was observed on the crack emanating from the opposite corner of the indent. The critical value of reduced field for inducing crack growth in this material is thus close to 1.10 x E_C. When the reduced field was increased into the range 1.8-5.7 x E_C, the terminal lengths of cracks on either side of the indent all lie between 0.41-0.52 mm, while the individual crack extensions conform to an average value of 0.46,

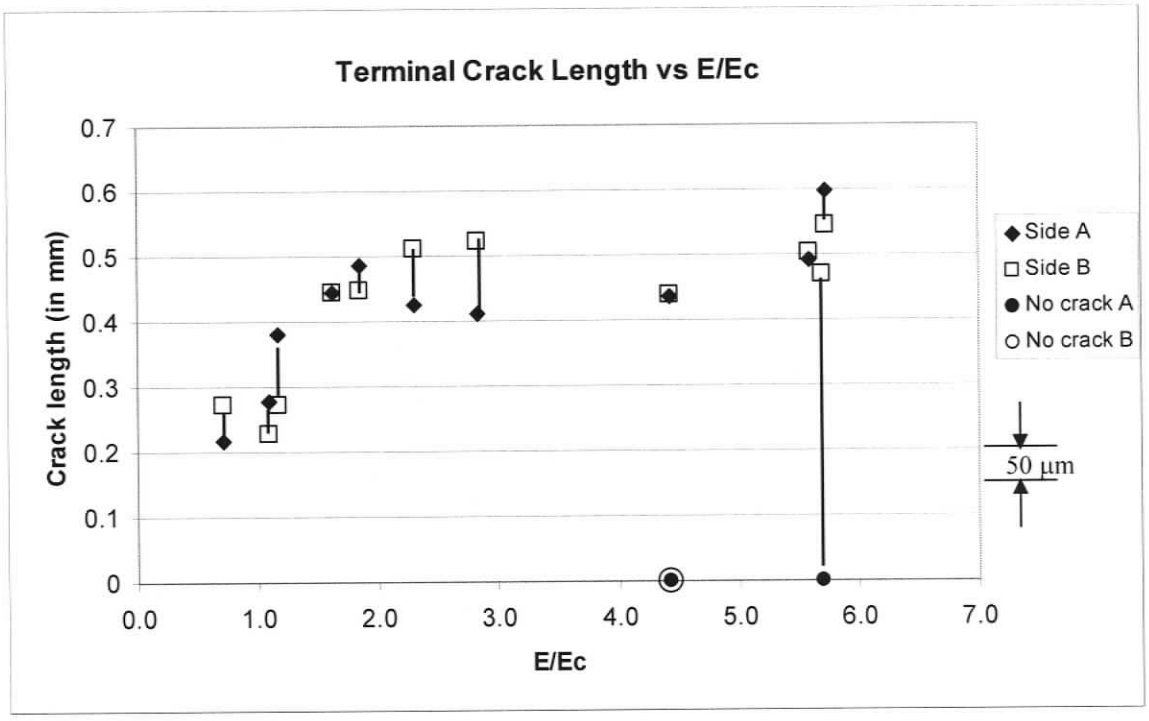

Figure 5-26 Terminal crack length vs. reduced field (PMN-0.3PT)

within the limit of experimental error of ± 50 µm. This common terminal crack extension is consistent with the limiting crack lengths obtained for the samples referred to in Figure 5-25, which were all subjected to the same range of applied reduced fields. These results also confirm the previous finding of a limiting crack extension length for BM532 specimens, when subjected to applied reduced fields in the range 0.9-2.0, as shown in Figure 2-22, and agree with the observations of Lynch et al. [102] and Shieh et al. [104],

that pre-cracks in PLZT grow rapidly to a common length when exposed to cyclic fields of 1.2-2.0 x E_C. The common overall crack length of 0.92 mm (2 x 0.46 mm) observed in the present results is approximately 0.8 times the separation between the two electrodes, which also concurs with the results obtained by Lynch et al. [102]. However, none of the present results concur with the earlier finding of Cao and Evans [101] that crack growth in PZT at electric fields greater than E_C conform to a steady state condition, in which the growth rate is independent of the crack length.

The results in Figure 5-26 also show that samples which had no crack at either corner of the diamond indentation did not generate new cracks when subjected to an applied reduced field of 4.44 x E_C for a period of 6000 cycles. Another sample that had a crack at only one corner of the diamond indent showed growth of this crack only to a limiting extension of 0.47 mm after 6000 cycles in a reduced field of 5.7 x E_C, but an additional crack was not generated in the opposite corner of the indent as a result of this treatment. It is thus concluded that applied reduced electric fields up 5.7 x E_C are not effective for generating new cracks in indented specimens of PMN-0.30PT that are initially crack-free.

5.4.3. Hard Piezoelectric PZT Ceramics

Cracks introduced by a Vickers diamond hardness indenter in the hard piezoelectrics BM200 and BM800 are illustrated by the micrographs in Figure 5-27. The indenting operation generated single cracks (emanating from only one corner of the indent) and double cracks (emanating from both opposite corners). Both types of crack appeared to be transgranular in nature and extended to lengths of 50-148 μm in directions parallel to

one or other of the diagonals of the indent. The incidence of shorter crack lengths compared to those obtained under the same loading conditions in the specimens of BM532 and PMN-0.3PT, is considered to be a direct consequence of the greater mechanical hardness of the BM200 and BM800 ceramics.

Microscopic examination of sets of eight samples of both BM200 and BM800, at a magnification of 160X, showed no measurable increase in the length of cracks oriented

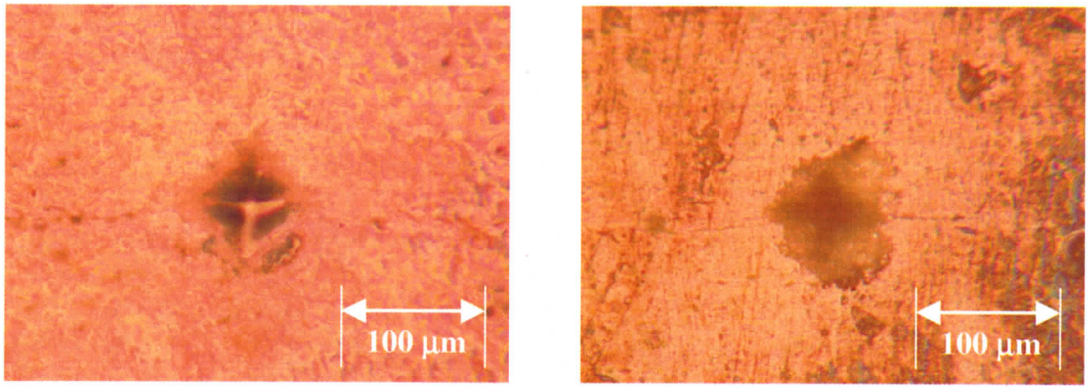

Figure 5-27 Indentation cracks in a) BM200 and b) BM800

normal to the applied field, after successive applications of electric fields with progressively increasing strengths up to an available maximum of 3.15 MV/m, at a common frequency of 5 Hz. Since the coercive fields of BM200 and BM800 shown above in Figure 5-7 are of the order of 1.9 MV/m, the maximum reduced field of 1.7 is only slightly less than the reduced field of 1.9 that caused considerable crack growth in specimens of the PZT soft piezoelectric BM532. The absence of crack growth in these hard piezoelectrics is thus attributed to their relatively low d_{33} piezoelectric charge coefficients.

To investigate a simple non-destructive method for detecting, and/or monitoring, the growth of fine cracks that may not be visible in a light microscope at low magnification, the impedance spectra of the hard piezoelectric specimens were measured near their lowest frequency resonance i.e. in the LTE mode as shown previously in Figure 2-13. The results of measurements made on both non-indented samples and indented samples, before and after exposure to a selected numbers of low frequency field sweeps are shown in Figure 5-28.

The resonance frequency of BM200 samples, measured prior to indentation with the Vickers diamond, was 146 kHz. This frequency was decreased to 143-144 kHz in indented samples that contained a single clearly resolved crack emanating from only one corner of the diamond indent. A smaller reduction in resonance frequency, from 146 to 145 kHz, was observed in samples with double narrow cracks emanating from opposite corners of the diamond indent, that were only made visible in the microscope after the sample surface was treated with a blue penetrating dye. The resonance frequency of 158 kHz, measured prior to indentation in BM800 samples, showed a distinct drop to 148 kHz in samples that contained a single well-resolved crack emanating from only one corner of the diamond indent. Once again, BM800 samples with narrow double cracks showed a smaller decrease in resonance frequency, of the order of 1 kHz.

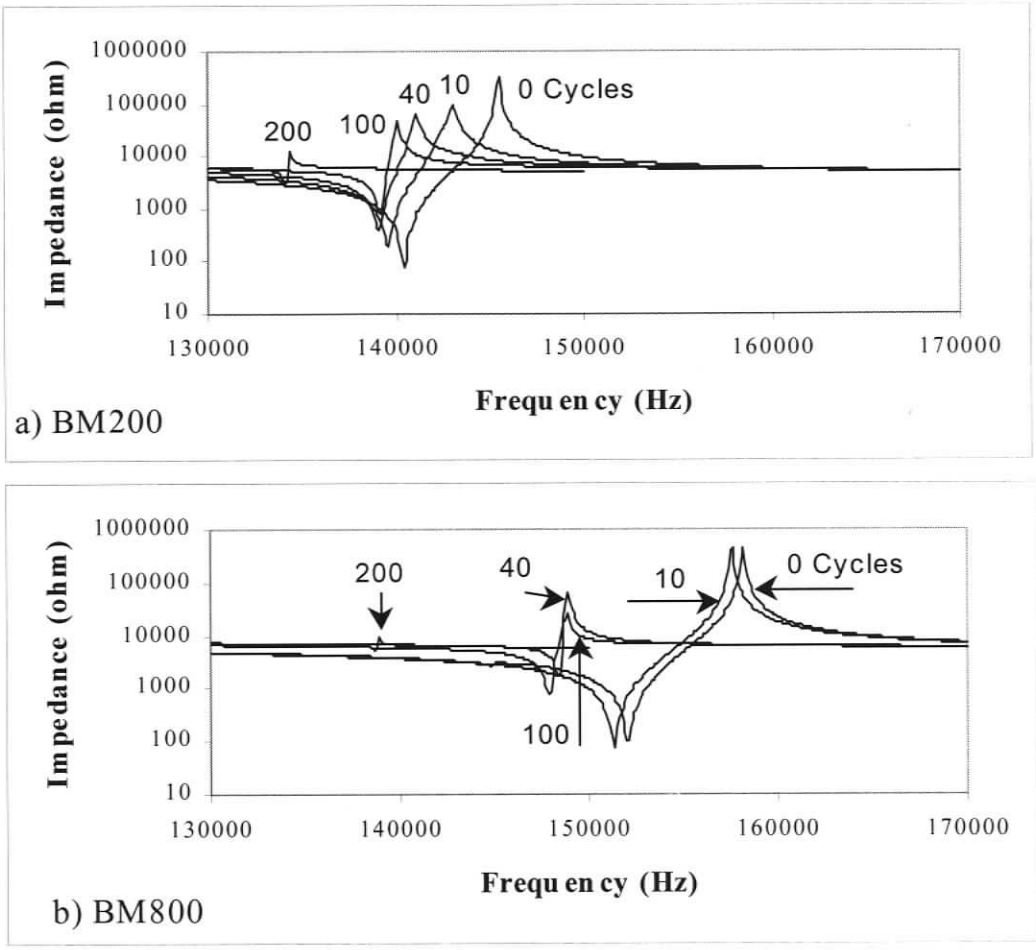

Figure 5-28 LTE mode impedance spectra for indented and electrically exposed samples of a) BM200 and b) BM800

No apparent correlation was observed, however, between the length of the cracks and the measured decrease in resonance frequency, for both sets of hard piezoelectric ceramics. It was thus concluded that the observed decreases in resonance frequency are associated with the relative width, or perhaps the depth, of the cracks, as opposed to their lengths. These aspects would be worth exploring in future work on directed at the development of a non-destructive test for defects in piezoelectric ceramics.

5.4.4. Relaxor PMN-PT Ceramics

The microstructure of a Vickers diamond indent in a specimen of the relaxor ferroelectric PMN-0.08PT, at a magnification of 100X, is shown in Figure 5-29. In contrast to the cracks observed in diamond indents made under identical conditions in the related composition PMN-0.3PT (Figure 5-24), and in the soft piezoelectric BM532 (Figure 5-21), no sharp transgranular cracks were observed to emanate from the corners of the diamond indent in the PMN-0.08PT relaxor ceramic. However, grains adjacent to the flat sides of the diamond indent were displaced above the polished surface of the specimen cracks, like the grains of sand that are displaced at the sides of a foot while walking along

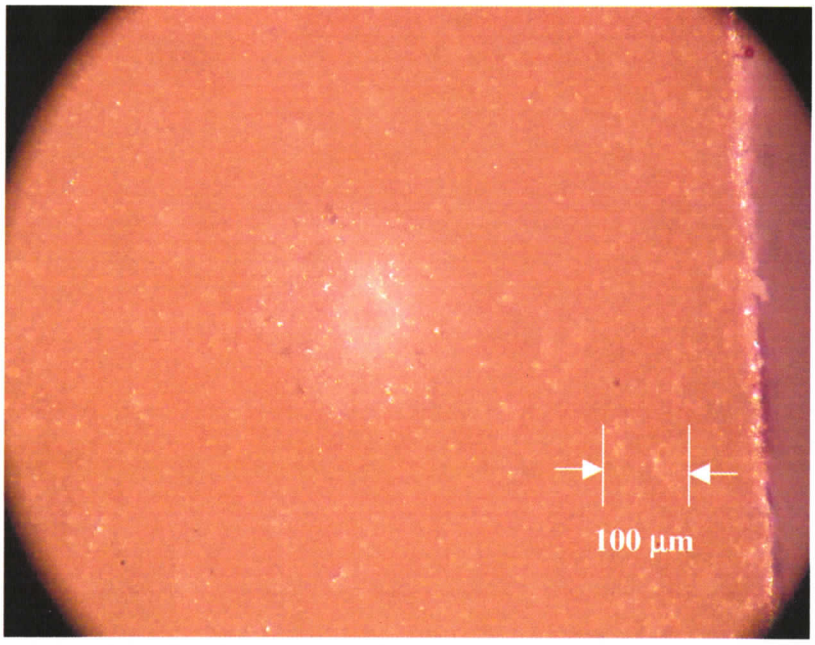

Figure 5-29 Indentation in PMN-0.08PT prior to applying cyclic field

the damp sand at the seashore. This deformation is similar to that reported earlier by Raynes et al. [105] in samples of PMN containing an unspecified small amount of PT. The nature of the deformation in Figure 5-29 is indicative of intergranular cracking, in which the direction of a crack meanders around a grain, rather than following a direction parallel to the diagonal of the indent.

No growth of the existing intergranular cracks occurred, nor were any new transgranular or intergranular cracks observed in the sample of PMN-0.08PT, after the application of 104 cycles of an electric field of 3.1 MV/m, as shown by the micrograph in Figure 5-30. This figure does indicate a general tendency for the intergranular cracks to radiate out from the indent, but this effect is regarded as an existing condition which was highlighted by the penetration of the insulating oil that was used for the field application experiments. The absence of intergranular crack growth was not surprising, because the extension of

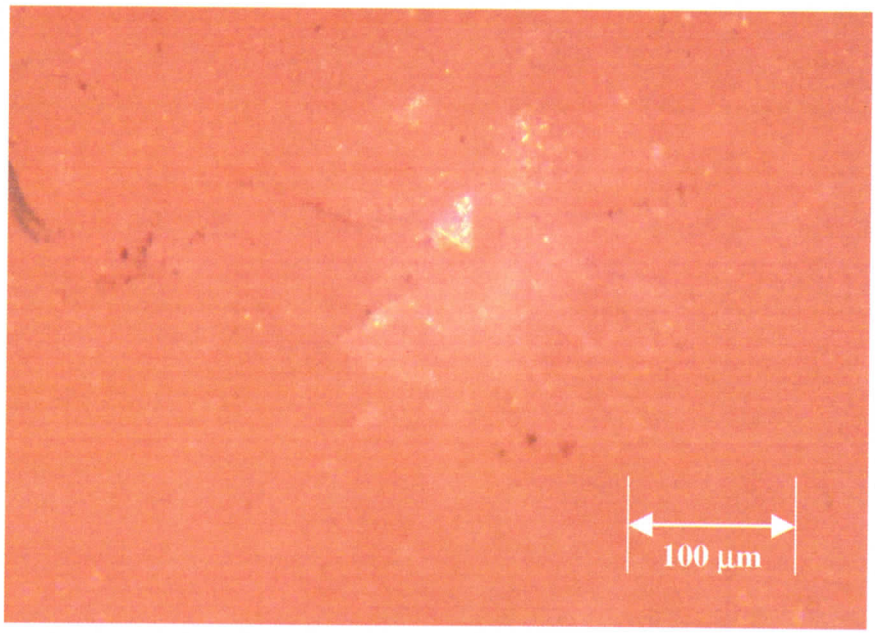

Figure 5-30 Indentation in PMN-0.08PT after 10,000 cycles

these cracks around the grains follows an indistinct path with respect to the orientation of the surface electrodes. In fact the introduction of microcracks is one of the methods used to toughen ceramics [7].

In a further attempt to introduce intergranular cracks, samples of PMN-0.08PT were indented with a Knoop diamond, which has a chisel shaped point that creates an elongated indent, with a pair of very acute angle corners and a pair of obtuse angle corners. The microstructure of a Knoop indent in the sample of PMN-0.08PT is shown in Figure 5-31. There is no evidence of transgranular cracking, even at the sharp end of the indent, but intergranular cracks were clearly resolved in the region of the specimen adjacent to the flat side of the indent. In many cases these cracks completely surround a grain and the unresolved dark regions indicate that entire grains have been ejected from the surface.

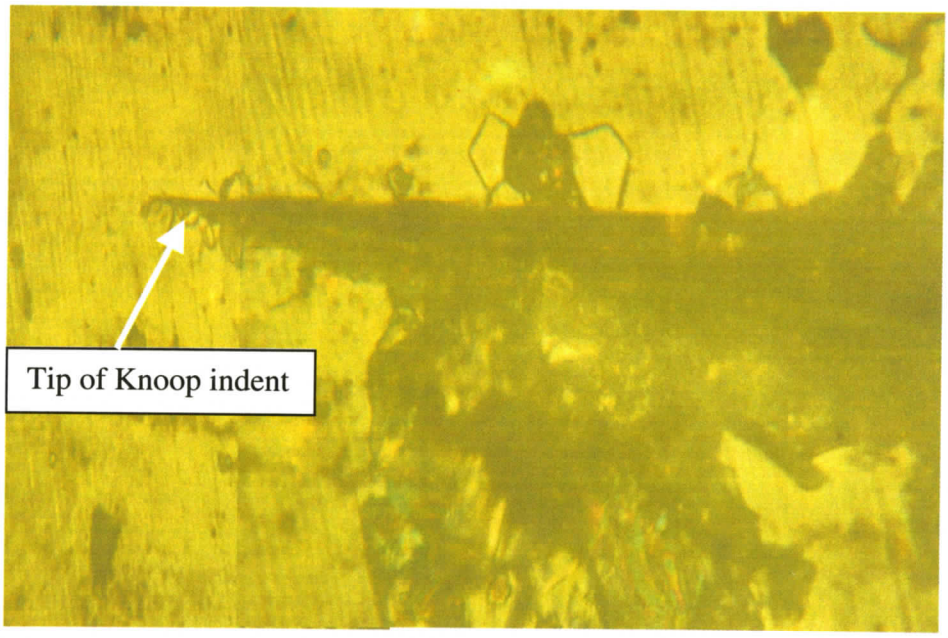

Figure 5-31 Knoop indent in PMN-0.08PT ceramic specimen (400X)

5.4.5. Discussion of Crack Growth Results

For each material subjected to the cyclic electric fields (BM 532, BM620, BM660, BM200 and BM 800), a total 16 specimens were polished. From these, 14 specimens were indented (with the two non-indented specimens remaining as reference specimens).

The experiments on a commercial grade of a soft piezoelectric BM532 PZT confirm that electric fields in excess of the coercive field can extend pre-existing cracks up to a length related to the electrode separation and also indicate that cyclic fields in excess of 2.0 x E_C can cause excessive crack growth which could result in accelerated electric breakdown. However, since the recommended maximum peak-to-peak field used in commercial actuator applications is typically about one-half E_C [6], this potentially deleterious effect is unlikely to be experienced in normal practice.

The results obtained for the PMN-0.30PT, where the cracks grow to a common length, but grow by different increments depending on the magnitude of the applied field, are analogous to the effect in increasing the applied load in a mechanical fatigue test. It is thus likely that the multiple stages of crack extension are caused by microstructural features that can act as crack stoppers, so that higher electric fields, or longer cycles, are required to achieve the common limiting extension. The analogous behaviour of these results to mechanical fatigue also suggests that there should be a level of applied reduced electric field below which pre-existing cracks will not grow to the limiting extension over finite cycling times.

The d_{33} piezoelectric charge coefficients of BM200 and BM800 are of the order of 225 pC/N, which is about one third of the d_{33} value of the soft PZT BM532, which is of the order of 590 pC/N [6]. Since the induced piezoelectric strain is directly proportional the applied field, it means that in order to obtain the same degree of strain, the electric field applied to the hard PZT piezoelectrics such as BM200 and BM800 must be about three times the field applied to soft piezoelectrics such as BM532 and PMN-0.3PT. The BM200 and BM800 ceramics are thus subjected to considerably smaller electric stress, at any given applied field. However, obtaining greater piezoelectric strains, by the use of higher electric fields is not practical in the present context, because the maximum field available for the present experiments was 80% of the dielectric breakdown field of PZT ceramics [25, 110, 120]. On the other hand, since the use of PZT as sensors and actuators will inevitably involve fields well below 3 MV/m, it is safe to consider that hard piezoelectric ceramics such as BM200 and BM800 are effectively resistant to electric-field-induced crack growth for most, if not all, commercial applications.

The different types of cracks that form by indentation in the ceramics PMN-0.3PT and PMN-0.08PT are considered to be a consequence of their different room temperature structures. PMN-0.3PT has a rhombohedral structure which will likely have a cleavage plane that will create a transgranular crack. The PMN-0.08PT ceramic has a pseudocubic structure that is constrained by the nano-polar rhombohedral regions that cause internal stresses. The relief of these stresses by the diamond indentation is associated with the creation of free surfaces, so that the cracks are intergranular and whole grains can be displaced. The fracture of these ceramics under the imposed load of the Vickers or Knoop diamonds is thus similar to the fracture of tempered glass, while the cracks introduced in

the rhombohedral ceramics are similar in form to the brittle fracture of glass, or the cleavage of brittle ceramics. However, from a practical point of view, the relaxor PMN-PT compositions can be considered to be resistant to field induced fatigue, since no new cracks were introduced at the levels of the electric fields applied to industrial actuators composed of these materials. On the other hand, these ceramics should not be used in high mechanical, or shock, load situations, where fracture by the relief of residual stresses can occur.

6.0 Summary and Conclusions

1. Soft piezoelectrics (such as BM532 and PMN-0.3PT are characterized by symmetrical polarization-field hysteresis loops, while field-biased hard piezoelectrics (such as BM200 and BM800) have asymmetrical hysteresis loops, which generate inflated values of the coercive field E_C (1.88-1.94 MV/m).
2. An effective coercive field E_C' has been defined for internally biased PZT piezoelectrics by subtracting the internal field E_i from the measured E_C, to enable a meaningful comparison to be made between the dielectric properties of these ceramics and the coercive fields of the soft unbiased piezoelectrics.
3. The temperature T_α at which relaxor ferroelectrics display a sharp change in coefficient of thermal expansion can be identified with the onset of the second order phase transformation from the high temperature cubic perovskite phase to a lower temperature pseudocubic structure, which contains stable nano-polar rhombohedral regions, with random orientations.
4. The onset of the first order phase transformation from the pseudocubic phase to a rhombohedral structure occurs at the temperature T_f, (or T_d), which is associated with the freezing of the rhombohedral polar regions on cooling, or the onset of de-poling on heating.
5. The rhombohedral structure is regarded as the lowest temperature equilibrium phase in relaxor compositions of PMN-PT, but a metastable elastically constrained cubic structure is observed in PMN-0.1PT at room temperature and in PMN at cryogenic temperatures.

6. The mechanism of the relaxor transition in PMN-PT is considered to be as follows: Nano-polar regions that are observed at temperatures just below the Burns temperature T_D, are in a continual state of formation and re-solution and have random orientations; on cooling through the temperature T_α, the crystal lattice becomes stiffened and the randomly oriented nano-polar regions become stable, but can be re-oriented by an applied electric field; the number of nano-polar regions increase to a maximum on cooling to the temperature T_m, below which the size of the regions, and the interactions between them, increases on cooling; on further cooling below the temperature T_f, the orientation of the nano-regions is frozen, to give a net polarization, and a stable rhombohedral structure can form by a first order phase transition.
7. The sequence of structures that occur on cooling PMN-PT compositions in the region of the morphotropic phase boundary is: cubic – tetragonal – monoclinic (or orthorhombic) – rhombohedral.
8. The athermal displacive phase transformations that occur in the PMN-PT ceramic system occur over ranges of temperature in which increasing amounts of the new phase form on cooling, so the transformation boundaries between the different structures are really narrow two-phase regions, that can be effectively investigated by the study of diffraction profiles over narrow ranges of temperature.
9. Pre-existing transgranular cracks in the room temperature rhombohedral phase in soft piezoelectrics (such as BM532 and PMN-0.3PT) can propagate after relatively few cycles (less than 10) of low frequency (1.5-10 Hz) applied electric fields, with amplitudes above a threshold of 0.9-1.1 x E_C.

10. With increasing field amplitude, up to the safe limit to avoid dielectric breakdown (2-5 x E_C), transgranular cracks in soft piezoelectrics can grow up to a limited length, which is of the order of the separation of the electrodes, but fresh cracks are not initiated, even at the maximum safe permitted field.
11. Growth of pre-existing transgranular cracks in the room temperature rhombohedral phase in field-biased hard piezoelectrics (such as BM200 and BM800) cannot be stimulated by the action of low frequency electric fields, with amplitudes up to the safe limit to avoid dielectric breakdown (3.15 MV/m).
12. Shifts in resonance frequencies, with concurrent changes in the difference between maximum and minimum impedance can, in principle, be used to detect and/or monitor crack growth in applied electric fields, at levels below the limit of detection by optical inspection (e.g. in hard piezoelectrics).
13. Vickers diamond indents generate intergranular (as opposed to transgranular) cracks, in the room temperature metastable cubic structure of relaxors (such as PMN-0.1PT).
14. Local surface disintegration (such as grain lifting) observed in the vicinity of the intergranular cracks in the relaxor PMN-0.1PT is attributed to the relief of internal stresses in the pseudocubic crystal lattice, which is constrained by the enclosed nano-polar rhombohedral regions.
15. Growth of pre-existing intergranular cracks in the cubic structure of this relaxor cannot be simulated by the action of low frequency electric fields, with amplitudes up to the safe limit to avoid dielectric breakdown (3.15 MV/m).

16. Although the specified maximum working field for soft piezoelectric is less than half of the threshold field for stimulating crack growth, and crack growth is not observed up to the maximum safe fields in hard piezoelectrics and in relaxors, close attention must be still given to testing for microstructural defects, that can act as crack formers, during the manufacture of these important engineering ceramics.

7.0 Future work

In order for an actuator to be used successfully for engineering applications such as a piston for an electric brake caliper, it is necessary to determine its mechanical properties over the operational ranges of temperature and applied voltages. Since such devices will be operating in the elastic region, it is essential to know the temperature dependence of Young's modulus, in addition to the fracture strength and fracture toughness of the actuator material. Further, since it has been shown that the mechanical integrity of particular dielectric ceramics can break down in cyclic electric fields, the nature and extent of crack growth in all industrial grades of PZT needs to be investigated.

7.1. Effects of Cyclic Fields on a moderately hard PZT's

A significant gap in the knowledge of crack growth in low frequency electric fields occurs in PZT ceramics that have moderately hard piezoelectric properties. A PZT composition such as BM400 will be examined as a priority, followed by the remaining US Navy Types of PZT and other PMN-PT compositions between 0.1 and 0.3 mole fractions of PMN-PT.

7.2. Further investigation of PMN-PT Phase Diagram

Future work will involve X-ray measurements on the PMN-PT samples with compositions of 0.25, 0.28, 0.32 and 0.38 mole fractions of PT, to establish the precise phase transformations that occur in the region of the morphotropic phase boundary in this

system. A finer step scan resolution will be used in combination with smaller temperature increments, on cooling through the transformation temperature ranges. This will allow a more detailed determination of the structural phase diagram of the (1-x)PMN-xPT ceramic system.

7.3. Investigation of Structural Transformations in the Region of the Morphotropic Phase Boundary in the PZT Ceramic System

Recent discoveries have shown that an intermediate monoclinic phase, which forms between the high temperature cubic phase and the low temperature rhombohedral phase, is responsible for the exceptional piezoelectric properties of PZT compositions in the region of the morphotropic phase boundary [121, 122]. The temperatures at which this monoclinic phase forms, and then transforms to the rhombohedral phase, will be investigated by examining diffraction profile shapes of PZT compositions in the region of the MPB.

7.4. Investigation of PMN-PT Phase Diagram using a Calorimeter

7.4.1. Gibbs free energy

The Gibbs free energy (G) can be calculated from the polarization (P) using a relationship based on G(P). Plots of G vs. P at various temperatures below, at and above the Curie point should give an indication of the any structural phase transformations. The plots of G vs. P for PMN-PT should include temperatures in the region of T_{α}, which should confirm the results obtained using X-ray diffraction.

7.4.2. Locating Phase Transformations

A calorimeter could be used to investigate and confirm the phase transformations discovered in the PMN-PT system. The calorimeter would also allow the direct calculation of the Gibbs free energy at various temperatures.

7.5. Dielectric measurements using Labview

Since the cooling rate of the Blue-M furnace is very slow, it takes approximately 20-24 hours to collect capacitance values for a specimen. It is thus recommended that the thermocouple readings and the output for the capacitance meter be fed to a computer, via the Labview software program. This will allow a continuous recording of the temperature and capacitance, which should eliminate the human error involved in measuring and recording the readings. It should also be noted that as the dielectric measurements are made closer to room temperature, the slower the cooling of the furnace (and the longer the experiment) becomes. As well, the automation of the data collection will prevent the restarting of the experiment at an intermediate point, which then requires re-heating the specimen in order to take the remaining dielectric measurements the following day.

References

1. Setter, N. and Waser, R. (2000). Electroceramic Materials. *Acta Material*, Vol. 48, pp 151-178.

2. Takuro Ikeda, Fundamentals of Piezoelectricity. Oxford Science Publications, New York, 1996.

3. F. Jona and G. Shirane, Ferroelectric Crystals, Dover Publications, New York, 1993.

4. J. F. Nye, Physical Properties of Crystals – Their Representation by Tensors and Matrices. Oxford Science Publications-Oxford University Press, New York, 2004.

5. B. Jaffe, W.R. Cook and H. Jaffe. Piezoelectric Ceramics, Academic Press (1971).

6. Company Data Sheets. Sensor Technology Ltd. Collingwood, Ont. Canada. [www.sensortech.ca] (2005-09-31).

7. Y-M. Chiang, D.P. Birnie III, W.D. Kingery, Physical Ceramics: Principles for Ceramic Science and Engineering. John Wiley and Sons, New York, 1997.

8. C. Kittel, Introduction to Solid State Physics - 4th edition, John Wiley & Sons, New York, London, Sydney, Toronto, 1971, pp. 475−499.

9. M. H. Cohen (1951), Ferroelectricity vs. Antiferroelectricity in barium titanate. *Phys. Rev.* Vol. 84, 369.

10. R. Pepinsky (1955), *Proc. I.R.E.* Vol. 42, p. 1738.

11. Askland, D. R. (2001). The Science and Engineering of Materials, 4th edition. Boston, Mass., International Thompson Publishing.

12. W.J. Merz (1949), The Electric and Optical Behavior of BaTiO3 Single Domain Crystals. *Phys. Rev.* Vol. 76, p. 1221.

13. E. Fatuzzo and W.J. Merz, Ferroelectricity. Selected Topics in Solid State Physics, Vol. 7, John Wiley & Sons, Inc., New York, (Interscience Publishers Division), Editor E.P. Wohlfarth, 1967.

14. 2002 CODATA Recommended Values. Committee on Data for Science and Technology (CODATA), NIST, [http://physics.nist.gov/cuu/Constants/bibliography.html] Oct.16, 2005.

15. IEEE Standard on Piezoelectricity, IEEE Standard #176-1978. *Institute of Electrical and Electronics Engineers Inc.,* 345 East 47th St., New York, NY 10017.

16. Measurements of Piezoelectric Ceramics, *IRE Standards on Piezoelectric Ceramics; 1961, Proc. IRE*, pp. 1161-1169 (1961).

17. C.T. Dervos, C.D. Paraskevas, P.D. Skafidas and P. Vassiliou (2005), A Complex Permittivity Based Sensor for the Electrical Characterization of High-Voltage Transformer Oils. *Sensors*, Vol. 5, pp. 302-316.

18. F.T. Emery (2002), Power Factor Measurements on High Voltage Stator Bars 8t Stator Windings. *Conf. Rec. of the 2002 IEEE International Symposium on Electrical Insulation*, Boston, MA USA, (April 7-10, 2002), pp. 502-505.

19. S. Wang, Solid State Electronics. McGraw-Hill Book Co., New York, 1966.

20. Engineered Materials Handbook: Ceramics and Glasses-Vol. 4. ASM International, (1991), ISBN 0-87170-282-7.

21. G. L. Johnson (2001), Solid State Tesla Coil - Chapter 3: Lossy Capacitors.

22. Kaye and Laby (2004), Table of Physical and Chemical Constants – Online Edition. National Physical Laboratory, Teddington, Middlesex, United Kingdom, [http:// www.kayelaby.npl.co.uk/general_physics/2_6/2_6_5.html], Nov 2005.

23. E. C. Henry (1980). Ferroelectrics. Encyclopedia of Chemical Technology, 2nd Ed., Vol. 9, pp 1−25.

24. W. J. Merz (1953), Double Hysteresis Loop of $BaTiO_3$ at the Curie Point. *Phys. Rev*. Vol. 91, No. 3, pp. 513-517.

25. K. Carl and K.H. Hardtl (1978), Electrical after-effects in $Pb(Ti,Zr)O_3$ ceramics, *Ferroelectrics*, Vol.17, pp. 473−486.

26. James F. Shackelford, Introduction to Materials Science for Engineers, 4th Ed., Prentice Hall, New Jersey, 1996.

27. G.E. Dieter, Mechanical Metallurgy. 3rd Ed. McGraw-Hill Book Company, New York, 1986.

28. [http://www.efunda.com/materials/piezo/electronics/elec_impedance.cfm] , Oct 27, 2005.

29. W.G. Cady, Piezoelectricity: An Introduction to the Theory and Applications of Electromechanical Phenomena in Crystals. McGraw-Hill Book Co. New York, 1964, pp. 298.

30. IRE Standards on Piezoelectric Crystals: Determination of the Elastic, Piezoelectric and Dielectric Constants. *Proc. IRE*, Vol. 46, pp. 764-768, 1958.

31. Sung-Eek Park and Thomas R. Shrout, Ultrahigh strain and piezoelectric behavior in relaxor based ferroelectric single crystals. J. Appl. Phys., Vol. 82 (4), 15 August 1997, pp 1804 -1811.

32. V. Vargha, A. Gy. Pozsgay, P. Valentini (1999), Ferroelectric Liquid Crystal Polymers. *Periodica Polytechnica Ser. Chem. Eng.,* Vol. 43, No. 1, pp.17-33.

33. Cross, L.E., (1994), Relaxor Ferroelectrics: an Overview. *Ferroelectrics*, Vol. 151, pp. 305-320.

34. Guangyong Xu, D. Viehland, J.F. Li, P. M. Gehring, G. Shirane (2003), Evidence of decoupled lattice distortion and ferroelectric polarization in the relaxor system PMN-xPT. *Phys. Rev. B* Vol. 68, 212410 (2003).

35. E.V. Colla, E. Yu Koroleva, N.M. Okuneva, S.B. Vakhrushev (1992), Low-frequency dielectric response of PbMg1/3Nb2/3O3. J. Phys. Condens. Matter, Vol. 4, pp. 3671-3677.

36. Smolenskii, G. A. and Agranovskaia, A.I. (1958). Dielectric Polarization and Losses of Some Complex Compounds. Soviet Physics-Technical Physics, Vol. 3, pp1380−1382.

37. G.A. Smolensky (1970), Physical Phenomena in Ferroelectrics with Diffuse Phase Transition, *J. Phys. Soc. Japan*, Vol. 28 (Suppl.), pp.26-27.

38. G.A. Smolenskii, V.A. Isupov and A.I. Agranovskaya (1961), Ferroelectrics of the Oxygen-Octahedral Type with Layered Structure, *Sov. Phys. - Solid State*, Vol. 3, No. 3, pp. 651-655.

39. G.A. Smolenskii, V.A. Isupov, A.I. Agranovskaya and S.N. Popov (1961), Ferroelectrics with Diffuse Phase Transitions. *Sov. Phys. - Solid State*, Vol. 2, pp. 2584-2594.

40. G. A. Smolenskii, and A.I. Agranovskaia (1959). Dielectric Polarization of a Number of Complex Compounds. Leningrad, USSR. Semiconductor Institute, Academy of Sciences.

41. Cross, L. E. (1984). Dielectric, Piezoelectric and Ferroelectric Components. *American Ceramic Society, Ceramic Bulletin*, Vol. 63, No. 4.

42. Cross, L. E. (1987). Relaxor Ferroelectrics. PA, USA, Ferroelectrics, Vol. 76, pp. 241−267.

43. Burns, G. and Dacol, F.H., (1983), Glassy Polarization Behavior in Ferroelectric Compounds $Pb(Mg_{1/3}Nb_{2/3})O_3$ and $Pb(Zn_{1/3}Nb_{2/3})O_3$, *Solid State Commun.*, Vol. 48, No. 10, pp. 853-856.

44. J. Zhao, A.E. Glazounov and Q.M. Zhang (1998), Neutron diffraction study of electrostrictive coefficients of prototype cubic phase of relaxor ferroelectric PbMg1/3Nb2/3O3. *Appl.Phys. Lett.* 72(9), pp.1048-1050.

45. B. Dkhil, J.M. Kiat, G. Calvarin, G. Baldinozzi, S.B. Vakhrushev and S. Suard (2001), *Phys. Rev,B*, Vol. 65, 024104-1-8.

46. D.M. Fanning, I.K. Robinson, S.T. Jung, E.V. Colla, D.D. Viehland and D.A. Payne (2000), Superstructure ordering in lanthanum-doped lead magnesium niobate. *J. Appl. Phys.*, Vol. 87, No. 2, pp. 840-848.

47. N. de Mathan, E. Husson, G. Calvarin, J.R. Gavarri, A.W. Hewat, A. Morell, (1991), A structural model for the relaxor PMN at 5K. *J. Phys. Condens. Matter*, Vol. 3, p. 8159.

48. J.-C. Ho, K.-S. Liu, I.-N. Lin (1993), Study of Ferroelectricity in the PMN-PT system near the morphotropic phase boundary. *Journal of Material Sciences*, Vol. 28, pp 4497−4502.

49. J. Chen, H.M. Chan, M.P. Harmer (1989), Ordering Structure and Dielectric Properties of La/Na – Doped PMN. *J. Am. Ceram.* Soc., Vol. 72 pp. 693-698.

50. C.A. Randall, A.D. Hilton, D.J. Barber, T.R. Shrout (1990), On Short Range Ordering in the Perovskite Lead Magnesium Niobate. *J. Mater. Sci.*, Vol. 25, pp. 3461-3466.

51. D. Viehland, N. Kim, Z. Xu and D.A. Payne (1995), Structural studies of ordering in the (Pb1-xBax)(Mg1/3Nb2/3)O3. *J. Am. Ceram. Soc.*, Vol. 78, p. 2481.

52. Y. Yan, S.J. Pennycook, Z. Xu and D. Viehland (1998), Determination of the ordered structures of Pb(Mg1/3Nb2/3)O3 and Ba(Mg1/3Nb2/3)O3 by atomic-resolution Z- contrast imaging, *Appl. Phys. Letts*. 72, No. 24, pp.3145-3147.

53. D. Viehland, J. F. Li, S. J. Jang, M. Wuttig and L. E. Cross (1990), Freezing of the polarization fluctuations in lead magnesium niobate relaxors. *J. Appl. Phys.*, Vol. 68, p. 2916.

54. D. Viehland, J.F. Li, S.J. Lang, L.E. Cross, W. Wuttig, Dipolar-glass model for lead magnesium niobate. *Phys. Rev.,* B43 (1991) pp. 8316-8320.

55. V. Westphal, W. Kleweman, M.D. Glinchuk, Diffuse phase transitions and random-field-induced domain states of the ``relaxor" ferroelectric $PbMg_{1/3}Nb_{2/3}O_3$. *Phys. Rev. Lett.,* 68 (1992) 847.

56. N. K. Yushin, S.N. Dorogovtsev, *Ferroelectrics*, 143 (1993) 49.

57. A.J. Bell (1993), Calculations of dielectric properties from the super-paraelectric model of relaxors. *J. Phys: Condens. Matter*, Vol. 5, pp. 8773-8792.

58. A.E. Glazounov, A.J. Bell, A.K. Tagantsev (1995), Relaxors as superparaelectrics with distributions of the local transition temperature. *J. Phys. Condens. Matter*, Vol. 7, pp. 4145-4168.

59. L.E. Cross (2000), Domain and Phase Change Contributions to Response in High Strain Piezoelectric Actuators. *Proc. of the First-Principles Calculations for Ferroelectrics 2000, Aspen Center for Physics Winter Workshop*, Aspen, CO USA (February 13-20, 2000), editor: R.E. Cohen.

60. V. Sundar and R.E. Newnham (1992), Electrostriction and Polarization. *Ferroelectrics*, Vol. 35, pp. 431-436.

61. Q.M. Zang, J. Zhao, T. Shrout, N. Kim and L.E. Cross, Characteristics of the electromechanical response and polarization of the electric field biased ceramics. *J. Appl. Phys.*, Vol. 77 (6), March 15, 1995.

62. Military Standards 1376B (SH), February 24, 1995.

63. E. Sawaguchi (1953), Ferroelectricity versus Antiferroelectricity in the Solid Solutions of $PbZrO_3$ and $PbTiO_3$. *J. Phys. Soc. Japan*, Vol. 8, p. 615.

64. D. F. Waechter D. Liufu, M. Camirand, R. Blacow and S.E. Prasad. Development of High-strain Low-hysteresis Actuators using Electrostrictive Lead Magnesium Niobate (PMN), Canada. Proc. 3rd CanSmart Workshop on Smart Materials and Structures, (St-Hubert, Que., Sept. 28-29, 2000) pp. 31, (2000).

65. D.J. Taylor, D. Damjanovic, A.S. Bhalla and L.E. Cross (1991), Large hydrostatic piezoelectric coefficient in lead magnesium niobate: lead titanate ceramics. *Journal of Material Science Letters*, Vol. 10, pp. 668-670.

66. J. Zhao, Volkmar Mueller and Q. M. Zhang (1999), The influence of external stress on the electrocmechanical response of electrostrictive $0.9Pb(Mg_{1/3}Nb_{2/3})O_3$-$0.1PbTiO_3$ in the dc electric field biased state. *J. Mater. Res.*, Vol. 14, No. 3, pp.1-9.

67. Choi, S.W. et al (1989). Dielectric and Pyroelectric Properties in the $Pb(Mg_{1/3}Nb_{2/3})O_3$-$PbTiO_3$ System. Ferroelectrics, Vol. 100, pp. 29-38.

68. O. Noblanc, P. Gaucher, G. Calvarin, (1996). Structural and dielectric studies of Pb(Mg1/3Nb2/3)O3–PbTiO3 ferroelectric solid solutions around the morphotropic boundary. *J. Appl. Phys.,* Vol. 79 (8), pp 4291−4297.

69. J.-C. Ho, K.-S. Liu, I.-N. Lin (1995), *J. Mater. Sci.*, Vol. 30, p. 3936.

70. Q.M. Zang, J. Zhao and L.E. Cross, Ageing of the dielectric and piezoelectric properties of relaxor ferroelectric lead magnesium niobate-lead titanate in the electric field bias state. *J. Appl. Phys.*, Vol. 79 (6), March 15, 1996.

71. G. Yang, S.-F. Liu, W. Ren, and B.K. Mukherjee, Uniaxial Stress Dependence of the Piezoelectric Properties of Lead Zirconate Titanate Ceramics. Proceedings of the Twelfth IEEE International Symposium on the Applications of Ferroelectrics, ISAF'2000, Honolulu, HI, USA, July 30 August 2, 2000.

72. A. Ahmad, G. McDonald, S. E. Prasad, D.F. Waechter and R. G. Blacow (2005), Development of Piezoelectric Ceramic Composites. *Proc. 8th* CanSmart *Meeting International Workshop on Smart Materials and Structures*, Ed. G. Akhras, pp. 193-198, Toronto.

73. D. F. Waechter, D. Liufu, M. Camirand, R. Blacow and S.E. Prasad (2000). Development of High-strain Low-hysteresis Actuators using Electrostrictive Lead Magnesium Niobate (PMN). *Proc. 3rd CanSmart Workshop*, St-Hubert, Que., Canada.

74. Feigelson, (2002), [http://www-mse.stanford.edu/people/faculty/feigelson/projects/PMNT/PMNhome].

75. D. Zekria, V.A. Shuvaeva and A.M. Glazer (2005), Bi-refringence imaging measurements of the phase diagram of Pb(Mg1/3Nb2/3)O3-PbTiO3, J. *Phys. Condens. Matter*, Vol.17, pp. 1593-1600.

76. G. Calvarin, E. Husson and Z.G. Ye (1995), X-ray study of the electric field-induced phase transition in single crystal $Pb(Mg_{1/3}Nb_{2/3})O_3$. *Ferroelectrics*, Vol. 165, pp. 349-358.

77. Z.G. Ye, and H. Schmid (1993), Optical, Dielectric and Polarization Studies of the Electric Field-Induced Phase Transition in $Pb(Mg_{1/3}Nb_{2/3})O_3$ [PMN]. *Ferroelectrics*, Vol. 145, pp. 83-106.

78. E.V. Colla, N.K. Yushin and D. Viehland (1998), Dielectric properties of $(PMN)_{1-x}(PT)_x$. *J. Appl.Phys.*, Vol. 83, No. 6, pp. 3298-3304.

79. Y. Lu, D. -Y. Jeong, Z. -Y. Cheng, Q.M.Zang, H.-S. Luo, Z.W. Yin and D. Viehland (2001), Phase Transitional Behavior and Piezoelectric Properties of the orthorhombic Phase of PMN-PT Single Crystals. *Appl. Phys. Lett.*, Vol. 78, p. 3109.

80. Z.-G. Ye, B. Noheda, M. Dong, D.E. Cox and G. Shirane (2001), Monoclinic phase in the relaxor-based piezoelectric/ferroelectric $Pb(Mg_{1/3}Nb_{2/3})O_3$-$PbTiO_3$ system. *Phys. Rev.B*, Vol. 64, 184114.

81. J.M. Kiat, Y Usesu, B. Dkhil, M. Matsuda, C. Malibert and G. Calvarin (2002), Monoclinic structure of unpoled morphotropic high piezoelectric PMN-PT and PZN-PT compounds. *Phys. Rev.B*, Vol. 65, 064106.

82. A.K. Singh and D. Pandey (2001), Structure and the location of the morphotropic phase boundary region in $(1-x)[Pb(Mg_{1/3}Nb_{2/3})O_3]$-$xPbTiO_3$ *J. Phys.:Condens. Mater,* Vol. 13, L931.

83. B. Noheda, D.E. Cox, G. Shirane J. Gao and Z.G. Ye (2002), Phase diagram of the ferroelectric relaxor (1-x)PbMg1/3Nb2/3O3-xPbTiO3, *Phys. Rev. B,* Vol. 66, 054104-1-8.

84. F. Bai, N. Wang, J.F. Li, D. Viehland, P.M. Gehring, G. Xu and G. Shirane (2004), X-ray and neutron investigations of the structural phase transformation sequence under an electric field in 0.7Pb(Mg1/3Nb2/3)-0.3PbTiO3 crystal. *J. Appl. Phys*. Vol. 96, No.3, pp. 1620-1627.

85. H. Cao, F. Bai, N.Wang, J. Li, D. Viehland, G.Xu and G. Shirane, Intermediate ferroelectric orthorhombic and monoclinic MB phases in [110] - electric field cooled Pb(Mg1/3Nb2/3)O3-30%PbTiO3 crystals, PACS number(s) 61.10Nz, 77.84.Dy,77.80Bh.

86. P.M. Gehring W. Chen, Z.-G. Ye and G. Shirane, A universal phase diagram for PMN-xPT and PZN-xPT. ArXiv:cond-mat/0304289 v1 11 April 2003.

87. G. Xu, Z. Zhong, Y. Bing, Z.-G. Ye, C. Stock and G. Shirane (2003), Ground state of the relaxor ferroelectric $Pb(Zn_{1/3}Nb_{2/3})O_3$. *Phys. Rev. B.*, Vol. 67, 104102.

88. M. W. Barsoum (1997), Fundamentals of Ceramics. McGraw-Hill, ISBN 0-07-005521-1.

89. J.M. Gere and S.P. Timoshenko (1997), Mechanics of Materials 4th edition. PWS Publishing Company, Boston, ISBN 0-534-93429-3.

90. A. A. Griffith (1920), The Phenomena of Rupture and Flow in Solids. *Philos. Trans. R. Soc. London, Ser. A, Vol.* 221, pp. 163-198.

91. E. Orowan (1948-9), Fracture and Strength of Solids. *Rep. Progr. Phys.*, Vol. 12, p. 185. (London: The Physical Society).

92. K.D. McHenry and B.G. Koepke (1983), Electric Field Effects on Subcritical Crack Growth in PZT. *Fract. Mech. Ceram.,* (1983) Vol. 5, pp. 337-352.

93. D.J. Taylor, R.E. Newnham and W.B. Carlson (1988), The Effect of Electric Field on Mechanical Strain and Stress in Flawed Electroceramics. *Ferroelectrics*, Vol. 87, pp. 81-84.

94. R.R. Winzer, N. Shankar and A.P. Ritter (1989), Designing cofired multilayered electrostrictive actuators for reliability. *J. Amer. Ceram. Soc.*, Vol. 72, pp. 2246-2257.

95. Y.E. Pak (1990), Crack Extension Force in a Piezoelectric Material. *ASME J. Appl. Mech.*, Vol. 57, pp. 647-653.

96. A.G. Tobin and Y.E. Pak (1993), Effect of Electric Fields on Fracture Behavior of PZT Ceramics. *Proc. SPIE, Smart Struct. Mater.,* Vol. 1916, pp. 78-86.

97. Z. Suo (1991), Mechanical concepts for failure in. ferroelectric ceramics. *Smart Structures and Materials*, AD-Vol 24/AMD-Vol 123, pp. 1-6.

98. S. Park and C-T. Sun (1995), Fracture Criteria for Piezoelectric Ceramics. *J. Amer. Ceram. Soc.,* Vol. 78, No. 6, pp. 1475-1480.

99. W. Yang and Z. Suo (1994), Cracking in ceramic actuators caused by electrostriction. *J. Mech. Phys. Solids*, Vol. 42, No. 4, pp. 649- 664.

100. T. Zhu and W. Yang (1999), Fatigue crack growth in ferroelectrics driven by cyclic electric loading, *J. Mech. Phys. Solids*, Vol. 47, pp. 81-97.

101. H. Cao and A.G. Evans (1994). Electric-field-induced fatigue crack growth in piezoelectrics. *J. American Ceramic Society*, Vol. 77, pp 1783−1786.

102. C.S. Lynch, W. Yang, L. Collier, Z. Suo and R.M. McMeeking (1995). Electric-field-induced cracking in ferroelectric ceramics. *Ferroelectrics*, Vol. 166, pp 11−30.

103. H. Wang and R.N. Singh (1997), Crack Propagation in Piezoelectric Ceramics: Effect of Applied Electric Fields. *J. Appl. Phys.,* Vol. 81, No. 11, pp. 7471-7479.

104. J. Shieh, J.E. Huber and N.A. Fleck, Fatigue crack growth in ferroelectrics under electric loading, *J. Euro. Ceram. Soc.*, Vol. ?? (2005) in the press.

105. A.S. Raynes, S.G. White and S.W. Freiman, Electric Field Effects on Crack Growth in a Lead Magnesium Niobate Ceramic. *Ceramic Transactions*, 15, (1989) 129-142.

106. H.W. King, E.A. Payzant and T.A. Caughlin, Temperature Discrepancies in High Temperature Diffractometry, Adv. X-ray Analysis, 40, CD-ROM ISSN 1097-0002, International Center for Diffraction Data (ICDD), (1997/1998), p. 681-687.

107. H. W. King, M.A. Peters, E.A. Payzant and M.B. Stanley. Low Temperature Attachment for X-ray Powder Diffractometry. Advances in X-ray Analysis, Vol. 37, pp 457−463.

108. King, H. W. and E.A. Payzant (1995). Error Corrections for X-ray Powder Diffractometry. London, Ont., 7th Annual Canadian Material Science Conference.

109. H. W. King and L.F. Vassamillet (1962). Precision X-ray Diffractometry Using Powder Specimens. Advances in X-ray Analysis, Vol. 6, pp 142−157.

110. B. Yan, D. Waechter, R. Blacow and S.E. Prasad (2002). Measurement of Strain and Polarization in Piezoelectric and Electrostrictive Actuators, *Proc. 2nd. Canada-Us CanSmart Workshop on Smart Materials and Structures*, Ed. G. Akhras, (Montreal, October 10−12, 2002), pp 33−39, ISBN 0-9685840-3-9.

111. R. Gerson and T.C. Marshall (1959). Dielectric Breakdown of Porous Ceramics. *J. Appl. Phys.,* Vol. 30, pp 1650−1653.

112. D.F.Waechter, S.E. Prasad and R. Blacow, Biased PZT materials for acoustic transducers, sensors and systems, Proc. ICONS 2002, International Conference on Sonar-Sensor Systems, (Cochin, India, December 11−13, 2002), pp. 665−672.

113. Q.M. Zhang, J. Zhao (1997), Polarization responses in lead magnesium niobate based relaxor ferroelectrics. *Applied Physics Letters*, Vol. 71, Issue 12, pp. 1649-1651.

114. L.E. Cross, Dielectric, Piezoelectric and Ferroelectric Compounds, *Ceramic Bull.*, 63, pp. 586-590 (1994).

115. Powder Diffraction File PDF 2, Release 2002, *International Center for Diffraction Data (ICDD)*, Newton Square, PA 19073-3273, USA. (2001).

116. S. Kojima and F. Jiang (2002). Broadband Brillouin Scattering of Relaxor Ferroelectric Crystals. [www http://particle.physics.wm.edu/ferro2001_papers/06_Kojima.pdf].

117. Xu Guisheing, Luo Haosu, Wang Pingchu, Qi Zhenyi and Yin Zhiwen (2000), Ferroelectric phase transition in relaxor ferroelectric single crystals 0.76PMN-0.24PT. *Chinese Science Bulletin,* Vol. 45, No. 15, pp. 1380-1385.

118. Z.-G. Ye, Y. Bing, J. Gao, A.A. Bokov, P. Stephens, B. Noheda and G. Shirane (2003), Development of ferroelectric order in relaxor (1-x)$Pb(Mg_{1/3}Nb_{2/3})O_3$ ($0 \leq x \leq 0.15$). *Phys. Review B*, Vol. 67, 104104.

119. J-C. Shaw, K-S. Liu and I-N. Lin, Dielectric Behavior at Morphotropic Phase boundary for PMN-PZT Ceramics, Scripta Metall. et Material., 29, 981-986 (1993).

120. M. Hansen and K. Anderko, Constitution of Binary Alloys, McGraw-Hill Book Co., New York, 1958, pp. 677-684.

121. B. Noheda and D.E. Cross (2005), Bridging Phase Boundaries of Lead-Oxide Solid Solutions, arXiv:cond-mat/0511256 v1-12.

122. A.M. Glazer, P.A. Thomas, K.Z. Baba-Kishi, G.K.H. Pang and C.W. Tai (2004), Influence of short-range and long-range order on the evolution of the morphotropic phase boundary in Pb $(Zr_{1-x} Ti_x)O_3$. Phys. Review B, Vol. 70, 184123.

8.0 Appendix

8.1. Equipment enhancements

8.1.1. Roll-a-Round Stand for the Refrigeration Cooling Unit

A new water-cooled Haskris refrigeration unit was purchased to replace the antiquated air-cooled model that had been previously used to cool the x-ray diffractometer. The new cooling unit is mounted on a portable stand that includes a shelving arrangement, along with the plumbing and a water filter designed to form a closed-loop system for cooling

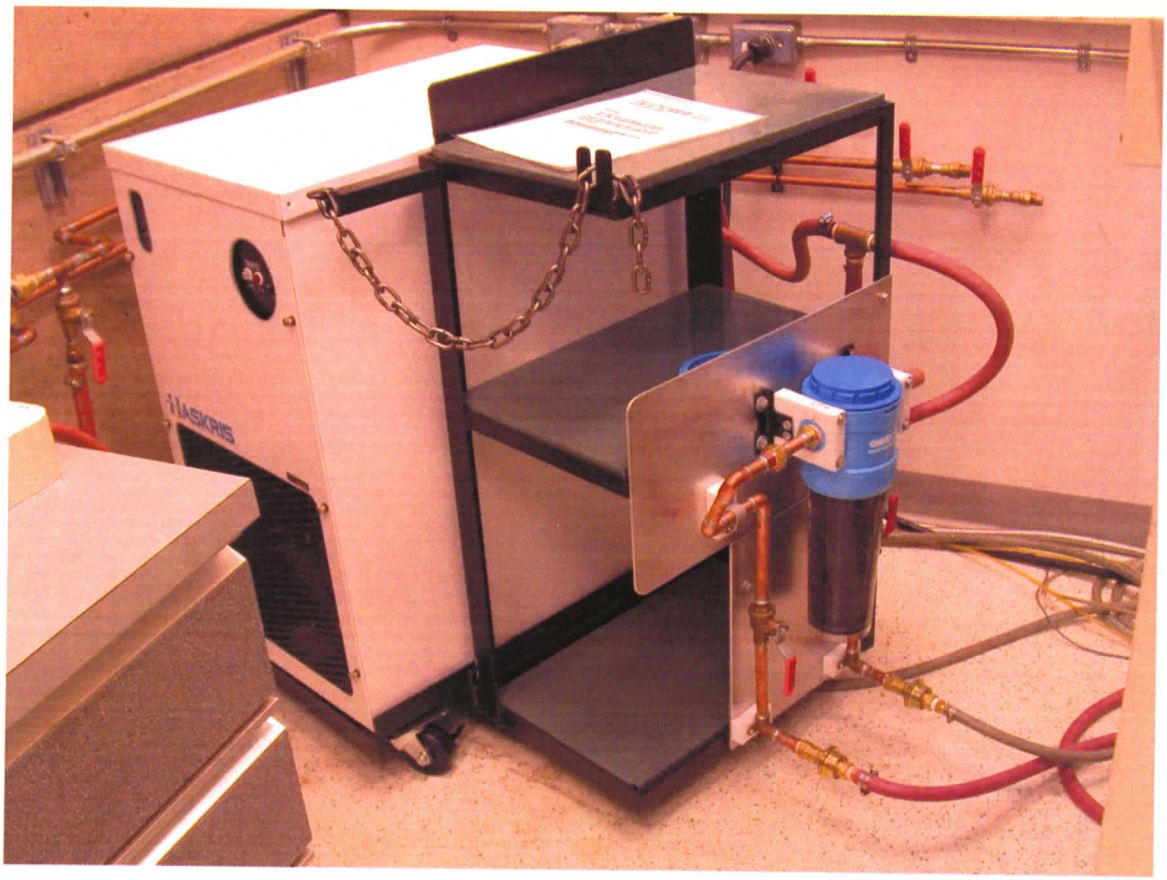

Figure 8-1 Haskris cooling unit on rolling stand with plumbing and filter

the diffractometer. The stand has four 2 inch casters (two swivel and two are unidirectional) that allow the cooling unit to be moved for cleaning and working behind the unit. These casters can hold up to 175 lbs each, which is deemed adequate to withstand the 425 lb weight of the cooling unit.

The shelves are designed to hold a vacuum roughing pump on the bottom shelf and various closed-loop water heating/circulating systems on the upper two shelves. As well, the shelves provide support for the plumbing and filter system that are connected to the sides of the shelves (see Figure 8-2). The water from the cooling unit is fed through the

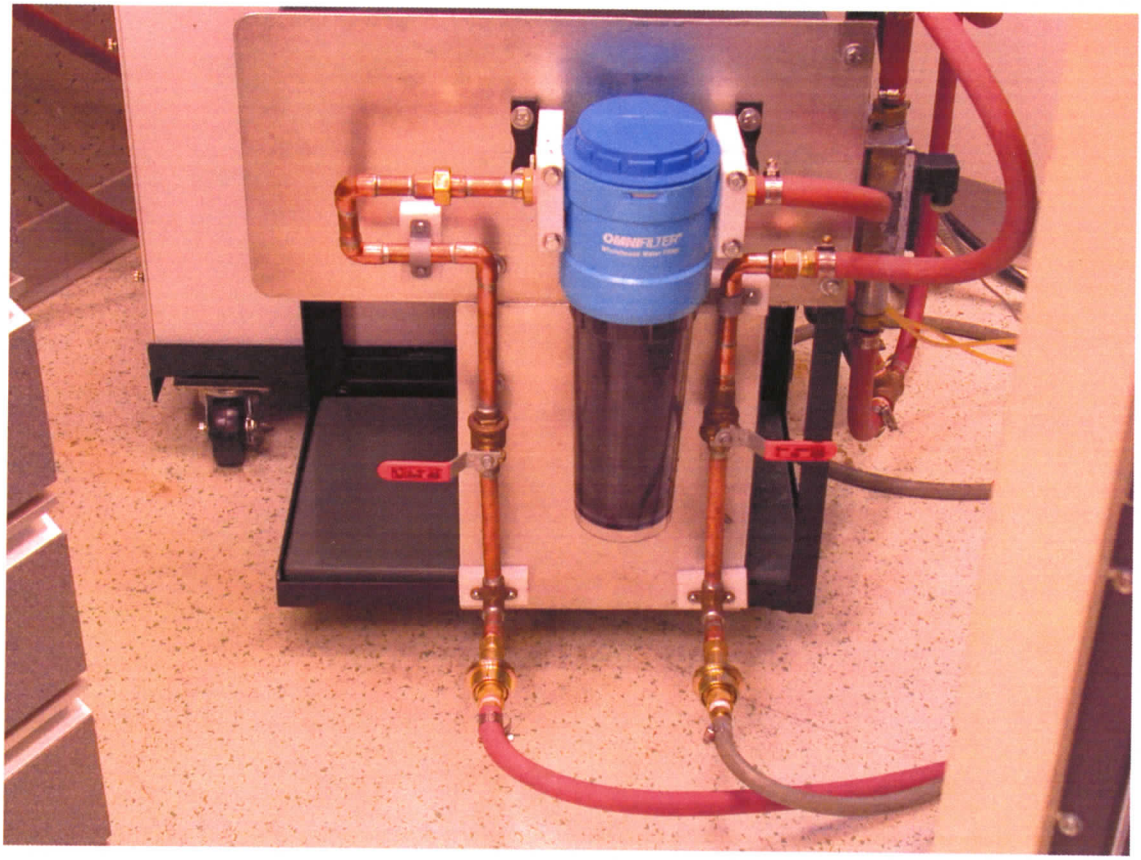

Figure 8-2 Water filter and plumbing arrangement attached to Haskris cooling unit.

filter to extract heat from the x-ray tube and generator; then, returned to the cooling unit via a closed loop. The filter unit has a flow capacity of up to 5 GPM, which is sufficient to handle the cooling requirements of the diffractometer.

8.1.2. Digital camera mounted on microscope

A Zeiss universal microscope with a metallurgical indirect lighting system and appropriate objectives and eyepieces to give a magnification to 1000X in ordinary and polarized light was originally fitted with a lens-less 35-mm camera that used the optics of the microscope for focussing. To enable the microscope to be used with a Nikon 995 digital camera with a 4X zoom lens, the phototube of the microscope had to be shortened a precise amount so that the image from the microscope could be focused clearly on the detector of the camera. The microscope/camera combination enables clear sharp images to be recorded digitally and transferred by cable to a PC computer. The modified instrument is used at present to examine the surface discolouration observed on PMN-PT specimens after heating at temperatures up to 300 °C in vacuum up to 10^{-5} Torr.

8.2. PZT Standards and Designations

8.2.1. Military Standard 1376B (SH)

The following table gives the official definitions for the Navy Types I through VI.

Table 8-1 Table of Navy Type definitions [62]

Navy Type	Description
Type I	A modified lead-zirconate-titanate composition generally recommended for medium- to high-power acoustic applications. Its ''resistance'' to depoling at high electric drive and/or mechanical stress makes it suitable for deep-submersion acoustic applications.
Type II	A lead zirconate-titanate composition modified to yield higher charge sensitivity, but one that is not suitable for high electric drive due to dielectric heating. This material is more suitable for passive devices such as hydrophones. Advantages also include better time stability.
Type III	Similar to type I but greatly improved for use at high electric drive because of lower losses. Its field dependency of dielectric and mechanical losses is substantially reduced. However, at low to moderate electric-drive levels, type I material may actually be a better choice because of greater electromechanical activity.
Type IV	A modified barium-titanate composition for use in moderate electric-drive application. It is characterized by lower piezoelectric activity and lower Curie temperature than any of the lead zirconate-titanate compositions.
Type V	A composition intermediate to types II and VI and thus to be used accordingly.
Type VI	Similar to type II with higher charge sensitivity and dielectric constant, at the expense of a reduced Curie temperature.

Table 8-2 General properties of Navy Types I to III, [62]

MATERIAL TYPES		I		II		III	
PROPERTY	SYMB	TYPICAL VALUES	AGING RATE[1/]	TYPICAL VALUES	AGING RATE[1/]	TYPICAL VALUES	AGING RATE[1/]
Free Rel. Diel. Const.	K_{33}^T	1275 ± 12.5%	-4.5 ± 2.0	1725 ± 12.5%	-1.5 ± 0.7	1025 ± 12.5%	-4.0 ± 1.5
Diel. Loss Factor	$\tan\delta$	≤ 0.006		≤ 0.020		≤ 0.004	
Planar Coup. Factor[2/]	k_p	0.58 ± 8.0%	-2.0 ± 1.0	0.60 ± 8.0%	-0.25 ± 0.15	0.50 ± 8.0%	-2.0 ± 1.0
Piezoelectric Coefficient[3/] 10^{-12} m/V	d_{33}	290 ± 15%		390 ± 15%		215 ± 15%	
Planar Freq. Constant Hz-m[4/]	N_p	2200 ± 8.0%	1.3 ± 0.8	1950 ± 8.0%	0.20 ± 0.10	2300 ± 8.0%	1.3 ± 0.8
Density 10^3 kg/m^3	ρ	≥ 7.45		≥ 7.60		≥ 7.45	
Mech. Qual. Factor[2,5/]	Q_m	≥ 500		≥ 75		≥ 800	
Percentage Change in K_{33}^T % 0° to 50°C[6/]		9.5 ± 3.0		25 ± 10		9.0 ± 3.0	
Approx. Curie Temp. °C		325		350		325	

See footnotes at end of table.

Table 8-3 General properties of Navy Types V to VI, [62]

MATERIAL TYPES		IV		V		VI	
PROPERTY	SYMB	TYPICAL VALUES	AGING RATE 1/	TYPICAL VALUES	AGING RATE 1/	TYPICAL VALUES	AGING RATE 1/
Free Rel. Diel. Const.	K^T_{33}	1275 ± 12.5%	-1.50 ± 2.0	2500 ± 12.5%	-2.0 ± 1.0	3250 ± 12.5%	-2.0 ± 1.0
Diel. Loss Factor	tan δ	≤ 0.010		≤ 0.025		≤ 0.025	
Planar Coup. Factor 2/	k_p	0.30 ± 8.0%	-1.50 ± 0.50	0.63 ± 8.0%	-0.25 ± 0.2	0.64 ± 8.0%	-0.25 ± 0.2
Piezoelectric Coefficient 3/ 10^{-12} m/V	d_{33}	140 ± 15%		495 ± 15%		575 ± 15%	
Planar Freq. Constant Hz-m 4/	N_p	3150 ± 8.0%	0.40 ± 0.20	1950 ± 8.0%	0.35 ± 0.2	1940 ± 8.0%	0.35 ± 0.2
Density 10^3 kg/m^3	ρ	≥ 5.50		≥ 7.40		≥ 7.40	
Mech. Qual. Factor 5/6/	Q_m	≥ 400		≥ 70		≥ 65	
Percentage Change in K^T_{33} % 0° to 50°C 6/		5.0 ± 2.0		30 ± 10		40 ± 10	
Approx. Curie Temp. °C		115		240		180	

1/ The aging rate is the typical change in properties up to 100 days after poling using the 10-day value as the base expressed in percent per time decade.

2/ The planar coupling factor, k_p, will be determined from figure 5, where f_n is the frequency of minimum admittance and f_m is the frequency of maximum admittance; f_m to be measured at fields <100 V/m.

3/ d_{33} is a new value added to the table. The values shown are calculated values based on appendix C. A method of measurement of d_{33} has not been standardized as of the revision of this document.

4/ Planar mode disc $N_p = (f_m D)$.

5/ The mechanical quality factor, Q_m, defined by $Q_m = Y_m/(2\pi f_m C^T k_{31}^2)$ where C^T is the small signal capacitance measured at 1 kHz, Y_m is the maximum admittance measured at f_m.

6/ Values for the mechanical quality factor and the change in K^T_{33} with temperature are not 10-day values, but shall be measured at approximately 100 days.

8.2.2. Sensor Technology Designations

The following table cross references the Sensor Technology Limited designations to the Navy Type designations.

Table 8-4 Sensor Technology Designations to Navy Types [6]

Sensor Technology PZT Designation	Navy Type Designation
BM 200	---------
BM 300	---------
BM 400	Type I
BM 500	Type II
BM 527	Type V
BM 532	Type VI
BM 800	Type III
BM 900	----------

8.3. Force vs. Displacement graphs

Force vs. Displacement graphs were plotted for the BM200 and BM800 specimens which were indented at the University of British Columbia Ceramics laboratory. One example for each material is shown below. These graphs are not available for the PMN-PT and BM532 specimens, which were indented in Ontario.

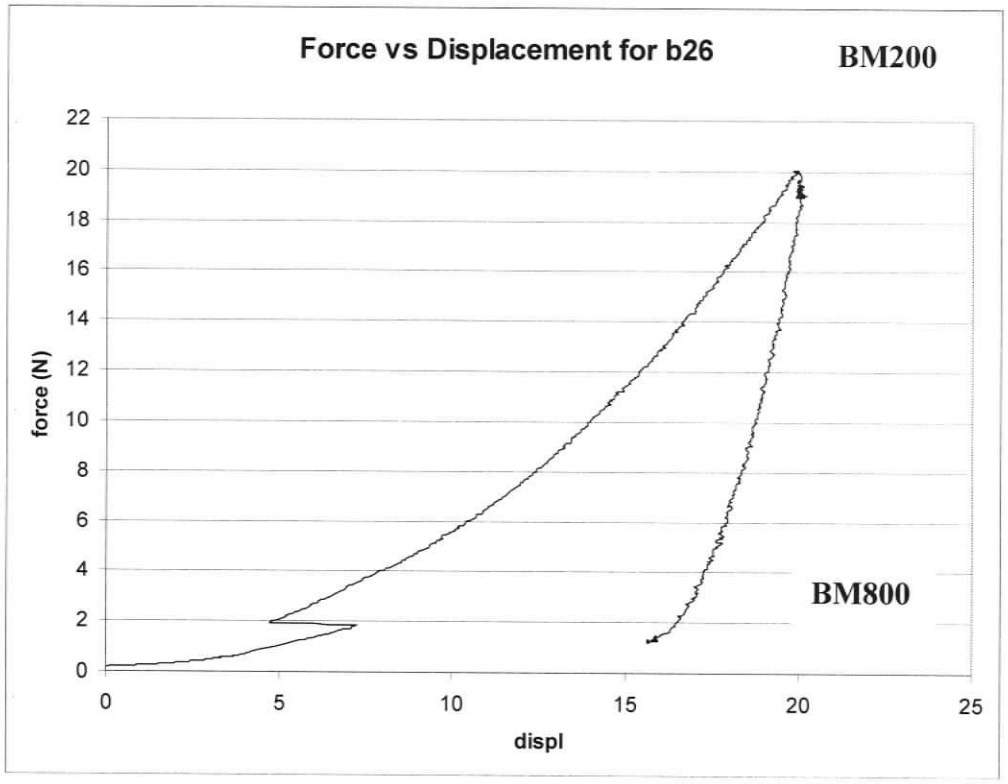
Force vs Displacement for b26
BM200
BM800
force (N)
displ
0
2
4
6
8
10
12
14
16
18
20
22
0
5
10
15
20
25

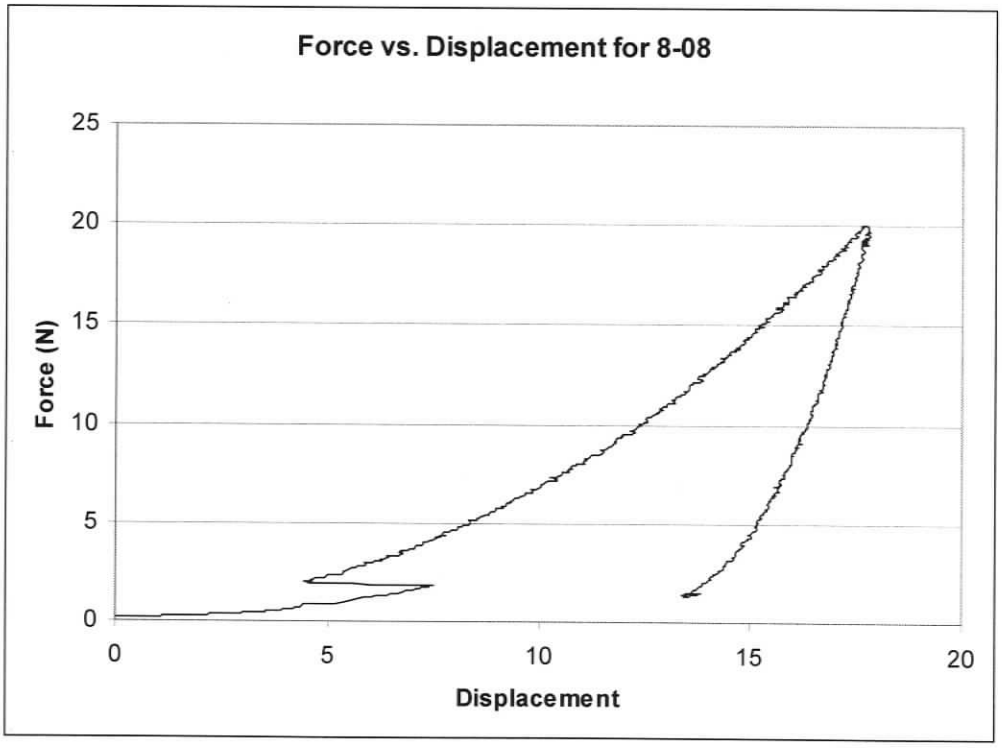
Force vs. Displacement for 8-08
Force (N)
Displacement
0
5
10
15
20
25
0
5
10
15
20

8.4. Example Indentation and Cyclic Electric Field Data (BM800)

specimen	indent	set voltage	frequency (in Hz)	total cycles	initial crack length (in mm) left	final crack length (in mm) left	initial crack length (in mm) right	final crack length (in mm) right	comments
8_32	Vickers	500	5	1	0	0			
	Vickers	500	5	3	0	0			faint line to right. Picture #11. Line is glass chips that sometimes turn into cracks.
	Vickers	500	5	5	0	0			
	Vickers	500	5	10	0	0			
	Vickers	500	5	20	0	0			
	Vickers	500	5	50	0	0			
	Vickers	500	5	100	0	0			
	Vickers	500	5	500	0	0			
	Vickers	500	5	1000	0	0			
	Vickers	500	5	2000	0	0			
	Vickers	1000	5	1	0	0			
	Vickers	1000	5	3	0	0			
	Vickers	1000	5	5	0	0			
	Vickers	1000	5	10	0	0			
	Vickers	1000	5	50	0	0			
	Vickers	1000	5	500	0	0			
	Vickers	1000	5	1500	0	0			
	Vickers	2000	5	50	0	0			
	Vickers	2000	5	100	0	0			
	Vickers	2000	5	500	0	0			
	Vickers	2000	5	1500	0	0			
	Vickers	4000	5	1000	0	0			
	Vickers	4000	5	5000	0	0			

8_43	Vickers	500	5	1	0.287	0.287			Crack on left side only
	Vickers	500	5	3	0.287	0.287			Pictures #12 & #13
	Vickers	500	5	5	0.287	0.287			
	Vickers	500	5	10	0.287	0.287			
	Vickers	500	5	20	0.287	0.287			
	Vickers	500	5	50	0.287	0.287			
	Vickers	500	5	100	0.287	0.287			
	Vickers	500	5	500	0.287	0.287			
	Vickers	500	5	1000	0.287	0.287			
	Vickers	1000	5	1	0.287	0.287			
	Vickers	1000	5	3	0.287	0.287			
	Vickers	1000	5	5	0.287	0.287			
	Vickers	1000	5	10	0.287	0.287			
	Vickers	1000	5	50	0.287	0.287			
	Vickers	1000	5	100	0.287	0.287			
	Vickers	1000	5	500	0.287	0.287			
	Vickers	1000	5	1000	0.287	0.287			
	Vickers	2000	5	1	0.287	0.287			
	Vickers	2000	5	3	0.287	0.287			
	Vickers	2000	5	5	0.287	0.287			
	Vickers	2000	5	10	0.287	0.287			
	Vickers	2000	5	50	0.287	0.287			
	Vickers	2000	5	100	0.287	0.287			
	Vickers	2000	5	500	0.287	0.287			
	Vickers	2000	5	1000	0.287	0.287			
	Vickers	4000	5	50	0.287	0.287			
	Vickers	4000	5	500	0.287	0.287			
	Vickers	4000	5	2500	0.287	0.287			
	Vickers	4000	5	5000	0.287	0.287			

8_34	Vickers	1500	5	1	0.156	0.156	0.337	0.337	Picture #16
	Vickers	1500	5	3	0.156	0.156	0.337	0.337	
	Vickers	1500	5	5	0.156	0.156	0.337	0.337	
	Vickers	1500	5	10	0.156	0.156	0.337	0.337	
	Vickers	1500	5	50	0.156	0.156	0.337	0.337	
	Vickers	1500	5	500	0.156	0.156	0.337	0.337	
	Vickers	1500	5	2500	0.156	0.156	0.337	0.337	
	Vickers	1500	5	5000	0.156	0.156	0.337	0.337	
	Vickers	4000	5	10	0.156	0.156	0.337	0.337	
	Vickers	4000	5	50	0.156	0.156	0.337	0.337	
	Vickers	4000	5	100	0.156	0.156	0.337	0.337	
	Vickers	4000	5	500	0.156	0.156	0.337	0.337	
	Vickers	4000	5	2500	0.156	0.156	0.337	0.337	
	Vickers	4000	5	5000	0.156	0.156	0.337	0.337	Picture #17
8_42	Vickers	1500	5	1	0	0	0	0	
	Vickers	1500	5	3	0	0	0	0	
	Vickers	1500	5	5	0	0	0	0	
	Vickers	1500	5	10	0	0	0	0	
	Vickers	1500	5	50	0	0	0	0	
	Vickers	1500	5	500	0	0	0	0	
	Vickers	1500	5	1000	0	0	0	0	
	Vickers	4000	5	2000	0	0	0	0	Possibly a hairline crack on right and left, (difficult to tell).
	Vickers	4000	5	5000	0	0	0	0	Apparent cracks on left and right.